Faculty of Science, Palacký University
in Olomouc

Joint Laboratory of Optics

Nonlinear optics in modern photonic structures - generation of quantum correlated photon pairs

Ph.D. Thesis

Dalibor Javůrek

Supervisor:
Doc. RNDr. Jan Peřina Jr., Ph.D.

Olomouc 2015

Přírodovědecká fakulta, Univerzita Palackého
v Olomouci

Společná laboratoř optiky

Nelineární optika v moderních fotonických strukturách - generace kvantově korelovaných fotonových párů

Dizertační práce

Dalibor Javůrek

Školitel:
Doc. RNDr. Jan Peřina Jr., Ph.D.

Olomouc 2015

Bibliographic details

Title	Non-linear optics in modern photonic structures - generation of quantum correlated photon pairs
Nadpis	Nelineární optika v moderních fotonických strukturách - generace kvantově korelovaných fotonových párů
Type	PhD. degree thesis
Author	Dalibor Javůrek
Supervisor	Jan Peřina Jr.
University	Palacký University in Olomouc
Study program	Physics
	Optics and Optoelectronics
Department	Joint Laboratory of Optics
Language	English
Year	2015
Pages	114

Statement of originality

I hereby declare that this thesis is my own work and that, to the best of my knowledge and belief, it contains no material previously published or written by another person nor material which to a substantial extent has been accepted for the award of any other degree or diploma of the university or other institute of higher learning, except where due acknowledgement has been made in the text.

In Olomouc, ..., 2015 .....

Submitted on ....., 2015

The author grants permission to Palacký University in Olomouc to store and display this thesis and its electronic version in the university library and on the official website.

Acknowledgement

I am very grateful to my parents, who have always been supporting my in my studies by all means. They enabled the thesis to be written, and more importantly, gave me an opportunity to enrich my knowledge about the world's nature. I am thankful to my supervisor Jan Peřina Jr. for his helpfulness and patience during the preparation of the scientific papers as well as for the discussions about the logical problems. I want to thank my colleague Jiří Svozilík for cooperation, useful discussions, and his indispensable contribution to the released scientific papers.

Abstract

Spontaneous parametric down-conversion is a nonlinear quantum process in which correlated photons are created in pairs. Photon pairs have become an indispensable tool for verification of quantum-mechanical principles, in quantum-information processing, for quantum-communication protocols and quantum cryptography.

Modern photonic structures enhance photon-pair emission rates and simultaneously modify the properties of generated photon pairs. Periodically-poled silica ring-shaped fibers are capable of generation and stable guidance of photon pairs in modes with defined orbital angular momentum (OAM). The most stable modes have been selected for the nonlinear interaction. Their transversal profiles together with phase-matching conditions have been analyzed to obtain the desired interaction. Narrow-band and broad-band emission of photon pairs have been obtained in dependence on the mode of the pump beam. In the time domain, the conditional probability of detection of a signal photon has been obtained and correlation times have been evaluated. The emission of photon pairs entangled in OAMs and frequencies have been analyzed. Effective dimension of the entangled space has been quantified by means of the Schmidt number indicating a maximally entangled photon-pair state. The influence of noise on the entangled OAM state has been evaluated by the Clauser-Horne-Shimony-Holt inequality.

Also metallo-dielectric layered structures have been analyzed as highly efficient sources of photon pairs. Layered structures consisting of silver (Ag) and Gallium-Nitride (GaN) have been investigated. Two structures formed by three and eleven layers have been designed to maximize the emission rate. They have been examined with respect to relative signal photon-number density in the angular-spectral domain. Both structures have been found more efficient than dielectric structures due to strong back-scattering effects caused by the high index-of-refraction contrast. Distributions of electric-field amplitudes corresponding to the emission maxima have been analyzed. Correlated areas as well as temporal characteristics including those appropriate for the Hong-Ou-Mandel interferometer have been investigated. Also, numbers of noise photons have been discussed as the metallic layers are absorptive.

Abstrakt

Spontánní parametrická frekvenční konverze je nelineární kvantový proces, při kterém jsou vytvářeny korelované fotonové páry. Fotonové páry se staly jedinečným prostředkem pro ověření fundamentálních principů kvantové mechaniky, pro zpracování kvantové informace, pro kvantově komunikační protokoly a kvantovou kryptografii.

Moderní fotonické struktury zvyšují míru emise fotonových párů a současně modifikují vlastnosti generovaných fotonových párů. Periodicky pólovaná křemičitá prstencová vlákna jsou schopna generace a stabilního vedení fotonových párů s definovaným úhlovým momentem (OAM). Nejstabilnější módy byly vybrány pro nelineární interakci. Jejich příčné profily společně s podmínkou sfázování byly analyzovány za účelem optimalizace procesu. Pro odlišné módy čerpacího svazku byla obdržena úzko- a širokospektrální emise fotonových párů. V časové doméně byla obdržena podmíněná pravděpodobnost detekce jalového fotonu a byly spočteny korelační časy. Analyzována byla emise fotonových párů entanglovaných v OAM a frekvenci. Efektivní dimenze entanglovaného prostoru byla vyčíslena pomocí Schmidtova čísla. To poukázalo, že fotony v páru jsou maximálně entanglované v OAM. Vliv šumu na entanglovaný OAM stav byl vyhodnocen pomocí Clauser-Horne-Shimony-Holtovy nerovnosti.

Metalo-dielektrické fotonické struktury byly rovněž analyzovány jako účinné zdroje fotonových párů. Zkoumány byly vrstevnaté struktury skládající se ze stříbra (Ag) a Gallium-Nitridu (GaN). Dvě struktury skládající se ze tří a jedenácti vrstev byly navrženy tak, aby maximalizovaly míru emise fotonových párů. Byly zkoumány s ohledem na relativní počet emitovaných signálových fotonů v úhlově-spektrální doméně. Obě struktury byly shledány účinnějšími než jejich dielektrické protějšky díky vysokému kontrastu indexů lomu obou materiálů. Analyzovány byly distribuce amplitud elektrických polí, které přísluší nejsilnější emisi fotonových párů. Předmětem zkoumání také byly korelované plochy a časové charakteristiky včetně charakteristik příslušných Hong-Ou-Mandelově interferometru. Diskutován byl i počet šumových fotonů, jelikož metalické vrstvy vykazují nenulovou absorpci.

Contents

Chapter 1

Intoduction

1.1 The goals of the thesis

The modern photonic structures are bright sources of photon pairs. The main goal was to study spontaneous parametric down conversion in a metallo-dielectric layered medium and a periodically-poled ring silica fiber. In both cases the spectral, spatial and temporal properties of photon pairs had to be studied. The photon pair emission rate of both sources had to be evaluated in order to determine their efficiency.

1.2 Annotation

Chapter 1 identifies goals of the thesis (Sec. 1.1) and gives an overview about the content of the thesis (Sec. 1.2).

The introduction to the field of classical non-linear optics is provided in Chapter 2. A polarization vector describing linear and non-linear interaction of radiation with matter is defined together with frequency dependent linear and non-linear susceptibilities (Sec. 2.1). Its definition is utilized for derivation of the coupled wave equations. A general interaction of two monochromatic waves in the second-order non-linear medium is qualitatively described in Section 2.2. The individual processes, which arise from the interaction, are explained by the electron-photon energy transition schemes.

Chapter 3 covers the topic of photon pairs. The first step, which started a fruitful era of quantum phenomena is briefly mentioned in Section 3.1.1. The quantum-optical approach to quantization of the electromagnetic field in vacuum is placed in Section 3.1.2. The properties and usefulness of the photon pairs in physics are summarized in Section 3.2. The generation of photon pairs entangled in various degrees of freedom from

a bulk crystal is explained in Section 3.3.

The spontaneous parametric down-conversion (SPDC) in a ring fiber is described in Chapter 4. Section 4.1 introduces integrated sources of photon pairs (Sec. 4.1.1), explains usefulness of modes with orbital angular momentum (OAM), concept of quasi-phase matching and the thermal poling procedure (Sec. 4.1.3). The theorectial approach to SPDC in the ring-fiber is developed in Section 4.2. The simulated quantities characterizing a photon pair are defined at the end of the Section. The angular decomposition of individual modes together with determination of the number of Schmidt modes is described in Section 4.3. The derivation of analytical formula of the guided OAM modes of the ring fiber and their analysis are in the Sections 4.4 and 4.5. Section 4.5 covers as well analysis of the narrow-band generation of photon pairs. The broad-band type is investigated in Section 4.6. The entanglement of the generated photon pairs is explored in Section 4.7. Subsequently, the impact of the noise on the entanglement of generated photon pairs is evaluated.

The emission of the photon pairs from a layered structure is examined in Chapter 5. In the introduction, the state of art is briefly summarized. The non-linear model of metal is derived from hydrodynamical model in Section 5.2. The SPDC model in the layered medium is provided in Section 5.3. The quantities characterizing a photon pair are defined in Section 5.4. Section 5.5 is devoted to a theory of photon losses in the layered medium. Emission of photon pairs from simple metal-dielectric-metal (Ag-GaN-Ag) resonator and structure with 11 layers (GaN-Ag) is explored in Section 5.6 and Section 5.7, respectively. The correlated areas, temporal properties (both in Sec. 5.8) and photon losses (Sec. 5.9) have been considered as well.

The Conclusion (Chapter 6) summarizes the content of the thesis in English (Sec. 6.1) and Czech (Sec. 6.2) language. The list of author's publications is found on page 102, while the references are placed on page 103.

Chapter 2

Non-linear phenomena of the second order

The elements of dispersion in transparent media are provided in Section 2.1. The polarization vector is introduced for both linear and non-linear media. The non-linear media are assumed to posses only second-order non-linearity. With the definition of polarization vector in dependence on the electric field, the equations for spatial evolution of the electric-field frequency amplitudes are derived. Polarization vector for a general non-linear second-order process is derived in Section 2.2. All the associated processes - second harmonic generation, sum-frequency generation and difference-frequency generation are described with electron transition schemes.

2.1 Non-linear vector of polarization

Non-linear optics started to develop at the beginning of 1960's. Shortly after the discovery of light amplification by stimulated emission of radiation (laser). The lasers were the first sufficiently intense sources of coherent light. The intensity of generated light was strong enough to reveal the non-linear nature of matter for the first time. The first observed non-linear effect was second-harmonic generation by Franken et al. [1]. Since then, the field on non-linear optics started its fruitful era. Many distinct non-linear phenomena have been observed and theoretically described [2]. At present, the non-linear optics is indispensable part of the physics.

Till the discovery of laser, the matter had appeared to preserve the frequency of the light. From theoretical point of view it means, that the optical properties of the matter are linear with respect to propagating light. If we describe the matter as a system of

electric dipoles, this is expressed as

$$\mathbf{P}(\mathbf{r},t) = \varepsilon_0 \chi^{(1)} \mathbf{E}(\mathbf{r},t). \tag{2.1}$$

Eq. (2.1) relates the dipole density in a matter $\mathbf{P}$ with the total electric field $\mathbf{E}$. The vector $\mathbf{P}$ is termed polarization vector, ε_0 is the permittivity of vacuum, $\mathbf{r} = (x, y, z)$ is the coordinate vector and t indicates time. Eq. (2.1) can be physically interpreted as follows. When the electric dipoles are exposed to an electromagnetic wave, they start to oscillate. The oscillating dipoles radiate secondary waves, which superpose with the incident wave. The process results in different phase velocity of the wave in the matter than in vacuum. The relation (2.1) is valid for medium, which responds immediately on the local electric field $\mathbf{E}$/[1]. Moreover, the polarization properties of the medium are assumed to be polarization independent[2]. Therefore, the proportionality constant between electric field $\mathbf{E}$ and polarization vector $\mathbf{P}$ is a scalar quantity denoted as $\chi^{(1)}$. The constant $\chi^{(1)}$ is called dielectric susceptibility and in the visible spectrum usually reaches values around 1.

The situation is different if the medium does not respond instantly on the applied electric field $\mathbf{E}$. The polarization vector $\mathbf{P}(\mathbf{r},t)$ in time t is dependent on electric field $\mathbf{E}$ at the same point in the previous times. This can be expressed by the equation

$$\mathbf{P}(\mathbf{r},t) = \varepsilon_0 \int_{-\infty}^{t} dt' \, \Phi(t-t') \, \mathbf{E}(\mathbf{r},t'). \tag{2.2}$$

The function $\Phi(t-t')$ is called a response function. If we assume the electric field $\mathbf{E}$ to be composed of countable number of frequency components

$$\mathbf{E}(\mathbf{r},t) = \sum_n \mathbf{E}(\mathbf{r},\omega_n) \exp(-i\omega_n t), \tag{2.3}$$

equation (2.2) attains the form

$$\mathbf{P}(\mathbf{r},t) = \sum_n \varepsilon_0 \chi^{(1)}(\omega_m) \, \mathbf{E}(\mathbf{r},\omega_n) \, \exp(-i\omega_n t). \tag{2.4}$$

The function $\chi(\omega_n)$ is the frequency-dependent dielectric susceptibility. It is related to the response function $\Phi(t)$ by a Fourier transform $\chi(\omega_n) = \int_{-\infty}^{+\infty} dt' \, \Phi(t') \exp(i\omega_n t')$. If

[1] The polarization vector $\mathbf{P}(\mathbf{r},t)$ in time t is solely dependent on electric field $\mathbf{E}(\mathbf{r},t)$ in the same time.

[2] The direction of the polarization vector $\mathbf{P}$ is the same as direction of the electric field $\mathbf{E}$.

the polarization vector $\mathbf{P}$ is as well decomposed into the frequency components $\mathbf{P}(\mathbf{r},t) = \sum_n \mathbf{P}(\mathbf{r},\omega_n)\exp(-i\omega_n t)$, the relation between the electric-field amplitudes $\mathbf{E}(\mathbf{r},\omega_n)$ and polarization-vector amplitudes $\mathbf{P}(\mathbf{r},\omega_n)$ is obtained:

$$\mathbf{P}(\mathbf{r},\omega_n) = \varepsilon_0 \chi^{(1)}(\omega_n;\omega_n)\mathbf{E}(\mathbf{r},\omega_n). \tag{2.5}$$

In Eq. (2.5), we adopted the notation from [2], where the first argument in the permittivity tensor denotes the frequency of the polarization vector (wave emitted by the dipoles). The second argument is separated from the first argument by a semicolon and corresponds to frequency of the propagating electric field $\mathbf{E}$/[3].

In general, the non-linear properties and non-uniform directional polarizability of matter have to be taken into account. The polarization vector $\mathbf{P}$ is dependent on the electric field $\mathbf{E}$ in a more complex manner. Particularly, the polarization vector $\mathbf{P}(\mathbf{r},t)$ is treated as a general function of electric field $\mathbf{E}(\mathbf{r},t)$. For simplicity it is assumed, that the response of a matter is instant. The expansion of the polarization vector with respect to electric field to the second order reads [2]:

$$P_j(\mathbf{r},t) = \sum_k \varepsilon_0 \chi^{(1)}_{jk} E_k(\mathbf{r},t) + \sum_{kl} \varepsilon_0 \chi^{(2)}_{jkl} E_k(\mathbf{r},t) E_l(\mathbf{r},t). \tag{2.6}$$

The symbol P_j denotes the j-the component of the polarization vector $\mathbf{P}$ and the linear dielectric susceptibility tensor $\chi^{(1)}_{jk}$ is a generalization of the linear dielectric susceptibility written in Eq. (2.1). The quantity $\chi^{(2)}_{jkl}$ is called the second-order susceptibility tensor. It is non-zero only in material, which does not posses inversion symmetry. The terms of the tensor have values around 10^{-12} m/V. Thus, the corresponding effects are observable only with a strong coherent source of light[4].

When the matter exhibits finite response time with respect to the applied electric field $\mathbf{E}$, the dependence of the polarization vector $\mathbf{P}$ on spectral components of electric

[3] If the polarization vector $\mathbf{P}$ is linearly dependent on the electric field $\mathbf{E}$, the notation of incident and generated frequency in the dielectric susceptibility might appear to be redundant. On the other hand, when the non-linear phenomena are considered, the introduced notation appears to be helpful [2].

[4] The non-linear tensor $\chi^{(2)}_{klm}$ describes the polarization properties of the matter with respect to the product of two electric fields. Therefore, the associated observed effects are called quadratic or non-linear second-order effects.

field is expressed by the equation

$$\begin{aligned} P_j(\mathbf{r},t) &= \sum_k \sum_n \varepsilon_0 \chi^{(1)}_{jk}(\omega_n;\omega_n) E_k(\mathbf{r},\omega_n)\, \exp(-i\omega_n t) + \\ &\quad \sum_{kl} \sum_{mn} \varepsilon_0 \chi^{(2)}_{jkl}(\omega_m+\omega_n;\omega_m,\omega_n) E_k(\mathbf{r},\omega_m) E_l(\mathbf{r},\omega_n) \exp[-i(\omega_m+\omega_n)t]. \end{aligned} \tag{2.7}$$

The second-order permittivity tensor $\chi^{(2)}_{jkl}(\omega_m+\omega_n;\omega_m,\omega_n)$ is dependent on the frequencies of the incident fields ω_m, ω_n. The frequency of the associated polarization vector amplitude

$$P_j(\mathbf{r},\omega_m+\omega_n) = \sum_{kl} \sum_{mn} \varepsilon_0 \chi^{(2)}_{jkl}(\omega_m+\omega_n;\omega_m,\omega_n) E_k(\mathbf{r},\omega_m) E_l(\mathbf{r},\omega_n) \tag{2.8}$$

is equal to the sum of frequencies ω_m, ω_n of the interacting electric-field amplitudes $E_k(\mathbf{r},\omega_m), E_l(\mathbf{r},\omega_n)$. Therefore, the outgoing electromagnetic field, emitted by the dipoles, has different frequency then the two incident electric fields.

The interaction of the electromagnetic field in non-linear medium is classically described by the Maxwell equations

$$\nabla \times \mathbf{E} = -\frac{\partial \mathbf{B}}{\partial t}, \tag{2.9}$$

$$\nabla \times \mathbf{H} = -\frac{\partial \mathbf{D}}{\partial t} + \mathbf{j}, \tag{2.10}$$

$$\nabla \cdot \mathbf{D} = \rho, \tag{2.11}$$

$$\nabla \cdot \mathbf{B} = 0. \tag{2.12}$$

$\mathbf{E}$ denotes electric intensity field, $\mathbf{B}$ magnetic induction field, $\mathbf{H}$ magnetic intensity field, $\mathbf{D}$ displacement field, $\mathbf{j}$ free current density and ρ free charge density. The most of materials are non-magnetic for electromagnetic waves with frequencies in or near the visible spectral range. Therefore, the first material equation relating the vector of magnetic intensity field $\mathbf{H}$ with the vector of magnetic induction $\mathbf{B}$ reads

$$\mathbf{B}(\mathbf{r},t) = \mu_0 \mathbf{H}(\mathbf{r},t). \tag{2.13}$$

The second material equation relates the displacement field $\mathbf{D}$ with the electric intensity field $\mathbf{E}$. In medium, where dipole moments can be induced by the electric field, the relation is

$$\mathbf{D}(\mathbf{r},t) = \varepsilon_0 \mathbf{E}(\mathbf{r},t) + \mathbf{P}(\mathbf{r},t). \tag{2.14}$$

In the most of dielectrics, free currents and free charges are negligible, $\mathbf{j} = 0, \rho = 0$.

The currents and charges in the dielectric media originate solely from polarization of the medium [2].

If we insert Eqs. (2.13) and (2.14) into the Maxwell equations (2.9) – (2.12), we obtain

$$\nabla \times \mathbf{E} = -\frac{\partial \mathbf{B}}{\partial t}, \quad (2.15) \qquad \nabla \cdot \mathbf{E} = -\frac{1}{\varepsilon_0}\nabla \cdot \mathbf{P}, \quad (2.17)$$

$$\nabla \times \mathbf{B} = \varepsilon_0\mu_0\frac{\partial \mathbf{E}}{\partial t} + \mu_0\frac{\partial \mathbf{P}}{\partial t}, \quad (2.16) \qquad \nabla \cdot \mathbf{B} = 0. \quad (2.18)$$

In order to obtain the equation of motion for the electric field $\mathbf{E}$, a $\nabla\times$ operation on the Eq. (2.15) is performed and with the use of Eq. (2.16), we arrive at

$$\nabla \times \nabla \times \mathbf{E} = \nabla(\nabla \cdot \mathbf{E}) - \triangle\mathbf{E} = -\frac{1}{c^2}\frac{\partial^2 \mathbf{E}}{\partial t^2} - \mu_0\frac{\partial^2 \mathbf{P}}{\partial t^2}. \quad (2.19)$$

c indicates the speed of light in the vacuum. The term $\nabla(\nabla \cdot \mathbf{E})$ is usually negligible in comparison with the term $\triangle\mathbf{E}$, thus it can be omitted it in the next considerations [2]. Eq. (2.19) can be rearranged as follows

$$\triangle\mathbf{E} - \frac{1}{c^2}\frac{\partial^2 \mathbf{E}}{\partial t^2} = \mu_0\frac{\partial^2 \mathbf{P}}{\partial t^2}. \quad (2.20)$$

The polarization vector can be expanded to electric field components according to Eq. (2.7). If the electric field is expanded in the same manner [Eq. (2.3)], the coupled differential equations in space for different frequency components are obtained:

$$\triangle E_j(\mathbf{r},\omega_n) + \frac{\omega_n^2}{c^2}E_j(\mathbf{r},\omega_n) + \sum_k \frac{\omega_n^2}{c^2}\chi^{(1)}_{jk}(\omega_n;\omega_n)E_k(\mathbf{r},\omega_n) +$$

$$\sum_{(mo)}\sum_{kl}\frac{(\omega_m+\omega_o)^2}{c^2}\chi^{(2)}_{jkl}(\omega_m+\omega_o;\omega_m,\omega_o)E_k(\mathbf{r},\omega_m)E_l(\mathbf{r},\omega_o) = 0;\ \forall n. \quad (2.21)$$

The sum with index (mo) goes only through frequencies ω_m, ω_o, which satisfy the equation $\omega_n = \omega_m + \omega_o$. Eq. (2.21) governs the spatial evolution of electric-field spectral amplitudes $\mathbf{E}(\mathbf{r},\omega_n)$ in medium with non-zero second-order susceptibility tensor $\chi^{(2)}$. The equation couples spectral amplitudes $E_j(\mathbf{r},\omega_n)$, which correspond to distinct spectral components. Thus, an electric-field spectral amplitude at particular frequency may be affected by electric-field spectral amplitudes with different frequencies. This is the main principle of all non-linear processes. Eq. (2.21) can be further simplified in order

to obtain equation, which is more appropriate for analytical or numerical methods [2].

2.2 Non-linear process of the second order

A non-linear process of the second order involves interaction of three electric-field amplitudes. Two waves with frequency components ω_1 and ω_2 enter the interaction and one new frequency component ω_3 originates. Scheme of the process is shown in Fig. 2.1. The total electric field entering the interaction is equal to

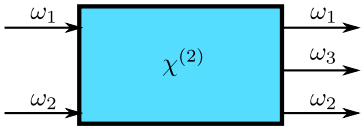

Figure 2.1: Scheme of the non-linear effect of the second order.

$$\mathbf{E}(\mathbf{r},t) = \mathbf{E}(\mathbf{r},\omega_1)\exp(-i\omega_1 t) + \mathbf{E}(\mathbf{r},\omega_2)\exp(-i\omega_2 t) + \text{c.c.} \tag{2.22}$$

Symbol c.c. denotes the complex conjugated part of the foregoing expression. If we include Eq. (2.22) into Eq. (2.7) and take only the non-linear part of the expression, we obtain

$$\begin{aligned}\mathbf{P}(\mathbf{r},t) \;=\; & \mathbf{P}(\mathbf{r},2\omega_1)\exp(-i2\omega_1 t) + \mathbf{P}(\mathbf{r},2\omega_2)\exp(-i2\omega_2 t) + \\ & \mathbf{P}(\mathbf{r},\omega_1+\omega_2)\exp[-i(\omega_1-\omega_2)t] + \mathbf{P}(\mathbf{r},\omega_1-\omega_2)\exp[-i(\omega_1-\omega_2)t] + \text{c.c.}\end{aligned} \tag{2.23}$$

The individual spectral components of the polarization vector are equal to

$$P_j(\mathbf{r},2\omega_1) = \varepsilon_0\chi^{(2)}_{jkl}(2\omega_1;\omega_1,\omega_1)E_k(\mathbf{r},\omega_1)E_l(\mathbf{r},\omega_1) \tag{2.24}$$

$$P_j(\mathbf{r},2\omega_2) = \varepsilon_0\chi^{(2)}_{jkl}(2\omega_2;\omega_2,\omega_2)E_k(\mathbf{r},\omega_1)E_l(\mathbf{r},\omega_1) \tag{2.25}$$

$$P_j(\mathbf{r},\omega_1+\omega_2) = 2\varepsilon_0\chi^{(2)}_{jkl}(\omega_1+\omega_2;\omega_1,\omega_2)E_k(\mathbf{r},\omega_1)E_l(\mathbf{r},\omega_2) \tag{2.26}$$

$$P_j(\mathbf{r},\omega_1-\omega_2) = 2\varepsilon_0\chi^{(2)}_{jkl}(\omega_1-\omega_2;\omega_1,-\omega_2)E_k(\mathbf{r},\omega_1)E^*_l(\mathbf{r},\omega_2). \tag{2.27}$$

There are several new frequency components, which originated from the non-linear interaction. The frequencies $\omega_3 = 2\omega_1, 2\omega_2$ belongs to the second harmonic and the process, in which the frequency components are generated, is called second-harmonic generation. The frequency $\omega_3 = \omega_1 + \omega_2$ is connected with the process termed sum-

frequency generation, and $\omega_3 = \omega_1 - \omega_2$ difference-frequency generation.

The generation of new frequency components by means of the second-order non-linearity [Eqs. (2.24) – (2.27)] can be explained microscopically. So far, the treatment of the non-linearity was purely mathematical. Its origin was established from expansion of polarization vector $\mathbf{P}$ in electric field $\mathbf{E}$. Nevertheless, if the microscopic structure of the matter is considered, the non-linear phenomena originate naturally.

In quantum mechanics, the total energy of the electromagnetic field is treated as a package of energetic quanta. Each quantum has an energy $\hbar\omega$ and the associated particle, which carries this energy, is called photon. The second-order processes involve interaction of two photons with one electron. The electron is assumed to be bounded in an orbit of an atom, which is located in the medium. When the electron absorbs the quanta or quantum of energy, it is excited to higher energy level according to the law of conservation of energy. The higher energy level may be either stable or a virtual one. The stable energy level originates from the parameters of the atom and the electron may occupy this level for sufficiently long time. In contrast, virtual energy level is not an energetic level of an atom, where electron may reside. Therefore, the electron is allowed to stay at this energetic level for restricted amount of time, which is defined by the Heissenberg inequality

$$\delta t = \hbar/\delta E. \tag{2.28}$$

δE is the energetic difference from the virtual level to closest real level of an atom. The transition times δt typically reach values around $10^{-15} - 10^{-16}$ s. Due to such a short times, the virtual transitions can be considered as instantaneous with respect to electromagnetic waves in the visible spectrum.

In the non-linear processes described in this thesis, the transitions trough the virtual levels are utilized. They allow for fast transition times of the electrons. Moreover, the transitions conserve energy of all involved photons. The processes, where only virtual energy levels of an electron are involved are called parametric. The transitions, which involve the real energy levels are called non-parametric. The transition times in non-parametric processes are much higher than in the case of parametric ones. Therefore, the exchange of energy between the photons and the medium has to be taken into the account. There might be as well effects, which may transform energy of photons to mechanical vibrations of the medium. In this case, there will be an absorption of the energy of the photons. Since the utilized energy levels are real, the resonance of the electric field with the electron transition causes the non-linear process to be resonantly enhanced. As a result, the probability of the transition can be much higher than in the

case of parametric process, but for the cost of additional absorption.

The simplest non-linear process of the second order is second-harmonic generation. It is connected with the non-linear polarization vector (2.24) and (2.25). It is described by transition scheme in Fig. 2.2(a). Two photons of the same frequency ω_1 are annihilated by an electron. Due to absorption of two energetic quanta $\hbar\omega_1$, the electron is excited from the ground state with energy E_g to virtual energy level with energy $E_g + 2\hbar\omega_1$. Till the defined time [Eq. (2.28)], the electron de-excites back to the original ground state. During the de-excitation process, the electron releases one photon with energy $2\hbar\omega_1$. The second-harmonic generation is a special case of more general process, the sum-frequency generation [Fig. 2.2(b)]. In sum-frequency generation two photons of arbitrary frequencies ω_1 and ω_2 are annihilated by an electron and one photon of frequency $\omega_1 + \omega_2$ is emitted. The physical explanation of the sum-frequency generation is identical to second harmonic generation.

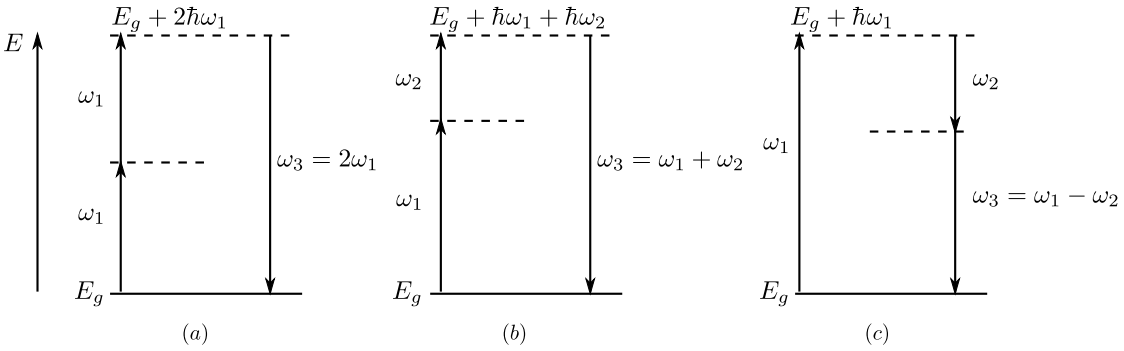

Figure 2.2: Electron transition schemes for (a) second-harmonic generation (b) sum-frequency generation (c) difference-frequency generation.

The last non-linear phenomenon of the second order is difference-frequency generation. Its transition scheme is shown in Fig. 2.2(c). There are two waves entering the interaction. Wave with positive frequency ω_1 and wave with negative frequency $-\omega_2$. We assume, that the frequency ω_1 is greater than ω_2. The outgoing wave has positive frequency

$$\omega_3 = \omega_1 - \omega_2. \tag{2.29}$$

Eq. (2.29) can be rearranged and multiplied by the reduced Planck constant $\hbar$. Then we obtain,

$$\hbar\omega_2 + \hbar\omega_3 = \hbar\omega_1. \tag{2.30}$$

Eq. (2.30) identifies the energy exchange between the interacting quantum fields, me-

diated by the electron. It can be explained as follows. The ingoing wave ω_1 releases one of its quantum $\hbar\omega_1$ to electron. The electron is excited to a virtual energy level with energy $E = E_g + \hbar\omega_1$. When electron de-excites, it releases one quantum of energy into the wave with frequency ω_2 and wave with frequency $\omega_3 = \omega_1 - \omega_2$. Besides the name difference frequency generation, the process can be as well called parametric down-conversion.

In the classical case[5], it has to be always assumed, that there are non-zero spectral amplitudes of interacting waves $\mathbf{E}(\mathbf{r}, \omega_n)$. If there is an ingoing wave with non-zero electric-field amplitude $\mathbf{E}(\mathbf{r}, \omega_1)$ and no external fields with frequencies ω_2, ω_3 entering the interaction [$\mathbf{E}(\mathbf{r}, \omega_2)$, $\mathbf{E}(\mathbf{r}, \omega_3) = 0$], the classical approach fails. It predicts that the waves with frequencies ω_2, ω_3 should not be generated. However, in the experiments, the generation of frequencies ω_2 and ω_3 is observed even if no external waves on the frequencies are provided.

In order to theoretically obtain the observed results, small non-zero amplitudes to the fields with frequencies ω_2 and ω_3 have to be introduced before the interaction. This ad-hoc solution is no longer needed when quantum-mechanical (QM) approach is used. The QM predicts, that there are non-zero vacuum fluctuations of the electromagnetic fields at an arbitrary frequency. As a result, if there are no externally provided fields with frequency ω_2 or ω_3, the energy from de-exciting electron is passed to the vacuum fluctuations of fields with frequencies ω_2 or ω_3. In analogy, the same problem arises for the second-harmonic generation as well as sum-frequency generation. They can be generated from the vacuum fluctuations in the same manner.

[5]The classical approach describes the non-linear interaction of the waves by the equations of coupled waves (2.21).

Chapter 3

Photon pairs

A brief historical background about the quantization of electromagnetic field is provided in Section 3.1.1. The quantization procedure of electromagnetic field in vacuum in the Coulomb gauge is shown in Section 3.1.2. The properties and usefulness of the photon pairs in physics, and particularly in quantum optics, are discussed in Section 3.2. In Section 3.3 the emission of photon pairs from a bulk birefringent crystal is briefly described as the simplest scenario of their generation. Subsequently, the procedures for obtaining the photon pairs entangled in frequency, emission angles and polarization are introduced.

3.1 Photons and quantization of the electromagnetic field

3.1.1 Introduction

A cornerstone for the quantization of an electromagnetic field was placed by Max Planck. At the turn of 19^{th} and 20^{th} century, he managed to theoretically solve the problem of radiation of a black body [3]. Till this time, there were two different formulas predicting the spectral density of black body radiation $u(\omega)$. The first one, proposed by Wilhelm Wien, approximated the spectral density for high frequencies

$$u(\omega) = C_1\omega^3 \exp\left(-C_2\frac{\omega}{T}\right); \tag{3.1}$$

C_1, C_2 are real positive constants and T is thermodynamic temperature. Although it was successful with predictions for the high frequencies, it failed in the low frequency limit. For the low frequency limit, there was a formula derived by Lord Rayleigh and

sir Jeans:

$$u(\omega) = \frac{2}{\pi}\omega^2 \frac{kT}{c^3}, \tag{3.2}$$

where k represents the Boltzmann constant. It was in agreement with the measurements of low-frequency part of black body spectrum. Although in low frequency limit, there was a discrepancy.

Max Planck was awared by the presence of two distinct formulas (3.1) and (3.2). By mathematical unification of entropies for both formula, he managed to derive an equation for spectral density of radiation:

$$u(\omega) = \frac{2\omega^2}{\pi c^3} \frac{\hbar\omega}{\exp(\hbar\omega/kT) - 1}, \tag{3.3}$$

which was able to predict the spectral density precisely across the whole spectral range. In order to obtain this formula, he was forced to take an unusual assumption. The energy of the radiation modes, which were in thermal equilibrium with the black body, had to be quantized. Particularly, each mode, which harmonically oscillated with frequency ω had to carry a discrete number of energy quanta $\hbar\omega$.

Together with Einstein's explanation of the photoeffect and observation of the spectral lines from emitting atoms, it started to be obvious, that quantization of en electromagnetic field is inherent part of the nature [3].

3.1.2 Quantization of the electromagnetic field

The quantization procedure in linear quantum optics composes of few stages [4]. First the wave equations of the vector potential $\mathbf{A}(\mathbf{r}, t)$ and scalar potential $\varphi(\mathbf{r}, t)$ are derived. The equations are solved with periodic boundary conditions. Then it is shown, that energy of the derived electromagnetic field in one periodic cell is equal to energy of infinite set of harmonic oscillators.

In the utilized approach, the potentials of the electromagnetic field are introduced. The equation stating non-existence of magnetic monopoles (2.18) and the Faraday law (2.15) are identically valid if we introduce the vector potential $\mathbf{A}$ as follows:

$$\mathbf{B} = \nabla \times \mathbf{A} \tag{3.4}$$

$$\mathbf{E} = -\frac{\partial \mathbf{A}}{\partial t} - \nabla\varphi. \tag{3.5}$$

We assume, that the medium through which the electromagnetic waves propagate is

vacuum. Then, the following material relations are valid:

$$\mathbf{B} = \mu_0 \mathbf{H}, \tag{3.6}$$

$$\mathbf{D} = \varepsilon_0 \mathbf{E}. \tag{3.7}$$

By inserting Eqs. (3.4) and (3.5) into the Ampere law (2.10) and the Coulomb law (2.11) and by usage of Eqs. (3.6) and (3.7), the equations of motion for potentials $\mathbf{A}$ and φ are obtained:

$$\triangle\varphi = -\nabla \cdot \frac{\partial \mathbf{A}}{\partial t} - \frac{\rho}{\varepsilon_0}, \tag{3.8}$$

$$\nabla \times \nabla \times \mathbf{A} = -\frac{1}{c^2}\frac{\partial^2 \mathbf{A}}{\partial t^2} - \frac{1}{c^2}\frac{\partial}{\partial t}\nabla\varphi. \tag{3.9}$$

Further, we will assume, that there are no free charges nor free currents. This means $\mathbf{j} = 0$ and $\rho = 0$. By the use of vector algebra and rearrangement of the terms in Eqs. (3.8) and (3.9), we get equations:

$$\begin{aligned} \Box\varphi &= -\frac{\partial}{\partial t}\left(\nabla \cdot \mathbf{A} + \frac{1}{c^2}\frac{\partial \varphi}{\partial t}\right) \\ \Box\mathbf{A} &= \nabla\left(\nabla \cdot \mathbf{A} + \frac{1}{c^2}\frac{\partial \varphi}{\partial t}\right). \end{aligned} \tag{3.10}$$

With the usage of Lorentz gauge

$$\nabla \cdot \mathbf{A} + \frac{1}{c^2}\frac{\partial \varphi}{\partial t} = 0, \tag{3.11}$$

which utilizes the non-uniqueness of the potentials $\mathbf{A}$ and φ, the wave equations for the potentials are obtained

$$\Box\varphi = 0, \tag{3.12}$$

$$\Box\mathbf{A} = 0. \tag{3.13}$$

The Lorentz gauge (3.11) can be further specified. In the investigated case it is possible to pass the Lorentz gauge (3.11) by defining

$$\nabla \cdot \mathbf{A} = 0 \wedge \varphi = 0. \tag{3.14}$$

The particular choice of gauge (3.14) is called the Coulomb gauge.

The procedure of quantization is independent of the shape of volume. Thus it will be assumed, that the radiation field is located in the cube of volume $V = L^3/^1$. It is further assumed that the complex solution of Eq. (3.13) is in the separable form,

$$\mathbf{A}^{(+)}(\mathbf{r}, t) = q(t)\mathbf{u}(\mathbf{r}). \tag{3.15}$$

Due to separability of the solutions (3.15), the wave equation for the vector potential (3.9) splits into two equations for functions q and $\mathbf{u}$

$$\begin{aligned} \triangle\mathbf{u} + \frac{\omega^2}{c^2}\mathbf{u} &= 0 & (3.16)\\ \frac{\mathrm{d}^2 q}{\mathrm{d}t^2} + \omega^2 q &= 0. & (3.17) \end{aligned}$$

The parameter ω originated from assumption of the separability. In order to obtain a solution of Eq. (3.16), the function $\mathbf{u}(\mathbf{r})$ is expanded into the plane-wave basis:

$$\mathbf{u}(\mathbf{r}) = \int_{-\infty}^{+\infty} d^3k\, A(\mathbf{k})\, \mathbf{e}(\mathbf{k})\, \exp(i\mathbf{k}\cdot\mathbf{r}). \tag{3.18}$$

The vector $\mathbf{e}(\mathbf{k})$ defines the polarization of the plane wave with wave vector $\mathbf{k}$, is real and its norm is equal to unity. The complex amplitude A covers magnitude of the wave and its phase shift. By insertion of Eq. (3.18) into Eq. (3.16) we obtain a dispersion relation between the wave vectors $\mathbf{k}$ and frequencies ω in the free space

$$\omega^2 = c^2\mathbf{k}^2. \tag{3.19}$$

The periodic boundary conditions at the edges of the quantization volume V require the function $\mathbf{u}(\mathbf{r})$ to fulfil the condition

$$\mathbf{u}(\mathbf{r}) = \mathbf{u}(\mathbf{r} + \mathbf{x}_0 L) = \mathbf{u}(\mathbf{r} + \mathbf{y}_0 L) = \mathbf{u}(\mathbf{r} + \mathbf{z}_0 L), \tag{3.20}$$

where $\mathbf{x}_0, \mathbf{y}_0, \mathbf{z}_0$ are the unit axis vectors. The requirement (3.20) is passed if the wave vectors are discretized, namely:

$$\mathbf{k}_l = \frac{2\pi}{L}(j, m, n), \tag{3.21}$$

where j, m, n are integers. The multi-index $l = (j, m, n)$ in the subscript of the wave

[1] The quantization in the free space limit can be done by expanding the volume V to infinity $V \to \infty$

vector includes the indexes j, m, n. While the wave vectors have become discrete, the angular frequencies ω have to be as well discretized. Therefore the frequencies are indexed with a multi-index l: ω_l.

After imposing the boundary conditions, the solution $\mathbf{u}(\mathbf{r})$ attains the form

$$\mathbf{u}(\mathbf{r}) = \sum_l A_l \mathbf{e}_l \exp(i\mathbf{k}_l \cdot \mathbf{r}) = \sum_l \mathbf{u}_l(\mathbf{r}). \tag{3.22}$$

The functions $\mathbf{u}_l$ are orthogonal and can be normalized such that

$$\int_V \mathbf{u}_l^*(\mathbf{r}) \cdot \mathbf{u}_m(\mathbf{r}) = \delta_{lm}. \tag{3.23}$$

The function $\mathbf{u}_l^*$ is complex conjugated to function $\mathbf{u}_l$ and δ_{lm} is the Kronecker delta. Then the form of function $\mathbf{u}_l$ is:

$$\mathbf{u}_l(\mathbf{r}) = \frac{1}{\sqrt{V}} \mathbf{e}_l \exp(i\mathbf{k}_l \cdot \mathbf{r}). \tag{3.24}$$

The spatial functions $\mathbf{u}_l(\mathbf{r})$ have to fulfil the Coulomb gauge (3.14), which means that:

$$\mathbf{e}_l \cdot \mathbf{k}_l = 0 \tag{3.25}$$

for all multi-indexes l. This implies, that the polarization vectors $\mathbf{e}_l$ are located in the transverse plane with respect to the wave vector $\mathbf{k}_l$. Thus, it is possible to decompose arbitrary vector $\mathbf{e}_l$ into the basis of two-dimensional space. This basis is formed by two vectors $\mathbf{e}_{l1}$ and $\mathbf{e}_{l2}$. The vectors $\mathbf{e}_{l1}, \mathbf{e}_{l2}$ are real and have norm equal to unity. The spatial function $\mathbf{u}(\mathbf{r})$ can be finally expressed as a superposition of mutually orthogonal modes $\mathbf{u}_l$:

$$\mathbf{u}(\mathbf{r}) = \sum_{l,\sigma} \frac{1}{\sqrt{V}} \mathbf{e}_{l\sigma} \exp(i\mathbf{k}_l \cdot \mathbf{r}), \tag{3.26}$$

where index $\sigma = 1, 2$ denotes the polarization of the wave.

The general solution of the differential equation (3.17) is

$$q_l(t) = A_{l\sigma}(\omega) \exp(-i\omega_l t) + A_{l\sigma}(-\omega) \exp(i\omega_l t), \tag{3.27}$$

in which $A_{l\sigma}(\omega_l)$, $A_{l\sigma}(-\omega_l)$ are complex numbers and $\omega_l = ck_l$ is a positive real number.

The resulting vector potential is given by the equation [5]

$$\begin{aligned}\mathbf{A}(\mathbf{r},t)=\sum_l \mathbf{u}_l(\mathbf{r})q_l(t) &= \sum_{\sigma l}\frac{1}{\sqrt{V}}\mathbf{e}_{l\sigma}\left[A_{l\sigma}(\omega_l)\exp(-i\omega_l t+i\mathbf{k}_l\cdot\mathbf{r})+\right.\\ &\left. A_{l\sigma}(-\omega_l)\,\exp(i\omega_l t+i\mathbf{k}_l\cdot\mathbf{r})\right]. \qquad (3.28)\end{aligned}$$

We break the sum into two parts and in the second sum the following identities are used $\sum_{l=-\infty}^{+\infty} g_l = \sum_{l=-\infty}^{+\infty} g_{-l}$, $\mathbf{k}_{-l}=-\mathbf{k}_l$, $\omega_l=\omega_{-l}$. Then, the obtained result is equal to

$$\begin{aligned}\mathbf{A}(\mathbf{r},t)=\sum_l \mathbf{u}_l(\mathbf{r})q_l(t) &= \sum_{l\sigma}\frac{1}{\sqrt{V}}\mathbf{e}_{l\sigma}\left[A_{l\sigma}(\omega_l)\,\exp(-i\omega_l t+i\mathbf{k}_l\cdot\mathbf{r})+\right.\\ &\left. A_{-l\sigma}(-\omega_l)\,\exp(i\omega_l t-i\mathbf{k}_l\cdot\mathbf{r})\right]. \qquad (3.29)\end{aligned}$$

We require the vector potential to be a real quantity. Thus, its complex conjugate must be equal to the original function $\mathbf{A}=\mathbf{A}^\dagger$. From this demand it follows that

$$A_{l\sigma}(\omega_l) = A^\dagger_{-l\sigma}(-\omega_l), \qquad (3.30)$$

$$A_{-l\sigma}(-\omega_l) = A^\dagger_{l\sigma}(\omega_l). \qquad (3.31)$$

Defining $A_{l\sigma}=A_{l\sigma}(\omega_l)$ the final solution for the vector potential reads

$$\begin{aligned}\mathbf{A}(\mathbf{r},t) &= \mathbf{A}^{(+)}(\mathbf{r},t)+\mathbf{A}^{(-)}(\mathbf{r},t)\\ &= \sum_{l,\sigma}\frac{\mathbf{e}_{l\sigma}}{\sqrt{V}}\left[A_{l\sigma}\,\exp(-i\omega_l t+i\mathbf{k}_l\cdot\mathbf{r})+A^\dagger_{l\sigma}\,\exp(i\omega_l t-i\mathbf{k}_l\cdot\mathbf{r})\right]. \qquad (3.32)\end{aligned}$$

The vector function $\mathbf{A}^{(+)}$ is complex conjugated to vector function $\mathbf{A}^{(-)}$, they denote the positive and negative frequency components of the vector potential $\mathbf{A}$. By insertion of Eq. (3.32) into the Hamiltonian of the electromagnetic field in the Coulomb gauge

$$H=\frac{1}{2}\int_V\left[\varepsilon_0\left(\frac{\partial\mathbf{A}}{\partial t}\right)^2+\frac{1}{\mu_0}\left(\nabla\times\mathbf{A}\right)^2\right] \qquad (3.33)$$

we arrive at

$$H=\sum_{l,\sigma}\frac{\hbar\omega_l}{2}(A^\dagger_{l\sigma}A_{l\sigma}+A_{l\sigma}A^\dagger_{l\sigma}). \qquad (3.34)$$

The Hamiltonian (3.34) is in the symmetric form with respect to complex amplitudes $A_{l\sigma}A^\dagger_{l\sigma}$. The final stage of the quantization procedure is the interchange between the amplitudes of the fields and creation and annihilation operators of linear harmonic

oscillator $A^\dagger_{l\sigma}A_{l\sigma} \rightarrow \hat{a}^\dagger_{l\sigma}, \hat{a}_{l\sigma}$. The commutation relations between the operators $\hat{a}^\dagger_{l\sigma}, \hat{a}_{l\sigma}$ is

$$[\hat{a}_{l\sigma}, \hat{a}^\dagger_{l'\sigma'}] = \hat{a}_{l\sigma}\hat{a}^\dagger_{l'\sigma'} - \hat{a}^\dagger_{l'\sigma'}\hat{a}_{l\sigma} = \delta_{\sigma\sigma'}\delta_{ll'}\mathbb{1}, \tag{3.35}$$

where the operator $\mathbb{1}$ is a unity operator.

After quantization of the field, the vector potential and Hamiltonian operator of the electromagnetic field are equal to:

$$\hat{\mathbf{A}}(\mathbf{r},t) = \sum_{l,\sigma} \mathbf{e}_{l\sigma}\left[\hat{a}_{l\sigma}\,\exp(-i\omega_l t + i\mathbf{k}_l\cdot\mathbf{r}) + \hat{a}^\dagger_{l\sigma}\,\exp(i\omega_l t - i\mathbf{k}_l\cdot\mathbf{r})\right], \tag{3.36}$$

$$\hat{H} = \sum_{l\sigma}\frac{\hbar\omega_l}{2}(\hat{a}^\dagger_{l\sigma}\hat{a}_{l\sigma} + \hat{a}_{l\sigma}\hat{a}^\dagger_{l\sigma}) = \sum_{l\sigma}\hbar\omega_l\left(\hat{a}^\dagger_{l\sigma}\hat{a}_{l\sigma} + \frac{1}{2}\right). \tag{3.37}$$

Operator of the number $\hat{n}$ of photons is defined as

$$\hat{n}_{l\sigma} = \hat{a}^\dagger_{l\sigma}\hat{a}_{l\sigma}. \tag{3.38}$$

Its eigenvectors are the Fock states $|n\rangle$ fulfilling

$$\hat{n}|n\rangle = n|n\rangle \tag{3.39}$$

and its eigenvalues are numbers of photons in given Fock states n. With the usage of the photon number operator $\hat{n}$, we may obtain mean number of photons in an arbitrary mode $l\sigma$ of a state $|\psi\rangle$. This can by computed from the equation

$$\langle n_{l\sigma}\rangle = \langle\psi|\hat{n}_{l\sigma}|\psi\rangle. \tag{3.40}$$

The symbol $\langle n_{l\sigma}\rangle$ indicates mean number of signal photons in mode $l\sigma$ of a multimode state $|\psi\rangle$.

3.2 Properties and usefulness of photon pairs

A photon pair is composed of two single-energetic quanta, which originate together in the spontaneous parametric down-conversion process (SPDC). SPDC is a quantum-mechanical phenomenon in which three quantum particles - photons interact together[2]. It was for the first time predicted by Luisell in 1961 [6] and experimentally observed independently by two research groups in 1968 [7,8]. During the process one photon of

[2]From classical point of view, the SPDC has been already described in Section 2.2 on page 20.

the pump field is annihilated and two other photons - signal and idler are created. The newly created particles are mathematically described by a common wavefunction - the two-photon state. This state describes all properties of both photons.

SPDC occurs only in a non-linear medium with a non-zero second-order susceptibility tensor $\chi^{(2)}$. In classical optics this tensor describes the non-linear capabilities of a medium, in SPDC it represents an interaction parameter. The magnitude of the parameter governs strength of the interaction. Despite of classical description of non-linear medium by a parameter, theoretical models of SPDC provide predictions which are in good agreement with experimental results [9–12].

Theoretical predictions and experimental results reveal that two-photon states do not offer deterministic results of measurements like the classical objects do. Just the opposite, there can be many various statistically correlated states but only one of them is detected [13]. These states, termed entangled, have served for performing many through-braking experiments like the test of Bell inequalities. Testing of the inequalities have revealed non-locality or non-realism of quantum phenomena [14, 15]. The photon pairs were as well used for testing EPR paradox [16–18] or quantum teleportation [19]. Besides the teleportation schemes, entanglement can be used for secured quantum key distribution [20,21]. Last but not least, entanglement also plays a crucial role in quantum computing [22, 23], quantum metrology [24, 25] and quantum object identification [26]. Till now, photon pairs were the exclusively experimentally obtainable entangled particles. However at present, entanglement can be established between the single atoms [27].

In the process of annihilation of a pump photon and creation of signal and idler photons, the laws of energy and momentum conservation have to be fulfilled. The law of conservation of energy is expressed as:

$$\hbar\omega_p = \hbar\omega_s + \hbar\omega_i. \tag{3.41}$$

The frequencies ω_p, ω_s and ω_i belong to pump, signal and idler photons. The law of conservation of momentum equals[3]

$$\hbar\mathbf{k}_p = \hbar\mathbf{k}_s + \hbar\mathbf{k}_i, \tag{3.42}$$

where $\mathbf{k}_p$, $\mathbf{k}_s$ and $\mathbf{k}_i$ are wave vectors of pump, signal and idler field.

[3]The law of conservation of momentum in the Eq. (3.42) is valid, if the non-linear medium is homogeneous on lengths many times higher than the wavelengths of the interacting photons. Otherwise a more general formula has to be used for the evaluation of conservation of momentum.

Strong statistical correlations between newly created photons arise due to these laws. The correlations may arise in variables such as frequency, wave vector or polarization. They provide us availability to predict properties of one photon by measuring properties of the other one. Generally, this implies that signal and idler photons are not independent particles. The nature of correlations is closely related to geometry and optical properties of the non-linear medium and shape of the pump pulse [28–31].

The energy conservation makes signal and idler photons to be created in a narrow temporal window. In addition, the law determines the sum frequency of down-converted photons. Time correlations can be observed in Hong-Ou-Mandel interferometer by measuring a correlation function of the 4^{th} order [11,28] (see scheme of the interferometer in Fig. 3.1). Measurement is based on detecting coincidences between two spatially and temporally separated photons. Time correlations can be tailored by the shape of the pump field in the time domain or by precise design of the non-linear structure [28]. By proper design of these parameters, frequency chirped two-photons states [32], anti-correlated states [33] or non-correlated two-photon states [29] can be obtained.

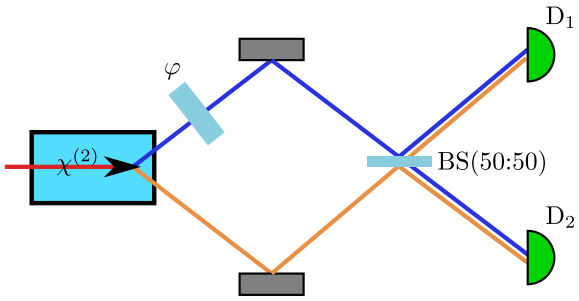

Figure 3.1: Scheme of the Hong-Ou-Mandel interferometer together with non-linear crystal.

The momentum conservation leads to correlations in wave vectors. Satisfying this law is crucial for effectivity of SPDC and it is termed phase-matching. At first, birefrigent materials passed this requirement, later photonic structures have started to being used. In modern photonic structures periodicity in a strucutre, in linear regime - refraction index or in non-linear regime - periodical poling, is introduced to provide a desired phase-matching condition [34,35]. Correlation in wave vectors is closely connected with emission angles of the photons from the structure. When one photon is observed at a given direction the direction of the other one is fully determined or can be located in a cone volume with certain probability [30,31,36]. Which one of these possibilities occurs depend on the geometry of the crystal and spatial parameters of the pump pulse.

The spatial correlations, which are connected with the wave vector correlations, are investigated in connection with, e.g., ghost imaging [37] or Schmidt modes [31][4].

Last important degree of freedom in which a correlations may occur is polarization [39,40]. There are two distinct polarization states in which the signal and idler photons can be created. One is orthogonal to the other or both of them have the same direction of polarization and the pump has different polarization from them. The first one is called type-II generation and the second is type-I generation. Polarization states are easy to calculate with and handle them in experiments. Therefore, this type of correlation is a suitable platform for many experiments. It has been used, e.g., for demonstration of quantum teleportation [13], violation of Bell unequalities [15] or test of EPR paradox [18].

3.3 Generation of photon pairs in bulk material

Photon pairs are generated in non-centrosymmetric crystals[5]. Typical examples are $KNbO_3$, $LiIO_3$, $LiNbO_3$, or $\beta-BaB_2O_4$ [3]. In the crystal, there are no preferred directions of emission or frequencies of the signal and idler photons ω_s and ω_i. Therefore, the photons are emitted at all allowed frequencies and in all directions governed by the conservation laws.

The simplest way how to obtain the photon pairs is their generation from birefringent bulk crystal. If the pump beam has a transverse spatial profile of a plane wave and is monochromatic, the photon pairs are emitted in the vicinity of two cone surfaces. Particularly, the wave vectors of the emitted photons form the cones. The orientation and alignment of the cone surfaces are determined by the phase-matching condition. The condition states, that the wave vectors of pump beam, signal and idler photons $\mathbf{k}_p, \mathbf{k}_s, \mathbf{k}_i$ have to fulfil the conservation law of momentum (3.42). This implies, that the wave vectors have to lie in one plane. Therefore, if we select a plane, in which a pump wave vector is located, the cross section of the plane with the cone surfaces uniquely determine the wave vectors (directions of emission) of the signal and idler photons in a pair.

The photon pairs are correlated in all variables. Namely in frequency, wave vector and polarization. The photons entangled in frequency can be obtained by selecting a small neighbourhood of two particular directions of emission. The directions of emission

[4]The Schmidt modes can be as well introduced in frequency region. Their number determines the amount of entanglement between the photons in a pair [38].

[5]Non-centrosymmetric media posses non-zero second-order susceptibility tensor $\chi^{(2)}$.

have to fulfil the conservation law of momentum. The directions can be experimentally filtered by small apertures of finite diameters. After that, we obtain a state, which is entangled in frequencies. It is approximately described by the formula

$$|\psi\rangle = |\mathrm{vac}\rangle + \iint_{-\infty}^{+\infty} d\omega_s d\omega_i \, \xi(\omega_s, \omega_i) \, \delta(\omega_p - \omega_s - \omega_i) |\omega_s\rangle_s |\omega_i\rangle_i. \tag{3.43}$$

The function $\xi(\omega_s, \omega_i)$ represents a probability amplitude with which the photon pairs with given frequencies are emitted, function $\delta(\omega_p - \omega_s - \omega_i)$ represents the law of energy conservation and couples frequencies of the signal and idler photons in a pair. The indices of the states s and i determine the signal and idler photons. Polarization of the photons is neglected in this case. The vacuum state $|\mathrm{vac}\rangle$ in Eq. (3.43) represents vacuum fluctuations of photons which were not converted to single energetic quanta.

The photons correlated in emission directions can be extracted by selecting precisely defined directions of two photon pairs. Each pair has to fulfil the conservation law of momentum and conservation law of energy. Then, the obtained two-photon state is

$$|\psi\rangle = |\mathrm{vac}\rangle + (|a\rangle|b\rangle + |a'\rangle|b'\rangle). \tag{3.44}$$

The states $|a\rangle, |b\rangle, |a'\rangle, |b'\rangle$ are single photon states propagating in the selected directions a, b, a', b'.

There are two distinct photon-pair states entangled in polarization. The first one consists of photon pairs, where the polarizations of signal and idler photons are orthogonal:

$$|\psi\rangle = \sqrt{1-\alpha^2}|\mathrm{vac}\rangle + \alpha\Big[|\uparrow\rangle_A|\rightarrow\rangle_B + |\rightarrow\rangle_A|\uparrow\rangle_B\Big]; \tag{3.45}$$

α is a real number and satisfies the inequality $\alpha^2 \leq 1$. The state $|\rightarrow\rangle$ denotes, that the photon has horizontal polarization and state $|\uparrow\rangle$ assigns a photon vertical polarization. The indices A and B denote directions of the emitted photons. The other photon pair state is formed by photon pairs, where photons have the same polarization. The two-photon state in this case equals

$$|\psi\rangle = \sqrt{1-\alpha^2}|\mathrm{vac}\rangle + \alpha\Big[|\uparrow\rangle_A|\uparrow\rangle_B + \alpha|\rightarrow\rangle_A|\rightarrow\rangle_B\Big]; \, \alpha^2 \leq 1. \tag{3.46}$$

The state in Eq. (3.45) is generated in alignment called type II. The second state (Eq. (3.46)) is generated in alignment called type I. In the type II SPDC, the photons with orthogonal polarizations are emitted at surfaces of two cones, which intersect each other. The intersections define two directions in which photons of both polarizations

can be emitted. There is the same probability, that a photon in direction A has a vertical polarization $\uparrow$ simultaneously with the photon in direction B having horizontal polarization $\rightarrow$ like in the case, when the polarizations are interchanged. The entangled state of photons (3.46) can be obtained by emission from two crystals located close to each other. Both crystals have to be conveniently cut and turned by 90 deg in the transverse plane with respect to each other. Then the crystals are aligned such that, their optical axes are orthogonal. It is further assumed that the generation occurs only for polarization of the pump wave oriented along the optical axis of the crystal and the non-linear tensor $\chi^{(2)}$ allows for generation likely polarized signal and idler photons. By use of the polarization of the pump wave, which is declined from the axes of both crystals by 45 deg, the cone emission patterns similar to single crystal can be observed. The state (3.46) is be obtained by selection of two directions from the cone, which satisfy the law of conservation of momentum and energy.

Chapter 4

Generation of photon pairs in a ring fiber

Integrated sources of photon pairs are introduced in Section 4.1.1. The guidance of modes with a defined OAM in fibers and waveguides is discussed in Section 4.1.2. The importance and applications of the OAM modes is as well mentioned. Section 4.1.3 is devoted to the concept of quasi-phase matching and thermal poling process.

The theoretical description of SPDC in a ring fiber is developed in Section 4.2. The theoretical framework is based on quantum-mechanical approach, where the Schrödinger equation is solved by means of perturbation series to the first order. Definitions of quantities characterizing a photon pair are provided at the end of the Section.

The theory describing decomposition of modes of the ring fiber into the basis of OAM operator eigenfunctions is introduced in Section 4.3. In addition, decomposition of a two-photon amplitude into the Schmidt basis in frequency and spatial domain is described.

Section 4.4 includes characterization of the guided modes of the ring fiber. Eigenmodes of the ring fiber are derived and procedure for computation of the propagation constants of the fiber is described. Effective refractive indices of the modes are shown. The most stable modes obeying the conservation law of OAM are identified as suitable for the non-linear interactions. Their transversal profiles together with angular spectral components are shown and discussed.

Narrow-band non-linear interaction of the pump beam with OAM number $l_p = +1$ with the signal and idler modes having OAM numbers $l_s = +1$ and $l_i = 0$ is investigated in Section 4.5. Stability of the interacting modes is analyzed by means of an effective index of refraction. The results of simulation of the non-linear interaction are shown.

Particularly, phase-matching conditions and mean signal photon-number spectra are discussed.

The non-linear interaction of pump beam with OAM number $l_p = 0$ with the signal and idler fields in TE_{01} modes is investigated in Section 4.6. Width of the mean signal photon-number spectrum and correlation times are compared with the results obtained for the narrow-band process in Section 4.5.

The entanglement of photon pairs generated by the pump beam with OAM number $l_p = 0$ and Gaussian time profile is investigated in Section 4.7. The two-photon amplitude in spatio-spectral coordinates is analyzed in order to determine the number of Schmidt modes. The maximal effective dimension of the entangled space is evaluated. The influence of noise on entanglement of the generated state is evaluated by means of the Clauser-Horne-Shimony-Holt inequalilty.

4.1 Introduction

4.1.1 Integrated sources of photon pairs

Entangled photon pairs can be generated from fiber or waveguide sources with $\chi^{(2)}$ non-linearity. Rectangular periodically-poled waveguides made of PPKPT or $LiNbO_3$ [41–44] represent well-developed and highly-efficient photon-pair sources. They can provide photon pairs entangled in polarization on degenerate and non-degenerate frequencies as well as non-correlated photons. $LiNbO_3$ and KTP have large coefficients of non-linear tensor $\chi^{(2)}$, typically between $10 - 30$ pm/V. Thus, they may be highly bright sources of photon pairs. Particularly, they are able to emit $10^2 - 10^3$ photon pairs per second per microwatt. On the other hand, there are fiber sources of photon pairs. For example, a periodically poled silica (SiO_2) fibre produces around 10 photon pairs per second per microwatt and can be utilized for the generation of polarization entangled photon pairs in a broad spectral range [45]. This is about two orders of magnitude less than in the case of the waveguides. The lower efficiency comes from lower value of the terms of non-linear tensor $\chi^{(2)} \sim 10^{-2}$ pm/V. But the length of the fibers can be one order of magnitude higher in comparison with the waveguides[1]. The longer non-linear grating then compensates for the lower value of the terms of non-linear tensor $\chi^{(2)}$.

The modes of waveguides reflect their rectangular transverse profiles that cannot be easily and effectively transformed into modes of fibers. Especially, they are unable

[1] The periodically poled grating can be uniformly introduced in fibers with lengths up to 1 m. The periodically poled waveguides are usually up to 10 cm long.

to guide modes with radial symmetry without distortion. On the other hand, there exist structured photonic waveguides with eigenmodes close to OAM modes [46, 47]. Unfortunately, these fibers have transverse profiles typically few tens of micrometers wide and so they are not suitable for poling. Thus, the only fibers, which combine the features of non-linearity and radial symmetry are the investigated ring shaped fibers. Though only weakly non-linear [45], they may be source of photon pairs with radially symmetric spatial modes. The detailed analysis of SPDC in the periodically poled ring fiber has been carried out in [A1, A2].

4.1.2 Guided OAM modes

The ring fibers are able to steadily guide modes with a defined OAM [46–49]. Such modes have been theoretically studied [48,49] and experimentally characterized recently [48] using a ring [Fig. 4.1(a)] or vortex geometry (concentric rings) of optical fibers. This geometry allows to separate modes of the LP_{11} family[2] that differ in their effective refractive indices. This results in their stable propagation with a low ratio of crosstalk for lengths over 1 km [48]. Such stable states of OAM can then be exploited to multiplex data and rise the transfer capacity of channels.

OAM fields are beneficial for both the classical and quantum areas of physics. Sufficiently strong (classical) fields are namely useful for nano-particle manipulations [52]. From the point of view of quantum communications that use individual photon pairs, entangled states are crucial. As we show below, the process of SPDC in thermally poled silica fibers allows to generate photon pairs entangled in different degrees of freedom. These fibers then represent sources of entangled photons that can be directly integrated into optical fiber networks [45]. The entanglement in OAM numbers offers additional advantage for the construction of division multiplexing systems [48]. OAM multi/demultiplexers have been recently addressed in [53]. Efficiency of these systems has been characterized via the crosstalk between demultiplexed OAM modes (the maximum value equaled -8 dB) and total losses (~ 18 dB). The entangled OAM fields also allow to implement various quantum computation protocols including the above mentioned quantum random walks [54,55] and a CNOT gate [56]. Last but not least, OAM fields have been found extraordinarily useful in the area of atomic physics where they enable enhanced control of transitions between atomic levels [57].

[2] LP_{mn} is a group of guided modes of radially symmetric fiber with slightly different propagation constants [50, 51]. The integers m, n categorize the modes.

4.1.3 Periodical poling of the silica fiber

The non-linear fibers are being poled in order to pass the conservation law of momentum [58,59]. The process of poling involves local introduction of non-zero non-linear tensor $\chi^{(2)}$. The technique of achieving the momentum conservation is called quasi-phase-matching. When the poling process is periodically repeated over the length of the fiber, a non-linear grating $\chi^{(2)}$ originates. The grating introduces additional momentum into the process. The law of conservation of momentum then reads

$$\mathbf{k}_p - \mathbf{k}_s - \mathbf{k}_i + \mathbf{G}_m = 0, \tag{4.1}$$

where the vector $\mathbf{G}_m$ belongs to the non-linear grating. It may attain different values according to the order m. At microscopic level, a poled domain can be considered as a volume of dipoles, which behave in a non-linear manner. When the dipoles are driven by the electric field of the pump beam, they emit waves with distinct harmonic components. The wave contributions from all the emitting dipoles superpose and form the outgoing wave. The proper space alignment of the non-linear domains cause the contributions from individual dipole domains to add constructively. As a result, the non-linear process is enhanced.

In the case of waveguides and fibers, there is only one homogeneous direction, the longitudinal one. Then the equation for the momentum conservation (4.1) reaches a scalar form

$$\beta_p - \beta_s - \beta_i + \frac{2\pi}{\Lambda} m = 0. \tag{4.2}$$

The variables β_p, β_s and β_i indicate propagation constants[3] of pump, signal and idler fields. The remaining term in the equation is the longitudinal component of the wave vector of the non-linear grating $\mathbf{G}_m$. It depends on the integer m, which means, that the phase matching condition can be satisfied in multiple ways. In practise, only few orders m may significantly contribute to the emission of photons. Usually only the most intense order m_0 is utilized. Nevertheless, there are proposals for utilization of the higher orders, which increases a versatility of a photon source [60]. The Eqs. (4.1) and (4.2) are exactly valid for infinitely long grating. In practise, the grating incorporates finite number periods, usually more then one hundred. In these cases, the equation (4.2) provides us the condition of the most intense generation.

There are many types of materials with various physical properties, which can be

[3] Propagation constant is a component of the wave vector in the direction of propagation. This term is used mainly in connection with the waveguides or fibers.

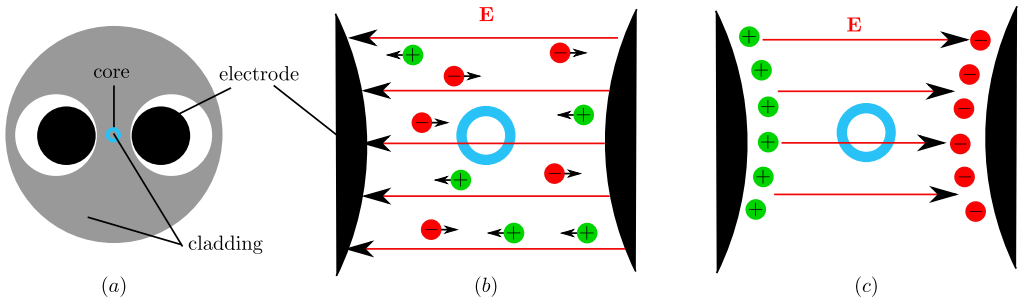

Figure 4.1: (a) A scheme of the twin-hole fiber (b) Process of thermal poling (c) The positions of electrons and ions after the poling process.

periodically poled. Therefore, different techniques for periodical poling have to be utilized [61–64]. Particularly, the process of periodical poling of $\chi^{(2)}$ susceptibility in silica fibers has already been mastered [65–67]. It allows to achieve phase matching of the non-linearly interacting fields, together with the conservation law of energy. During the poling, a SiO_2 material with no natural $\chi^{(2)}$ susceptibility (due to symmetry) is heated up and exposed to a strong electric field $\mathbf{E}$ originating in the electrodes inserted in the fiber [Fig. 4.1(b)]. The free ions in the fiber are dragged by the field and form the macroscopic charge nearby the electrodes. When the material is cooled down back to the room temperature, the electric field is switched off. However, the ions remain frozen at their positions and form a permanent internal static electric field $\mathbf{E}$ [Fig. 4.1(c)], [67,68]. This field is responsible for quadratic non-linear properties of the fiber. The non-linear grating is created by a UV erasure process that removes the non-linearity inside domains exposed to a UV laser. Suitable choice of the grating period Λ then allows to reach quasi-phase-matching of the non-linear process.

Photon pairs in fibers can also be generated via the process of four-wave mixing using $\chi^{(3)}$ susceptibility available in common optical fibers. However, there also occur other competing non-linear processes based on $\chi^{(3)}$ susceptibility (Raman scattering). Their presence results in larger values of single-photon noise superimposed on photon-pair fields. Despite this, a lot of attention has been devoted to such sources emitting photon pairs both around 800 nm and 1550 nm [69–71].

4.2 Theoretical description

Non-linear process of SPDC occurring among the pump (p), signal (s) and idler (i) fields can be described by the following interaction Hamiltonian $\hat{H}_{\text{int}}$ [72]:

$$\begin{aligned}\hat{H}_{\text{int}}(t) &= 2\varepsilon_0 \int_{S_\perp} r dr\, d\theta \int_{-L}^{0} dz\, \chi^{(2)}(z) : \mathbf{E}_p^{(+)}(r,\theta,z,t) \\ &\quad \times \hat{\mathbf{E}}_s^{(-)}(r,\theta,z,t)\hat{\mathbf{E}}_i^{(-)}(r,\theta,z,t) + \text{h.c.} \end{aligned} \tag{4.3}$$

Symbol : means tensor shorthand with respect to its three indices, ε_0 denotes the vacuum permittivity and h.c. replaces the Hermitian conjugated term. A vector positive-frequency electric-field amplitude of a pump beam is denoted as $\mathbf{E}_p^{(+)}(r,\theta,z,t)$ whereas vector negative-frequency electric-field operator amplitudes of the signal and idler beams are described as $\hat{\mathbf{E}}_s^{(-)}(r,\theta,z,t)$ and $\hat{\mathbf{E}}_i^{(-)}(r,\theta,z,t)$, respectively. Non-linear susceptibility $\chi^{(2)}$ is assumed z-dependent. Its spatial periodic rectangular modulation along the z axis (Fig. 4.2) with certain period permits quasi-phase-matching of the non-linear process. Hamiltonian $\hat{H}_{\text{int}}$ in Eq. (4.3) is written in cylindrical coordinates with radial variable r, angular variable θ and longitudinal variable z. Symbol $S_\perp$ denotes the transverse area of the fiber of length L.

After the process of thermal poling, a static electric field is established in the area of the core of the fiber [67] (for details see Sec. 4.1.3). The static electric field, oriented in the direction of axis x interacts with the silica's non-linear tensor of the the third order $\chi^{(3)}$ [2, 73][4]. The origin of the effective $\chi^{(2)}$ tensor is explained by interaction of the static electric field $\mathbf{E}_0$ with dynamical electric field $\mathbf{E}$ through the non-linear tensor of the third order $\chi^{(3)}$:

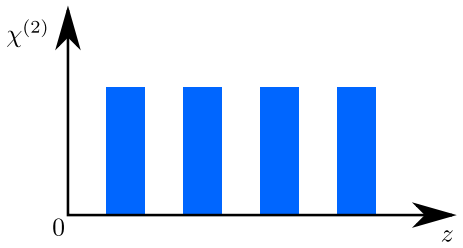

Figure 4.2: Modulation of non-linear tensor of the second order $\chi^{(2)}$ along the axis of the twin-hole fiber z.

$$\begin{aligned}&\chi^{(3)}_{jklm}(E_k + E_{0,k})(E_l + E_{0,l})(E_m + E_{0,m}) \rightarrow \\ &\qquad \chi^{(3)}_{jklm}E_{0,k}E_lE_m + \chi^{(3)}_{jklm}E_kE_{0,l}E_m + \chi^{(3)}_{jklm}E_kE_lE_{0,m} \\ &\qquad = 3\chi^{(3)}_{jklm}E_{0,k}E_lE_m = 3\chi^{(3)}_{jxlm}E_0E_lE_m = \chi^{(2)}_{jlm}E_lE_m. \end{aligned} \tag{4.4}$$

The electric field components $E_{0,j}$ belong to static electric field with magnitude equal to

[4] The values of the coefficients of silica's non-linear tensor of third order $\chi^{(3)}$ are at the level of 10^{-22} m^{2}V^{-2}.

E_0. The electric field components E_j correspond to additional dynamical electric field. In the Eq. (4.4), the terms, which follow the arrow sign effectively correspond to the non-linear processes of the second order. The terms, which are effectively assigned with the non-linear processes of the third order and linear processes, have been omitted[5]. In the Eq. (4.4), it was explicitly substituted for the static electric field $E_{0,j} = \delta_{jx} E_0$. The effective second-order susceptibility tensor $\chi^{(2)}_{jlm}$ then originated as a product of the static electric field $E_{0,x}$ with the third order non-linear tensor $\chi^{(3)}_{jxlm}$. As a consequence, thermal poling of SiO_2 material giving non-linearity to the fiber results in the following non-zero elements of $\chi^{(2)}$ tensor: $\chi^{(2)}_{xxx} \simeq 3\chi^{(2)}_{xyy}$ and $\chi^{(2)}_{xyy} = \chi^{(2)}_{yyx} = \chi^{(2)}_{yxy} = 0.021$ pm/V [2,74].

In the considered ring fiber with its rotational symmetry[6] around the z axis, the pump, signal and idler fields can be decomposed into transverse eigenmodes $\mathbf{e}_\eta(r,\theta,\omega)$ with propagation constants $\beta_\eta(\omega)$ at the appropriate frequencies ω. Multi-index η contains a mode name [51] including azimuthal (n) and radial indices and polarization index ϕ. In this decomposition, the strong (classical) positive-frequency electric-field pump amplitude $\mathbf{E}_p^{(+)}$ attains the form

$$\begin{aligned} \mathbf{E}_p^{(+)}(r,\theta,z,t) &= \sum_{\eta_p} A_{p,\eta_p} \int d\omega_p \, \mathcal{E}_p(\omega_p) \, \mathbf{e}_{p,\eta_p}(r,\theta,\omega_p) \\ &\quad \times \exp\left[i\beta_{p,\eta_p}(\omega_p) z - i\omega_p t\right], \end{aligned} \tag{4.5}$$

in which A_{p,η_p} gives the amplitude of mode η_p and $\mathcal{E}_p$ stands for the pump normalized amplitude spectrum. As the normalized eigenmodes $\mathbf{e}_\eta(r,\theta,\omega)$ form a basis, they can be used for quantization of the signal- and idler-field photon fluxes [75,76]. As a consequence, the negative-frequency electric-field signal and idler operator amplitudes $\hat{\mathbf{E}}_s^{(-)}$ and $\hat{\mathbf{E}}_i^{(-)}$ can be expressed as

$$\begin{aligned} \hat{\mathbf{E}}_a^{(-)}(r,\theta,z,t) &= \sum_{\eta_a} \int d\omega_a \sqrt{\frac{\hbar\omega_a}{4\pi\varepsilon_0 c \bar{n}_{a,\eta_a}}} \, \hat{a}^\dagger_{a,\eta_a}(\omega_a) \\ &\quad \times \mathbf{e}^*_{a,\eta_a}(r,\theta,\omega_a) \exp\left[i\beta_{a,\eta_a}(\omega_a) z - i\omega_a t\right], \; a = s,i; \end{aligned} \tag{4.6}$$

[5] In terms, which effectively belong to non-linear processes of the third order, the components of static electric field $E_{0,j}$ are not present. While in the linear terms, the components of the static electric field $E_{0,j}$ are present with the power of two. As a result, it modulates the linear index of refraction.

[6] The ring fibers partially loose their radial symmetry owing to the presence of two thin metallic wires used for thermal poling. However, the holes with wires are usually far from the fiber core and so their influence to radial symmetry of fiber modes results in only weak anisotropy that can usually be omitted [74].

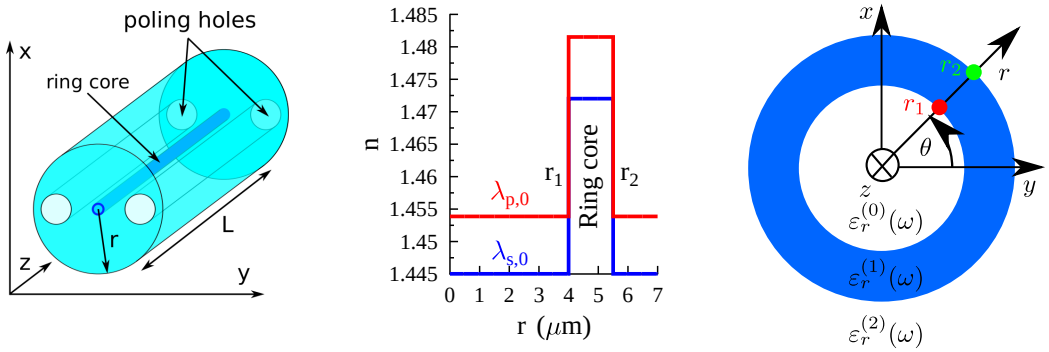

(a) (b) (c)

Figure 4.3: (a) Sketch of a ring fiber with two small poling holes (b) Radial profiles of indices of refraction n at the pump ($\lambda_p^0 = 0.775\ \mu m$) and signal ($\lambda_s^0 = 1.55\ \mu m$) wavelengths (c) Cross-section of the fiber with corresponding linear dielectric permitivitties.

$\hbar$ is the reduced Planck constant, c speed of light in the vacuum and $\bar{n}_{a,\eta_a}$ effective index of refraction for mode η_a of field a ($\bar{n}_{a,\eta_a} = c\beta_{a,\eta_a}/\omega_a$). The boson creation operators $\hat{a}^\dagger_{a,\eta_a}(\omega_a)$ in Eq. (4.6) add one photon into mode a with index η_a and frequency ω_a. The eigenmodes are normalized such that $\int r dr d\theta \, |\mathbf{e}_{a,\eta_a}(r,\theta,\omega_a)|^2 = 1$.

For the considered ring fiber composed of SiO_2 cladding and SiO_2 core doped by 19.3 mol% of GeO_2 [for the scheme, see Fig. 4.3(c)] [77, 78], the normalized electric-field eigenmodes $\mathbf{e}_\eta(r,\theta,\omega)$ together with the accompanying normalized magnetic-field eigenmodes $\mathbf{h}_\eta(r,\theta,\omega)$ can be obtained analytically. Their longitudinal z components can be expressed in terms of Bessel functions of the first (J_n) and second (Y_n) kind and modified Bessel functions of the first (I_n) and second (K_n) kind as follows [50]:

$$\begin{aligned}
e_{z,\eta}(r,\theta,\omega) &= \Big\{ C_\eta^{(0)}(\omega) I_n(w_\eta^{(0)} r) \mathrm{rect}_{0,r_1}(r) \\
&+ \Big[C_\eta^{(1)}(\omega) J_n(w_\eta^{(1)} r) + D_\eta^{(1)}(\omega) Y_n(w_\eta^{(1)} r) \Big] \mathrm{rect}_{r_1,r_2}(r) \\
&+ D_\eta^{(2)}(\omega) K_n(w_\eta^{(2)} r) \mathrm{rect}_{r_2,\infty}(r) \Big\} \sin(n\theta + \phi), \\
h_{z,\eta}(r,\theta,\omega) &= \Big\{ A_\eta^{(0)}(\omega) I_n(w_\eta^{(0)} r) \mathrm{rect}_{0,r_1}(r) \\
&+ \Big[A_\eta^{(1)}(\omega) J_n(w_\eta^{(1)} r) + B_\eta^{(1)}(\omega) Y_n(w_\eta^{(1)} r) \Big] \mathrm{rect}_{r_1,r_2}(r) \\
&+ B_\eta^{(2)}(\omega) K_n(w_\eta^{(2)} r) \mathrm{rect}_{r_2,\infty}(r) \Big\} \cos(n\theta + \phi).
\end{aligned} \tag{4.7}$$

Function $\mathrm{rect}_{a,b}(r)$ equals 1 for $r \in < a, b >$ and is zero otherwise. Whereas the Bessel functions describe the oscillating solutions inside the ring core with higher index of

refraction extending from $r = r_1$ to $r = r_2$, the modified Bessel functions express the exponentially growing solutions in the center of the fiber and the exponentially decreasing solutions in the outer cladding. Transverse components of the wave vector $w^{(q)}$ introduced in Eqs. (4.7) are real and they differ according to the radial region:

$$\begin{aligned} w_\eta^{(q)}(\omega) &= \sqrt{\beta_\eta^2(\omega) - \frac{\omega^2}{c^2}\varepsilon_r^{(q)}(\omega)}, \quad q = 0, 2, \\ w_\eta^{(1)}(\omega) &= \sqrt{\frac{\omega^2}{c^2}\varepsilon_r^{(1)}(\omega) - \beta_\eta^2(\omega)}. \end{aligned} \tag{4.8}$$

Relative permittivity $\varepsilon_r^{(1)}(\omega)$ characterizes the fiber ring core, permittivity $\varepsilon_r^{(0)}(\omega)$ describes the fiber inner cladding and permittivity $\varepsilon_r^{(2)}(\omega)$ is appropriate for the fiber outer cladding[7] [Fig. 4.3(c)]. All permittivities are considered to be scalar quantities. Values of real coefficients $A_\eta^{(0)}(\omega)$, $A_\eta^{(1)}(\omega)$, $B_\eta^{(1)}(\omega)$, $B_\eta^{(2)}(\omega)$, $C_\eta^{(0)}(\omega)$, $C_\eta^{(1)}(\omega)$, $D_\eta^{(1)}(\omega)$, and $D_\eta^{(2)}(\omega)$ occurring in Eqs. (4.7) are obtained from the requirement of continuity of tangential components (θ and z) of vector electric- $[\mathbf{e}_\eta(r, \theta, \omega)]$ and magnetic-field $[\mathbf{h}_\eta(r, \theta, \omega)]$ amplitudes at the boundaries of the ring core. This continuity requirement is fulfilled only for specific values of the propagation constant $\beta_\eta(\omega)$ that arise as the solution of dispersion equation [50, 51].

The θ and r components of the electric- and magnetic-field amplitudes are obtained from their z components in Eqs. (4.7) using the following formulas originating in the Maxwell equations,

$$\begin{aligned} e_{r,\eta} &= \frac{c^2}{\varepsilon_r\omega^2 - \beta_\eta^2 c^2}\left[\frac{i\omega\mu_0}{r}\frac{\partial h_{z,\eta}}{\partial\theta} + i\beta_\eta\frac{\partial e_{z,\eta}}{\partial r}\right], \\ e_{\theta,\eta} &= \frac{c^2}{\varepsilon_r\omega^2 - \beta_\eta^2 c^2}\left[-i\omega\mu_0\frac{\partial h_{z,\eta}}{\partial r} + \frac{i\beta_\eta}{r}\frac{\partial e_{z,\eta}}{\partial\theta}\right], \\ h_{r,\eta} &= \frac{c^2}{\varepsilon_r\omega^2 - \beta_\eta^2 c^2}\left[-\frac{i\omega\varepsilon_0\varepsilon_r}{r}\frac{\partial e_{z,\eta}}{\partial\theta} + i\beta_\eta\frac{\partial h_{z,\eta}}{\partial r}\right], \\ h_{\theta,\eta} &= \frac{c^2}{\varepsilon_r\omega^2 - \beta_\eta^2 c^2}\left[i\omega\varepsilon_0\varepsilon_r\frac{\partial e_{z,\eta}}{\partial r} + \frac{i\beta_\eta}{r}\frac{\partial h_{z,\eta}}{\partial\theta}\right]. \end{aligned} \tag{4.9}$$

Alternatively, the θ and r components can be replaced by the cartesian x and y com-

[7] The relative permittivities $\varepsilon_r^{(p)}; p \in \{0, 1, 2\}$ are related to linear part of the dielectric permittivity. Since the interacting fields are assumed to be weak, the non-linear contribution are assumed to have a negligible influence on the profiles of the modes.

ponents obtained by the simple relations:

$$\begin{aligned} e_{x,\eta}(r,\theta,\omega) &= \cos(\theta)e_{r,\eta}(r,\theta,\omega) - \sin(\theta)e_{\theta,\eta}(r,\theta,\omega), \\ e_{y,\eta}(r,\theta,\omega) &= \sin(\theta)e_{r,\eta}(r,\theta,\omega) + \cos(\theta)e_{\theta,\eta}(r,\theta,\omega). \end{aligned} \tag{4.10}$$

The electric- and magnetic-field amplitudes for azimuthal index $n \neq 0$ in Eq. (4.7) depends as well on phase ϕ that determines the mode polarization. An eigenmode with vertical (horizontal) polarization V (H) is obtained for $\phi = 0$ ($\phi = \pi/2$). As pairs of eigemodes with V and H polarizations have the same propagation constant β_η, eigenmodes with right- (R) and left-handed (L) circular polarizations can be built from these eigemodes using the relations:

$$\begin{aligned} e_{z,\tilde{\eta}R}(r,\theta,\omega) &= \frac{1}{\sqrt{2}}\left[e_{z,\tilde{\eta}V}(r,\theta,\omega) - ie_{z,\tilde{\eta}H}(r,\theta,\omega)\right], \\ e_{z,\tilde{\eta}L}(r,\theta,\omega) &= \frac{1}{\sqrt{2}}\left[e_{z,\tilde{\eta}V}(r,\theta,\omega) + ie_{z,\tilde{\eta}H}(r,\theta,\omega)\right], \end{aligned} \tag{4.11}$$

where $\tilde{\eta}$ indicates a mode excluding its polarization. These eigemodes are close to OAM eigemodes and in general posses non-zero OAM numbers. The electric- and magnetic-field amplitudes for $n = 0$ in Eqs. (4.7) describe two orthogonal TE_{01} and TM_{01} eigenmodes with different propagation constants $\beta_\eta(\omega)$. Polarization of TE_{01} and TM_{01} mode is obtained for $\phi = 0$ and $\phi = \pi/2$, respectively.

A common state $|\psi\rangle$ of the signal and idler fields at the output face of the fiber describing one photon pair is determined by a first-order perturbation solution of the Schrödinger equation with the interaction Hamiltonian $\hat{H}_{\mathrm{int}}$,

$$|\psi\rangle = -\frac{i}{\hbar}\int_{-\infty}^{\infty} dt\, \hat{H}_{\mathrm{int}}(t)|\mathrm{vac}\rangle. \tag{4.12}$$

State $|\mathrm{vac}\rangle$ denotes the vacuum state.

Substitution of the expressions from Eqs. (4.3–4.6) into Eq. (4.12) provides the output state $|\psi\rangle$ in the form:

$$\begin{aligned} |\psi\rangle &= \sum_{\eta_p}\sum_{\eta_s,\eta_i}\int d\omega_s \int d\omega_i\, \Phi^{\eta_p}_{\eta_s\eta_i}(\omega_s,\omega_i) \\ &\quad \times \hat{a}^\dagger_{s,\eta_s}(\omega_s)\hat{a}^\dagger_{i,\eta_i}(\omega_i)|\mathrm{vac}\rangle. \end{aligned} \tag{4.13}$$

Two-photon spectral amplitudes $\Phi^{\eta_p}_{\eta_s\eta_i}(\omega_s,\omega_i)$ introduced in Eq. (4.13) give a probability amplitude of generating a signal photon into mode η_s with frequency ω_s together with an idler photon into mode η_i with frequency ω_i from a pump photon in mode η_p. They are derived as follows:

$$\Phi^{\eta_p}_{\eta_s\eta_i}(\omega_s,\omega_i) = -\frac{i\sqrt{\omega_s\omega_i}}{\sqrt{\bar{n}_{s,\eta_s}\bar{n}_{i,\eta_i}}c} A_{p,\eta_p}\mathcal{E}_p(\omega_s+\omega_i) I^{\eta_p}_{\eta_s\eta_i}(\omega_s,\omega_i), \tag{4.14}$$

where

$$\begin{aligned} I^{\eta_p}_{\eta_s\eta_i}(\omega_s,\omega_i) &= \sqrt{2\pi}\int_{S_\perp} r dr d\theta\, \tilde{\chi}^{(2)}[-\Delta\beta^{\eta_p}_{\eta_s\eta_i}(\omega_s,\omega_i)] \\ &: \mathbf{e}_{p,\eta_p}(r,\theta,\omega_s+\omega_i)\mathbf{e}^*_{s,\eta_s}(r,\theta,\omega_s)\mathbf{e}^*_{i,\eta_i}(r,\theta,\omega_i) \end{aligned} \tag{4.15}$$

and $\Delta\beta^{\eta_p}_{\eta_s\eta_i}(\omega_s,\omega_i) = \beta_{p,\eta_p}(\omega_s+\omega_i) - \beta_{s,\eta_s}(\omega_s) - \beta_{i,\eta_i}(\omega_i)$ characterizes phase mismatch of the non-linear interaction.

Fourier transform $\tilde{\chi}^{(2)}(\beta)$ of spatially modulated $\chi^{(2)}(z)$ non-linearity used in Eq. (4.15) is given as follows:

$$\tilde{\chi}^{(2)}(\beta) = \frac{1}{\sqrt{2\pi}}\int_{-\infty}^{\infty} dz \chi^{(2)}(z)\exp(-i\beta z). \tag{4.16}$$

It attains the following form for the considered rectangular modulation composed of $2N+1$ periods of length Λ:

$$\begin{aligned} \tilde{\chi}^{(2)}(\beta) &= \chi^{(2)}\frac{2}{\sqrt{2\pi}\beta}\sin(\beta\Lambda/4)\frac{\sin[(N+1/2)\beta\Lambda]}{\sin(\beta\Lambda/2)} \\ &\quad\times\exp(i\beta\Lambda/4)\exp(iN\beta\Lambda). \end{aligned} \tag{4.17}$$

Photon-pair number density $N^{\eta_p}_{\eta_s\eta_i}(\omega_s,\omega_i)$ belonging to an individual non-linear process (η_p,η_s,η_i) is defined as

$$N^{\eta_p}_{\eta_s\eta_i}(\omega_s,\omega_i) = \langle\psi|\hat{a}^\dagger_{s,\eta_s}(\omega_s)\hat{a}^\dagger_{i,\eta_i}(\omega_i)\hat{a}_{s,\eta_s}(\omega_s)\hat{a}_{i,\eta_i}(\omega_i)|\psi\rangle. \tag{4.18}$$

Using Eq. (4.13), the density $N^{\eta_p}_{\eta_s\eta_i}$ can be expressed in a simple form:

$$N^{\eta_p}_{\eta_s\eta_i}(\omega_s,\omega_i) = |\Phi^{\eta_p}_{\eta_s\eta_i}(\omega_s,\omega_i)|^2. \tag{4.19}$$

The corresponding signal photon-number density $N^{\eta_p}_{s,\eta_s\eta_i}(\omega_s)$ is then derived according

to the formula

$$N^{\eta_p}_{s,\eta_s\eta_i}(\omega_s) = \int d\omega_i \, N^{\eta_p}_{\eta_s\eta_i}(\omega_s, \omega_i). \tag{4.20}$$

Whereas the two-photon amplitudes $\Phi(\omega_s, \omega_i)$ defined in Eq. (4.14) characterize the emitted photon pair in spectral domain, temporal two-photon amplitudes $\tilde{\Phi}(t_s, t_i)$ defined as [79]

$$\tilde{\Phi}(t_s, t_i) = \langle \mathrm{vac} | \hat{E}^{(+)}_s(0, t_s) \hat{E}^{(+)}_i(0, t_i) | \psi \rangle \tag{4.21}$$

are useful for the description of photon pairs in time domain. The substitution of Eqs. (4.6) and (4.13) into Eq. (4.21) gives us the formula valid outside the fiber:

$$\begin{aligned} \tilde{\Phi}^{\eta_p}_{\eta_s\eta_i}(t_s, t_i) &= \frac{\hbar}{4\pi\varepsilon_0 c} \int d\omega_s \int d\omega_i \, \frac{\sqrt{\omega_s \omega_i}}{\sqrt{\bar{n}_{s,\eta_s} \bar{n}_{i,\eta_i}}} \\ &\quad \times \Phi^{\eta_p}_{\eta_s\eta_i}(\omega_s, \omega_i) \exp(-i\omega_s t_s) \exp(-i\omega_i t_i). \end{aligned} \tag{4.22}$$

Photon pairs generated in an individual non-linear process (η_p, η_s, η_i) usually have a complex spectral structure that can be revealed by the Schmidt decomposition of spectral two-photon amplitude $\Phi^{\eta_p}_{\eta_s\eta_i}$,

$$\Phi^{\eta_p}_{\eta_s\eta_i}(\omega_s, \omega_i) = \sum_{k=0}^{\infty} \lambda_{\omega,k} f_{s,k}(\omega_s) f_{i,k}(\omega_s). \tag{4.23}$$

In Eq. (4.23), functions $f_{s,k}$ and $f_{i,k}$ form a Schmidt dual basis and eigenvalues $\lambda_{\omega,k}$ give coefficients of the decomposition. Provided that these coefficients are properly normalized ($\sum_{k=0}^{\infty} \lambda^2_{\omega,k} = 1$) they determine the Schmidt number K_ω of independent modes needed in the description [80],

$$K_\omega = \frac{1}{\sum_{k=0}^{\infty} \lambda^4_{\omega,k}}. \tag{4.24}$$

4.3 OAM decomposition of modes in the transverse plane

Vector modes in the transverse plane have in general a complex structure that, however, has to accord with rotational symmetry of the fiber. For this reason, it is useful to decompose their azimuthal dependencies into eigenmodes of OAM operator $\hat{L}(\theta)$, $\hat{L}(\theta) = -i\hbar\partial/(\partial\theta)$, that take the form of harmonic functions [81]:

$$t_l(\theta) = \frac{1}{\sqrt{2\pi}} \exp(il\theta). \tag{4.25}$$

Convenience of this decomposition is even emphasized when non-linear processes are taken into account as there occurs the conservation law of OAM number l [82]. This law immediately follows from the integration over azimuthal angle θ in the interaction Hamiltonian $\hat{H}_{\mathrm{int}}$ written in Eq. (4.3). For the considered SPDC process, this law is expressed as

$$l_p = l_s + l_i, \tag{4.26}$$

where the subscripts indicate the participating fields.

The electric-field modes $\mathbf{e}_\eta(r,\theta,\omega)$ involved in the interactions are vectorial, but their longitudinal components $e_{z,\eta}(r,\theta,\omega)$ are usually at least one order of magnitude smaller compared to their transverse components $e_{r,\eta}(r,\theta,\omega)$, $e_{\theta,\eta}(r,\theta,\omega)$ or $e_{x,\eta}(r,\theta,\omega)$, $e_{y,\eta}(r,\theta,\omega)$ [50, 51]. For this reason, we concentrate our attention to the analysis of transverse components. The analysis of cartesian transverse components $e_{x,\eta}(r,\theta,\omega)$ and $e_{y,\eta}(r,\theta,\omega)$ is more useful as they can easily be experimentally obtained using optical polarizers. Moreover, the x and y components of electric-field amplitude $\mathbf{e}_\eta(r,\theta,\omega)$ of the circularly polarized modes given in Eq. (4.11) are only mutually shifted in azimuthal variable θ by $\pi/2$. That is why, we further pay attention only to the x component $e_{x,\eta}(r,\theta,\omega) \equiv e_\eta(r,\theta,\omega)$.

The mode functions $e_\eta(r,\theta,\omega)$ depend in general on three variables r, θ and frequency ω. Following the rules of quantum mechanics, the probability p of detecting a photon in an OAM eigenstate t_l is given by the formula [81]:

$$p_{l,\eta}(\omega) = \int r dr \left| \int d\theta \, t_l^*(\theta) e_\eta(r,\theta,\omega) \right|^2 \tag{4.27}$$

that expresses averaging over the radial variable r.

As entangled photon pairs in their general form (for hyper-entangled photons, see [83, 84]) are emitted, two-photon amplitudes Φ depending on both transverse-plane variables and frequencies are needed in their description. They generalize the two-photon spectral amplitudes $\Phi^{\eta_p}_{\eta_s\eta_i}(\omega_s,\omega_i)$ defined in Eq. (4.14). In the usually considered spectral ranges several nm wide, the two-photon amplitude $\Phi(r_s,\theta_s,\omega_s,r_i,\theta_i,\omega_i)$ can be approximately written in the following factorized form:

$$\Phi(r_s,\theta_s,\omega_s,r_i,\theta_i,\omega_i) \approx \Phi_{r\theta}(r_s,\theta_s,r_i,\theta_i)\,\Phi_\omega(\omega_s,\omega_i). \tag{4.28}$$

The transverse part $\Phi_{r\theta}$ of two-photon amplitude can in principle be decomposed sim-

ilarly as the spectral part Φ_ω in Eq. (4.21), i.e.

$$\Phi_{r\theta}(r_s, \theta_s, r_i, \theta_i) = \sum_m \lambda_{r\theta,m}\, g_{s,m}(r_s, \theta_s) g_{i,m}(r_i, \theta_i) \tag{4.29}$$

using eigenvalues $\lambda_{r\theta,m}$ and eigenfunctions $g_{s,m}$ and $g_{i,m}$. The eigenvalues $\lambda_{r\theta,m}$ then determine the Schmidt number $K_{r\theta}$ of independent modes by the formula (4.24). However, the decomposition (4.29) is usually difficult to achieve. Nevertheless, the two-photon amplitude $\Phi_{r\theta}(r_s, \theta_s, r_i, \theta_i)$ nearly factorizes into its radial and azimuthal parts due to a simple radial dependence in our case. Then we can obtain an approximate number of modes K_θ from singular values $\lambda_{\theta,l}$ of matrix F_θ defined as

$$\mathrm{F}_{\theta,l_s l_i} = \left[\int r_s dr_s \int r_i dr_i \left| \int d\theta_s \int d\theta_i t^*_{l_s}(\theta_s) t^*_{l_i}(\theta_i) \Phi_{r\theta}(r_s, \theta_s, r_i, \theta_i) \right|^2 \right]^{1/2} \tag{4.30}$$

using Eq. (4.24).

4.4 Guided modes of a ring fiber

The generation of photon pairs around the wavelengths λ_s^0 and λ_i^0 equal to 1.55 μm is considered. The pump field is assumed to be monochromatic with a wavelength $\lambda_p^0 = 0.775$ μm. From the considerations of fields' propagation stability and efficiency of the non-linear interaction, the fiber was designed to guide radial fundamental modes for wavelengths longer than 1.2μm. This can be assured by an engineering of the inner and outer radii of the fiber.

The solution of the dispersion equation provides us the guided modes of the fiber. The dispersion equation is formulated as a determinant of a boundary-condition matrix. The boundary-condition matrix originates from the requirement of continuity of tangent components of all involved fields e_z, e_θ, h_z and h_θ at the discontinuities of dielectric permittivity function $\varepsilon(\mathbf{r}, \omega)$/[8]. The problem of boundary conditions can be solved in general for a multi-ring fiber with m discontinuities at radii $\{r_1, \ldots, r_m\}$ as follows. It holds, that the z-component of the electric and magnetic field amplitude in

[8] In the investigated ring fiber there are two discontinuities. One associated with the inner radius of the core r_1 and the other at the outer radius of the core r_2. The positions of the discontinuities are depicted in the Fig. 4.3(c).

a homogeneous region of the fiber is equal to

$$\begin{aligned} e_z^{(q)}(r,\theta,\omega) &= [C_n^{(q)}U_n^{(q)}(k_\perp^{(q)}r) + D_n^{(q)}V_n^{(q)}(k_\perp^{(q)}r)]\sin(n\theta+\phi), \\ h_z^{(q)}(r,\theta,\omega) &= [A_n^{(q)}U_n^{(q)}(k_\perp^{(q)}r) + B_n^{(q)}V_n^{(q)}(k_\perp^{(q)}r)]\cos(n\theta+\phi). \end{aligned} \tag{4.31}$$

Index q labels a region of the fiber, U_n is a Bessel function of the first order, V_n is a Bessel function of the second order and $k_\perp^{(q)} = \sqrt{(\omega/c)^2\varepsilon_r^{(q)} - \beta^2}$ is a perpendicular component of the wave vector[9]. The angular components $e_\theta(r,\theta,\omega), h_\theta(r,\theta,\omega)$ are computed from Eqs. (4.10) by usage of Eqs. (4.31).

The continuity of tangential components of electric- and magnetic-field amplitudes at boundary located at radius r_q requires validity of the following relations:

$$\begin{aligned} e_z^{(q)}(r_q,\theta,\omega) &= e_z^{(q+1)}(r_q,\theta,\omega), \\ h_z^{(q)}(r_q,\theta,\omega) &= h_z^{(q+1)}(r_q,\theta,\omega), \\ e_\theta^{(q)}(r_q,\theta,\omega) &= e_\theta^{(q+1)}(r_q,\theta,\omega), \\ h_\theta^{(q)}(r_q,\theta,\omega) &= h_\theta^{(q+1)}(r_q,\theta,\omega). \end{aligned} \tag{4.32}$$

The dependencies of amplitudes e_z, e_θ, h_z and h_θ on the angular variable θ and longitudinal variable z can be integrated out. By explicit insertion into Eqs. (4.32), a set of

[9]The perpendicular component of the wave vector $k_\perp^{(q)}$ is a real function of frequency ω in the core region and purely imaginary function of frequency ω in the cladding regions.

the following equations is obtained

$$\begin{aligned}
U_n^{(q)}C_n^{(q)} + V_n^{(q)}D_n^{(q)} - U_n^{(q+1)}C_n^{(q+1)} - V_n^{(q+1)}D_n^{(q+1)} &= 0,\\
U_n^{(q)}A_n^{(q)} + V_n^{(q)}B_n^{(q)} - U_n^{(q+1)}A_n^{(q+1)} - V_n^{(q+1)}B_n^{(q+1)} &= 0,\\
\frac{n\beta U_n^{(q)}}{(k_\perp^{(q)})^2\, r_q}C_n^{(q)} + \frac{n\beta V_n^{(q)}}{(k_\perp^{(q)})^2\, r_q}D_n^{(q)} - \frac{\omega\mu_0 w^{(q)}U_n^{(p)\prime}}{(k_\perp^{(q)})^2}A_n^{(q)}&\\
-\frac{\omega\mu_0 w^{(q)}V_n^{(q)\prime}}{(k_\perp^{(q)})^2}B_n^{(q)} - \frac{n\beta U_n^{(q+1)}}{(k_\perp^{(q+1)})^2\, r_q}C_n^{(q+1)} - \frac{n\beta V_n^{(q+1)}}{(k_\perp^{(q+1)})^2\, r_q}D_n^{(q+1)} +&\\
\frac{\omega\mu_0 w^{(q)}U_n^{(q+1)\prime}}{(k_\perp^{(q+1)})^2}A_n^{(q+1)} + \frac{\omega\mu_0 w^{(q)}V_n^{(q+1)}}{(k_\perp^{(q+1)})^2}B_n^{(q+1)} &= 0,\\
\frac{\omega\varepsilon_0\varepsilon_r^{(q)}w^{(q)}U_n^{(q)\prime}}{(k_\perp^{(q)})^2}C_n^{(q)} + \frac{\omega\varepsilon_0\varepsilon_r^{(q)}w^{(q)}V_n^{(q)\prime}}{(k_\perp^{(q)})^2}D_n^{(q)} - \frac{\beta n U_n^{(q)}}{k_\perp^{(q)}\, r_q}A_n^{(q)}&\\
\frac{\beta n V_n^{(q)}}{k_\perp^{(q)}\, r_q}B_n^{(q)} - \frac{\omega\varepsilon_0\varepsilon_r^{(q+1)}w^{(q+1)}U_n^{(q+1)\prime}}{(k_\perp^{(q+1)})^2}C_n^{(q+1)}&\\
-\frac{\omega\varepsilon_0\varepsilon_r^{(q+1)}w^{(q+1)}V_n^{(q+1)\prime}}{(k_\perp^{(q+1)})^2}D_n^{(q+1)} + \frac{\beta n U_n^{(q+1)}}{(k_\perp^{(q+1)})^2\, r_q}A_n^{(q)} + \frac{\beta n V_n^{(q+1)}}{(k_\perp^{(q+1)})^2\, r_q}B_n^{(q)} &= 0.
\end{aligned} \tag{4.33}$$

The symbols $U_n^{(q)}, V_n^{(q)}$ in Eqs. (4.33) are the corresponding Bessel functions evaluated at the discontinuity r_p [$U_n^{(q)} = U_n^{(q)}(k_\perp^{(q)} r_q, \omega), V_n^{(q)} = V_n^{(q)}(k_\perp^{(q)} r_q, \omega)$] and primes $U_n^{q\prime}, V_n^{(q)\prime}$ denote their derivatives with respect to argument $k_\perp^{(q)} r$. Equations (4.33) form set of four equations with eight unknown real-valued variables $A_n^{(q)}$, $B_n^{(q)}$, $C_n^{(q)}$, $D_n^{(q)}$, $A_n^{(q+1)}$, $B_n^{(q+1)}$, $C_n^{(q+1)}$ and $D_n^{(q+1)}$. For a discontinuity with index q, it is possible to rewrite the relations in Eq. (4.33) in a matrix form as follows:

$$\begin{pmatrix} \mathcal{A}_{11,n}^{(q)} & \mathcal{A}_{12,n}^{(q)} \\ \mathcal{A}_{21,n}^{(q)} & \mathcal{A}_{22,n}^{(q)} \end{pmatrix} \begin{pmatrix} \mathbf{U}_n^{(q)} \\ \mathbf{U}_n^{(q+1)} \end{pmatrix} = \mathbf{0}. \tag{4.34}$$

The elements of the submatrices $\mathcal{A}_{11,n}^{(q)}, \mathcal{A}_{12,n}^{(q)}, \mathcal{A}_{21,n}^{(q)}, \mathcal{A}_{22,n}^{(q)}$ are defined by the set of equations (4.33), while the vector $\mathbf{U}_n^{(q)} = \left(A_n^{(q)}, B_n^{(q)}, C_n^{(q)}, D_n^{(q)}\right)$ is formed by the unknown variables. The dimensions of the matrices $\mathcal{A}_{ij,n}^{(q)}$; $i, j = 1, 2$ are 2×4.

In the case of first and last discontinuity r_1 and r_m, the relations at the boundaries (4.34) are modified by the boundary conditions. The solution of amplitudes $e_z^{(1)}$ and $h_z^{(1)}$ are required to be finite in the region $r \in \langle 0, r_1 \rangle$. The Bessel function of the second

kind Y_n and modified Bessel function of the second kind K_n are singular at $r = 0$. Thus, the coefficients $B_n^{(1)}, D_n^{(1)}$ have to equal to zero. The requirement of vanishing of the field amplitudes $e_z^{(m)}$ and $h_z^{(m)}$ with $r \to \infty$ implies, that the amplitudes have to evolve according to the modified Bessel function of the second kind K_n/[10]. As a result, the coefficients $A_n^{(m)}, C_n^{(m)} = 0$. In total, this reduces the number of unknown variables by number of four. The boundary conditions for the first discontinuity $q = 1$ then attains a form:

$$\begin{pmatrix} \tilde{\mathcal{A}}_{11,n}^{(1)} & \mathcal{A}_{12,n}^{(1)} \\ \tilde{\mathcal{A}}_{21,n}^{(1)} & \mathcal{A}_{22,n}^{(1)} \end{pmatrix} \begin{pmatrix} \tilde{\mathbf{U}}_n^{(1)} \\ \mathbf{U}_n^{(2)} \end{pmatrix} = \mathbf{0}. \tag{4.35}$$

The matrices $\tilde{\mathcal{A}}_{11,n}^{(1)}$ and $\tilde{\mathcal{A}}_{21,n}^{(1)}$ are 2×2 matrices and the vector of unknown variables $\tilde{\mathbf{U}}_n^{(1)}$ is defined as $\tilde{\mathbf{U}}_n^{(1)} = (A_n^{(1)}, C_n^{(1)})$. The matrices $\mathcal{A}_{12,n}^{(m)}, \mathcal{A}_{22,n}^{(m)}$ have a size 2×4. In the case of the last discontinuity $q = m$, we arrive at the equation

$$\begin{pmatrix} \mathcal{A}_{11,n}^{(m)} & \tilde{\mathcal{A}}_{12,n}^{(m)} \\ \mathcal{A}_{21,n}^{(m)} & \tilde{\mathcal{A}}_{22,n}^{(m)} \end{pmatrix} \begin{pmatrix} \mathbf{U}_n^{(m)} \\ \tilde{\mathbf{U}}_n^{(m+1)} \end{pmatrix} = \mathbf{0}. \tag{4.36}$$

The vector of unknown variables $\tilde{\mathbf{U}}_n^{(n+1)}$ is defined as $\tilde{\mathbf{U}}_n^{(n+1)} = (B_n^{(n+1)}, D_n^{(n+1)})$ and the sizes of matrices $\mathcal{A}_{11,n}^{(m)}, \mathcal{A}_{21,n}^{(m)}$ and $\tilde{\mathcal{A}}_{12,n}^{(m)}, \tilde{\mathcal{A}}_{22,n}^{(m)}$ are 2×4 and 2×2, respectively.

For m discontinuities, we arrive at set of $4m$ equations for $4m$ unknown variables. This set of equations has a form $\mathcal{A}\mathbf{U} = \mathbf{0}$, which can be expressed as

$$\begin{pmatrix} \tilde{\mathcal{A}}_{11,n}^{(1)} & \mathcal{A}_{12,n}^{(1)} & 0 & 0 & \dots & 0 & 0 \\ \tilde{\mathcal{A}}_{21,n}^{(1)} & \mathcal{A}_{22,n}^{(1)} & 0 & 0 & \dots & 0 & 0 \\ 0 & \mathcal{A}_{11,n}^{(2)} & \mathcal{A}_{12,n}^{(2)} & 0 & \dots & 0 & 0 \\ 0 & \mathcal{A}_{21,n}^{(2)} & \mathcal{A}_{22,n}^{(2)} & 0 & \dots & 0 & 0 \\ \vdots & & \ddots & & \dots & & \vdots \\ 0 & \dots & & \dots & 0 & \mathcal{A}_{11,n}^{(m)} & \tilde{\mathcal{A}}_{12,n}^{(m)} \\ 0 & \dots & & \dots & 0 & \mathcal{A}_{21,n}^{(m)} & \tilde{\mathcal{A}}_{22,n}^{(m)} \end{pmatrix} \begin{pmatrix} \tilde{\mathbf{U}}_n^{(1)} \\ \mathbf{U}_n^{(2)} \\ \mathbf{U}_n^{(3)} \\ \vdots \\ \mathbf{U}_n^{(m)} \\ \tilde{\mathbf{U}}_n^{(m+1)} \end{pmatrix} = \mathbf{0}. \tag{4.37}$$

The non-zero solution of the problem requires determinant of the boundary-condition matrix $\mathcal{A}$ (4.37) to be zero. This results in the equation

$$\xi(\beta, \omega, n) = \det(\mathcal{A}) = 0, \tag{4.38}$$

where function ξ is given by determinant of the boundary-matrix $\mathcal{A}$. The variables ω, n

[10] Modified Bessel function of the second kind $K_n(r)$ is exponential-like decaying function in radial coordinate r. Therefore it satisfies the requirement $\lim_{r\to\infty} K_n(r) = 0$

in Eq. (4.38) are defined as independent variables and variable $\beta = \beta(\omega, n)$ is defined to be dependent variable. The propagation constants β are found as roots of function $\xi(\beta, \omega_0, n_0)$ for fixed values of parameters $\omega = \omega_0, n = n_0$. For this task a suitable numerical approach has to be used[11].

The fundamental mode arises as the solution of dispersion equation with the highest value of propagation constant $\beta(\omega, n)$ and occurs even at the lowest possible guided frequencies. The other modes follow the fundamental mode with lower propagation constants β. The modes are categorized with respect to their complexity in the angular and radial directions. In the angular direction, the fields are defined by the integer n (4.31). The integer n defines number of periods of the z-components of the electric- e_z and magnetic-field amplitudes h_z in the angular direction θ. In the radial direction, the modes are labelled by radial index $\tilde{n}$, which is as well an integer. It is not present explicitly in the solutions for the fields' components (4.7), but arises naturally from geometry of the problem. Geometrically, it is related to the number of periods of the mode in the radial direction.

The modes with higher radial mode numbers $\tilde{n}$ originate for higher threshold frequencies ω. This property allows us to exclude higher-order modes for the chosen frequencies (wavelengths) by a suitable choice of radii r_1 and r_2 of the fiber ring core (Fig. 4.3). Detailed numerical calculations have revealed that the analyzed fiber with its core extending from $r_1 = 4$ μm to $r_2 = 5.5$ μm admits only the radial fundamental modes for the wavelengths longer than 1.2 μm.

Effective indices of refraction $n_{\mathrm{p,eff}}$ ($n_{\mathrm{p,eff}} = c\beta_p/\omega_p$) for the pump field at the wavelength $\lambda_p^0 = 0.775$ μm are shown in Fig. 4.4. They are indexed by azimuthal number n and radial number $\tilde{n}$. Modes with the simplest transverse profiles are interesting for the non-linear interaction as they propagate with low distortions and also allow to reach the greatest values of the interaction overlap integral written in Eq. (4.15). From this point of view, TE_{01}, TM_{01}, HE_{11}, and HE_{21} modes with the greatest effective indices of refraction $n_{\mathrm{p,eff}}$ are important (see Fig. 4.4). Whereas transverse components of TE_{01} and TM_{01} modes have a complex structure from the point of view of OAM eigenmodes $t_l(\theta)$ given by Eq. (4.25), transverse components of modes $\mathrm{HE}_{11,R}$ and $\mathrm{HE}_{11,L}$ are close to eigenmode $t_0(\theta)$. Transverse components of mode $\mathrm{HE}_{21,R}$ [$\mathrm{HE}_{21,L}$] are close to eigenmode $t_{+1}(\theta)$ [$t_{-1}(\theta)$] and so bear a nonzero OAM (for details, see Fig. 4.6 below).

[11] The formulation of the dispersion Eq. (4.38) needs computation of determinant of matrix $\mathcal{A}$ in Eq. (4.37). Since the order of matrix is $4m$, the computation of the determinant can be computational demanding for higher numbers of m. For this case an alternative approach is developed [51].

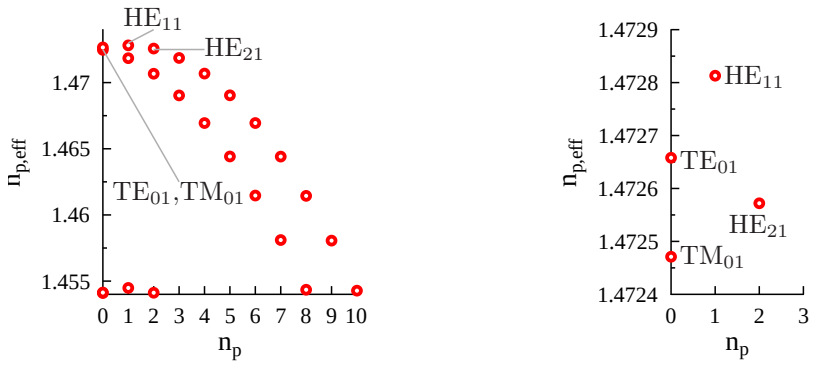

Figure 4.4: (a) Effective refractive index $n_{p,\mathrm{eff}}$ of the pump field in dependence on azimuthal number n_p for $\lambda_p^0 = 0.775$ μm. (b) Detail of the graph around $n_p = 0$ is shown.

The signal and idler fields analyzed at the wavelength $\lambda_s^0 = \lambda_i^0 = 1.55$ μm contain only radial fundamental modes which effective indices of refraction $n_{s,\mathrm{eff}}$ are plotted in Fig. (4.5). In total 14 modes occur in the analyzed spectral region: TE_{01} and TM_{01} modes without a defined OAM and both left- and right-handed circularly polarized modes HE_{11} ($l = 0$), HE_{21} ($l = \pm 1$), HE_{31} ($l = \pm 2$), HE_{41} ($l = \pm 3$), EH_{11} ($l = \pm 2$) and EH_{21} ($l = \pm 3$).

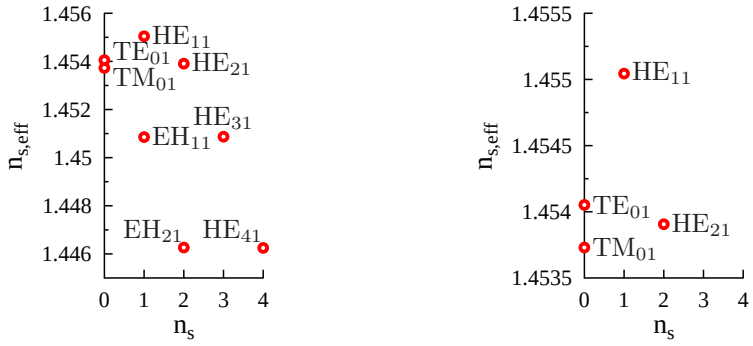

Figure 4.5: (a) Effective refractive index $n_{s,\mathrm{eff}}$ of the signal field in dependence on azimuthal number n_s for $\lambda_s^0 = 1.55$ μm. In (b), detail of the graph around $n_s = 0$ is shown.

Profiles of the x and z components of signal electric-field amplitudes $\mathbf{e}_\eta(r, \theta)$ for four simplest modes, TE_{01}, TM_{01}, HE_{11}, and HE_{21}, are shown in Fig. 4.6. The y components

of electric-field amplitudes $\mathbf{e}_\eta(r,\theta)$ have the same amplitudes as the x components of $\mathbf{e}_\eta(r,\theta)$ but their phases are shifted by $\pi/2$ with respect to the phases of the x components. The pump modes have similar profiles as the signal modes, they are only more localized inside the core ring as a consequence of their half wavelength relative to the signal one.

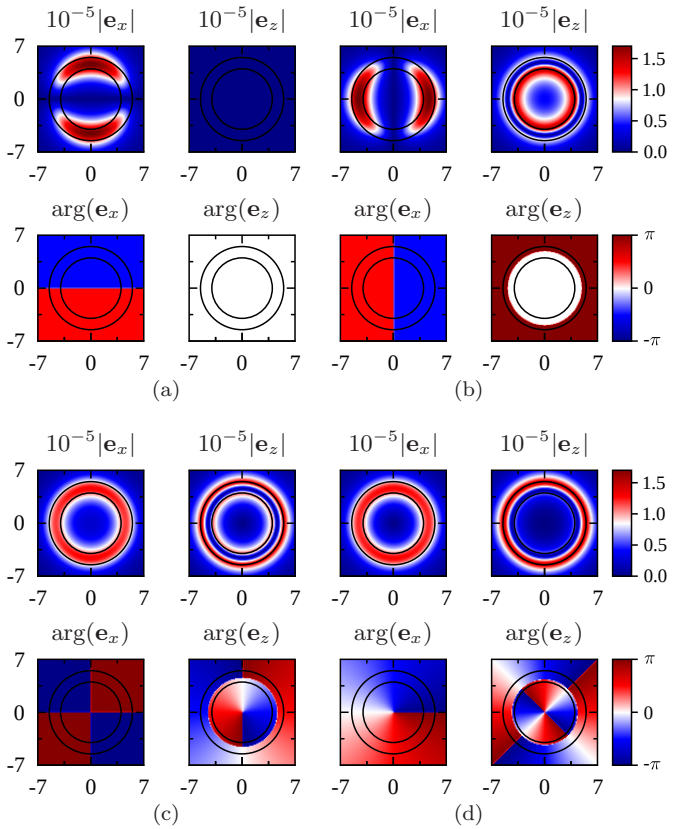

Figure 4.6: Amplitude and phase of components $e_x(x,y)$ and $e_z(x,y)$ of electric-field amplitudes for modes TE_{01} (a), TM_{01} (b), $\mathrm{HE}_{11,R}$ (c), and $\mathrm{HE}_{21,R}$ (d) for the signal field at $\lambda_s^0 = 1.55$ μm; $x = r\cos(\theta)$, $x = r\sin(\theta)$. The cartesian x and y axes' labels are in μm and the components are normalized according to $\int dxdy\,|e_{x,z}(x,y)|^2 = 1$.

The weights of individual OAM eigenmodes in the above modes determined by probabilities p in Eq. (4.27) are important for judging efficiency of the non-linear interaction as it obeys the conservation law of OAM expressed in Eq. (4.26). The probabilities p determined for the most useful modes TE_{01}, TM_{01}, HE_{11}, and HE_{21} of the signal field are depicted in Fig. 4.7. Whereas several OAM eigenmodes are essential for building TE_{01} and TM_{01} modes, the OAM eigenmode $t_0(\theta)$ [$t_{+1}(\theta)$ and $t_{-1}(\theta)$] dominates in the

x and y components of electric-field amplitude $\mathbf{e}_\eta(r,\theta)$ of modes $\mathrm{HE}_{11,R}$ and $\mathrm{HE}_{11,L}$ [$\mathrm{HE}_{21,R}$ and $\mathrm{HE}_{21,L}$]. On the other hand, the z components of electric-field amplitudes $\mathbf{e}_\eta(r,\theta)$ usually contain OAM eigenmodes t_l with l in absolute value greater by one compared to their x and y components. So the component $e_{z,\mathrm{HE}_{m1,R}}(r,\theta)$ [$e_{z,\mathrm{HE}_{m1,L}}(r,\theta)$] is formed by OAM eigenstate $t_{+m}(\theta)$ [$t_{-m}(\theta)$] for $m = 1, 2$.

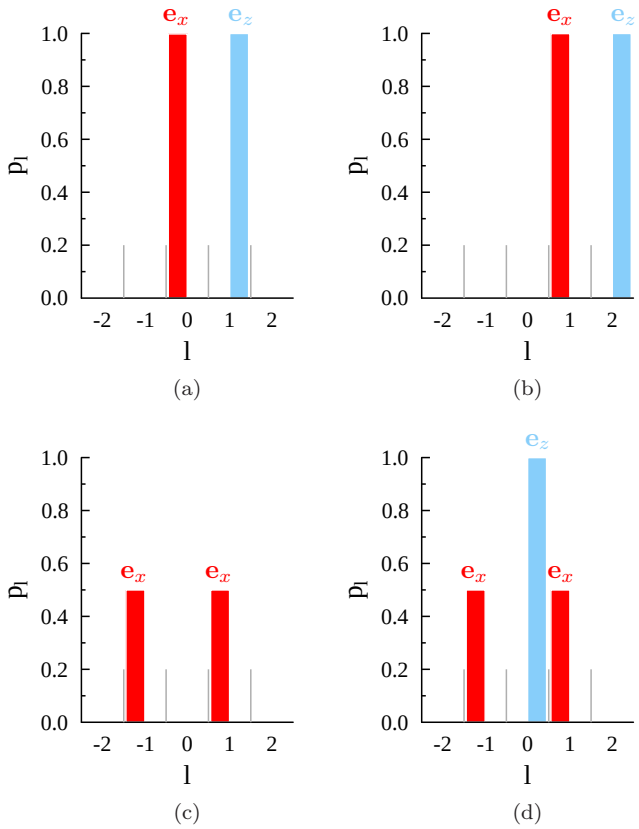

Figure 4.7: Probabilities p_l of measuring an OAM eigenmode t_l for the x and z components of electric-field amplitude $\mathbf{e}_\eta(r,\theta,\omega)$ for modes (a) TE_{01}, (b) TM_{01}, (c) $\mathrm{HE}_{11,R}$, and (d) $\mathrm{HE}_{21,R}$ for the signal field at $\lambda_s^0 = 1.55$ μm.

These modes of the pump, signal and idler fields can be combined in several different ways in order to arrive at an efficient non-linear interaction among individual modes. This interaction is efficient provided that the conservation laws of energy and OAM together with quasi-phase-matching are fulfilled. Period Λ of periodical poling is the only free parameter that allows us to choose among several individual non-linear processes. In the following three sections, different processes that give us both spectrally narrow- and broad-band photon pairs as well as photon pairs entangled in OAM numbers are

analyzed.

4.5 Generation of photon pairs with non-zero OAM numbers

Pump modes with zero OAM numbers l_p are suitable for the generation of spectrally broad-band photon pairs whereas pump modes with non-zero OAM are optimal for the emission of spectrally narrow-band photon pairs. When the conservation law of OAM in Eq. (4.26) is applied to pump modes $\mathrm{HE}_{11,R}$ and $\mathrm{HE}_{11,L}$ with $l_p = 0$, the signal l_s and idler l_i OAM numbers have to have the same absolute value, but opposite sign. The signal and idler modes then naturally have similar properties, which allow for a broad-band photon-pair generation (see the Sec. 4.6). On the other hand, if the pump beam is in mode $\mathrm{HE}_{21,R}$ with $l_p = +1$ (or its left-handed circularly polarized variant $\mathrm{HE}_{21,L}$ with $l_p = -1$) the conservation law of OAM suggests the signal and idler modes with different OAMs. The down-converted modes are then expected to have different properties and the emission of photon-pairs is assumed to be narrow-band and non-degenerate. Stability of the pump mode $\mathrm{HE}_{21,R}$ follows from the graph in Fig. 4.4 that identifies modes TE_{01} and TM_{01} as the closest modes with respect to effective refractive index $n_{p,\mathrm{eff}}$. However, differences $\Delta n_{p,\mathrm{eff}}$ between the modes ($\Delta n_{p,\mathrm{eff}} = -9 \times 10^{-5}$ for mode TE_{01}, $\Delta n_{p,\mathrm{eff}} = 1 \times 10^{-4}$ for mode TM_{01}) are high enough to guarantee stable guiding of mode HE_{21} without crosstalk.

The signal and idler modes fulfilling the conservation of OAM together with the pump $\mathrm{HE}_{21,R}$ mode are summarized in Table 4.1. However, only the variants with the signal $\mathrm{HE}_{21,R}$ mode and idler $\mathrm{HE}_{11,R}$ and $\mathrm{HE}_{11,L}$ modes are sufficiently stable. The fundamental modes $\mathrm{HE}_{11,R}$ and $\mathrm{HE}_{11,L}$ are the most stable. In detail, the difference $\Delta n_{s,\mathrm{eff}}$ of refraction indices of modes HE_{11} and the closest mode TE_{01} equals 1×10^{-3}, whereas $\Delta n_{s,\mathrm{eff}}$ for mode HE_{21} and the closest mode TE_{01} is 1.5×10^{-4}.

Also the signal TE_{01} and TM_{01} modes may participate in the non-linear interaction as they are partially composed of OAM eigenmodes with $l_s = +1$ [see Fig. 4.8(a)]. However, these modes are not suitable for transmission of photons as they do not have a well defined OAM. They can be spectrally separated from the combinations of modes discussed above owing to different propagation constants. They lead to different values of non-linear phase mismatch $\Delta\beta$ for the considered individual non-linear processes (HE_{21}^p,HE_{21}^s,HE_{11}^i), (HE_{21}^p,TE_{01}^s,HE_{11}^i) and (HE_{21}^p,TM_{01}^s,HE_{11}^i). The dependence of non-linear phase mismatch $\Delta\beta$ on signal wavelength λ_s for continuous-wave pumping

pump	$HE_{21,R}$		
l_p	+1		
signal	$HE_{21,R}$	$HE_{31,R}$ $EH_{11,R}$	$HE_{41,R}$ $EH_{21,R}$
l_s	1	2	3
idler	$HE_{11,R}$ $HE_{11,L}$	$HE_{21,L}$	$HE_{31,L}$ $EH_{11,L}$
l_s	0	-1	-2

Table 4.1: Possible combinations of pump, signal and idler modes with their OAM numbers l (in the weakly-guiding approximation [50]) fulfilling the conservation of OAM.

plotted in Fig. 4.8(a) shows that a sufficiently narrow spatial spectrum $\tilde{\chi}^{(2)}$ of QPM grating [see Eq. (4.17)] provides spectral separation of different non-linear processes. Width $\Delta\tilde{\chi}^{(2)}$ of spatial spectrum can easily be varied by the length L of the grating. The longer the grating, the narrower the spectrum $\tilde{\chi}^{(2)}$ and also the narrower the signal- and idler-field spectra. Individual non-linear processes are thus better separated for longer QPM gratings. Therefore a suitable length of the grating has to be found. A 10-cm long rectangular grating [for scheme, see Fig. 4.2] with period $\Lambda = 42.9$ μm available by a simple fabrication method [23] [see Fig. 4.8(a) for its spectrum $\tilde{\chi}^{(2)}$] satisfies the requirement. It allows the generation of signal photons around the wavelength $\lambda_s^0 = 1.5$ μm accompanied by idler photons around the wavelength $\lambda_i^0 = 1.6$ μm in the non-linear process (HE_{21}^p,HE_{21}^s,HE_{11}^i). Intensity spectral width $\Delta\tilde{\chi}^{(2)}$ equals 2×10^{-4} μm^{-1} (full width at half maximum, FWHM) for this grating and guarantees the amount of unwanted photons at the level of 1%.

The number of generated photon pairs depends on the overlap integral containing the product of pump, signal and idler electric-field amplitudes in the transverse plane [see Eq. (4.15)]. The value of this integral in the azimuthal angle is maximized due to the conservation of OAM. The maximal available value of this integral then depends on radial mode profiles that are shown in Fig. 4.8(b) for the chosen non-linear process. It holds in general that the lower the number of minima in radial intensity profiles, the greater the number of generated photon pairs. This favors modes with lower mode numbers. The utilized modes are fundamental in the radial direction. This implies that there are no zeros in their radial profiles, as can be verified in Fig. 4.8(b). As a result, they efficiency of the non-linear interaction is maximized.

Six well separated peaks occur in the down-converted field spectrum $N_s(\lambda_s)$ shown in Fig. 4.9. The most intensive peak at $\lambda_s = 1.5$ μm belongs to mode $HE_{21,R}^s$ and origi-

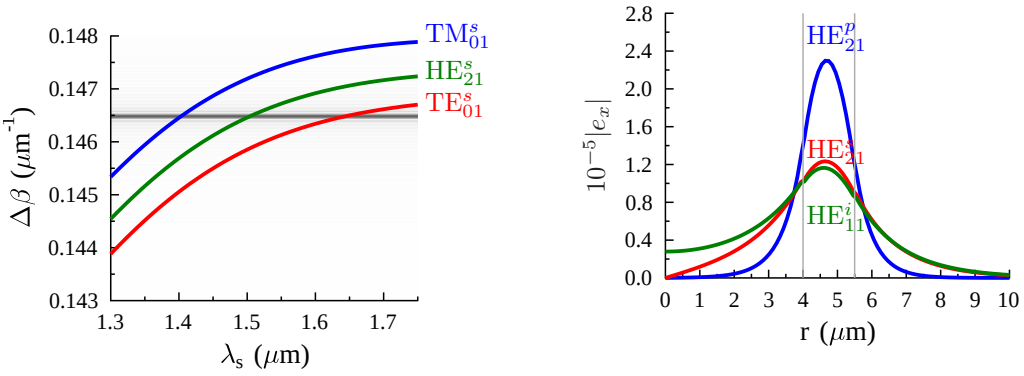

(a) (b)

Figure 4.8: (a) Phase mismatch $\Delta\beta$ for non-linear processes (HE$^p_{21}$,HE$^s_{21}$,HE$^i_{11}$), (HE$^p_{21}$,TE$^s_{01}$,HE$^i_{11}$) and (HE$^p_{21}$,TM$^s_{01}$,HE$^i_{11}$). The gray horizontal pattern describes spatial spectrum $\tilde{\chi}^{(2)}(\beta)$ of a rectangular QPM grating with $\Lambda = 42.9$ μm; $L = 10$ cm. (b) Absolute value $|e_x|$ of the x component of electric-field amplitude depending on radius r for pump mode HE$^p_{21}$, signal mode HE$^s_{21}$ and idler mode HE$^i_{11}$. Normalization is such that $\int dxdy\,|e_x(x,y)|^2 = 1$.

nates in the non-linear processes (HE$^p_{21,R}$,HE$^s_{21,R}$,HE$^i_{11,L}$) and (HE$^p_{21,R}$,HE$^s_{21,R}$,HE$^i_{11,R}$). The accompanying peaks at $\lambda_i = 1.603$ μm correspond to modes HE$^i_{11,L}$ and HE$^i_{11,R}$ with the same weight. The curves in Fig. 4.9 confirm that these desired peaks can be well separated by frequency filters from the unwanted ones. The modes HE$^i_{11,L}$ and HE$^i_{11,R}$ with the same spectra cannot be separated and in fact form a common quantum superposition state. The efficiency of spectral separation in ring fibers is similar to that found in non-linear waveguides with SPDC [85,86]. Spectral width of the peak at $\lambda_s = 1.5$ μm equals 9.41 nm (FWHM). The peak occurring at $\lambda_s = 1.4$ μm belongs to TM$_{01}$ mode and forms a pair together with the peak at $\lambda_i = 1.73$ μm given by mode HE$^i_{11,R}$. Mode TE$^s_{01}$ is responsible for the peak at $\lambda_s = 1.63$ μm that occurs together with the peak at $\lambda_i = 1.47$ μm established by mode HE$^i_{11,R}$. It is worth to note that small oscillations at the wings of the peaks reflect the shape of spatial spectrum $\tilde{\chi}^{(2)}(\beta)$ of QPM grating.

As follows from Fig. 4.9, photon-pair density N_s attains its maximum value at 2.4×10^9 nm^{-1}s^{-1} for 1 W of the pump power. Taking into account the peak spectral width, around 20 photon pairs per 1 s and 1 μW of pumping are expected in modes (HE$^p_{21,R}$,HE$^s_{21,R}$,HE$^i_{11}$) provided that appropriate spectral filters are used. The number of generated photon pairs can be increased by considering longer fibers. It can be shown theoretically that the number of photon pairs increases better than linearly with the

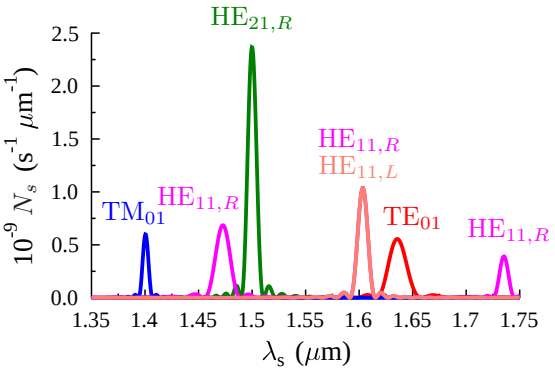

Figure 4.9: Spectral photon-number density N_s created by modes $\mathrm{HE}_{21,R}$, $\mathrm{HE}_{11,R}$, $\mathrm{HE}_{11,L}$, TE_{01}, and TM_{01} in dependence on wavelength λ_s; $N_s(\omega_s) = \sum_{\eta_p,\eta_s,\eta_i} N^{\eta_p}_{s,\eta_s,\eta_i}(\omega_s)$

fiber length. Also narrowing of the emitted spectra occurs with the increasing fiber length. On the other hand, fabrication imperfections as well as non-ideal alignment of the non-linear interaction in the laboratory reduces these numbers by one or two orders in magnitude [45].

Photon pairs are emitted in states entangled in signal and idler frequencies due to the conservation law of energy. This results in sharp temporal correlations in detection times of the signal and idler photons. For the spectra approx. 10 nm wide, typical entanglement times quantifying these correlations are in hundreds of fs (for details, see Fig. 4.11) [87].

4.6 Generation of spectrally broad-band photon pairs

As it has already been discussed above, the pump field in a $\mathrm{HE}_{11,R}$ (or $\mathrm{HE}_{11,L}$) mode with $l_p = 0$ allows to generate spectrally broad-band photon pairs achievable usually in chirped poled non-linear materials [88,89]. This is a consequence of flat spectral dependencies of phase mismatches $\Delta\beta$ of individual non-linear processes conserving OAM [see Fig. 4.10(a)]. Stable down-converted modes of LP_{11} family, HE_{21}, TE_{01} and TM_{01}, can take part in this interaction. The curves in Fig. 4.10(a) indicate that the non-linear processes ($\mathrm{HE}^p_{11,R}$,$\mathrm{HE}^s_{21,R}$,$\mathrm{HE}^i_{21,L}$), ($\mathrm{HE}^p_{11,R}$,$\mathrm{HE}^s_{21,L}$,$\mathrm{HE}^i_{21,R}$), ($\mathrm{HE}^p_{11,R}$,TE^s_{01},TM^i_{01}), and ($\mathrm{HE}^p_{11,R}$,TM^s_{01},TE^i_{01}) occur nearly simultaneously and thus may provide a more complex state. On the other hand, the processes ($\mathrm{HE}^p_{11,R}$,TE^s_{01},TE^i_{01}) and ($\mathrm{HE}^p_{11,R}$,TM^s_{01},TM^i_{01}) can easily be separated from other processes for sufficiently narrow spatial spectra

$\tilde{\chi}^{(2)}(\beta)$, similarly as in the case discussed in Section 4.5. As an example, we consider the

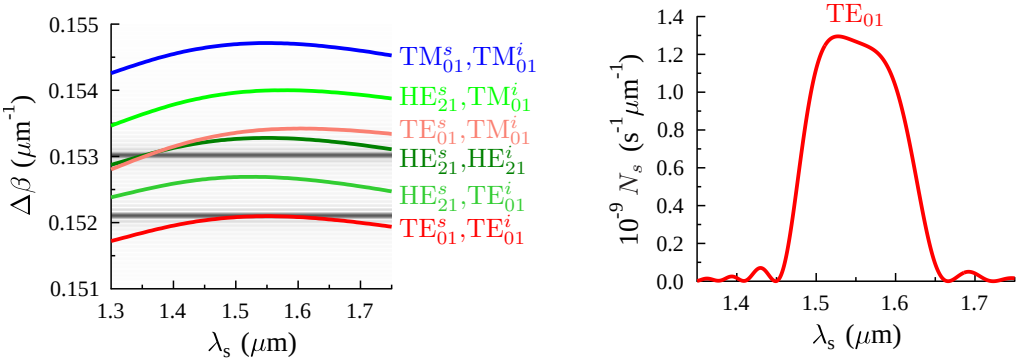

(a) (b)

Figure 4.10: (a) Phase mismatch $\Delta\beta$ for non-linear processes pumped by mode $\mathrm{HE}^p_{11,R}$ with signal and idler fields in modes HE_{21}, TE_{01} and TM_{01} in dependence on wavelength of signal photon λ_s. The gray horizontal pattern describes spatial spectra $\tilde{\chi}^{(2)}(\Delta\beta)$ of rectangular non-linear modulation with $\Lambda = 41.06$ μm (upper pattern) and $\Lambda = 42.28$ μm (lower pattern); $L = 10$ cm. (b) Spectral photon-number density N_s originating in non-linear process ($\mathrm{HE}^p_{11,R}$,TE^s_{01},TE^i_{01}); $\Lambda = 42.28$ μm, $L = 10$ cm in dependence on wavelength λ_s.

non-linear interaction with TE_{01} signal and idler modes. This interaction is achieved for period Λ of the non-linear modulation equal to 42.28 μm. Signal photon-number density $N_s(\lambda_s)$ for this process and 10-cm long QPM grating attains its maximum at degenerate wavelength $\lambda_s^0 = 1.55$ μm where a 142-nm wide peak occurs [FWHM, see Fig. 4.10(b)]. Around 150 photon pairs per 1 s and 1 μW of pumping are emitted in this process. The obtained spectrum is approx. 15 times broader compared to that of the process analyzed in Section 4.5. This implies considerably sharper temporal features of photon pairs generated by the process ($\mathrm{HE}^p_{11,R}$,TE^s_{01},TE^i_{01}). Profiles of probability densities $p_{t,i}$ of detecting an idler photon at time t_i conditioned by detection of a signal photon at time $t_s = 0$ s for both cases (narrow-band and broad-band) are compared in Fig. 4.11 confirming this fact. Whereas the probability-density width equals 4.5×10^{-14} s (FWHM) for the spectrally broad-band process ($\mathrm{HE}^p_{11,R}$,TE^s_{01},TE^i_{01}), it attains 63.5×10^{-14} s for the spectrally narrow-band process ($\mathrm{HE}^p_{21,R}$,$\mathrm{HE}^s_{21,R}$,$\mathrm{HE}^i_{11,R}$). The sharp temporal correlations are important in metrology as they determine the available temporal resolution [25, 90].

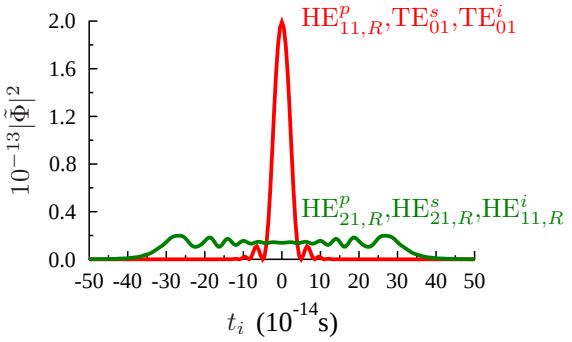

Figure 4.11: Probability density $p_{t,i}$, $p_{t,i} = \mathcal{C}|\tilde{\Phi}(0,t_i)|^2$, as a function of idler-photon detection time t_i for a signal photon detected at time $t_s = 0$ s for processes ($HE^p_{21,R}$,$HE^s_{21,R}$,$HE^i_{11,R}$) ($\Lambda = 42.9$ μm) and ($HE^p_{11,R}$,TE^s_{01},TE^i_{01}) ($\Lambda = 42.28$ μm), $L = 10$ cm. Constant $\mathcal{C}$ is defined such that $\int_{-\infty}^{\infty} dt_i p_{t,i}(t_i) = 1$.

4.7 Generation of photon pairs entangled in OAM numbers

Pumping the fiber with a $HE_{11,R}$ (or $HE_{11,L}$) mode is interesting even in the case when more LP_{11} modes participate in the non-linear interaction. Period Λ of non-linear modulation equal to 41.06 μm provides suitable conditions for four non-linear processes ($HE^p_{11,R}$,$HE^s_{21,R}$,$HE^i_{21,L}$), ($HE^p_{11,R}$,$HE^s_{21,L}$,$HE^i_{21,R}$), ($HE^p_{21,R}$,TE^s_{01},TM^i_{01}) and ($HE^p_{21,R}$,TM^s_{01},TE^i_{01}) [see Fig. 4.10(a)]. The last two processes do not contribute to photon-pair generation as they have zero overlap integrals given in Eq. (4.15). In the first two non-linear interactions, the signal and idler photons are generated with OAM numbers equal to ± 1 and ∓ 1. State $|\psi_{l_s,l_i}\rangle$ entangled in OAM numbers [91] ($|\psi_{l_s,l_i}\rangle = C_1|l_s = 1\rangle_s|l_i = -1\rangle_i + C_2|l_s = -1\rangle_s|l_i = 1\rangle_i$, C_1 and C_2 are constants) can thus be obtained at wavelengths $\lambda_s = 1.35$ μm and $\lambda_i = 1.82$ μm. As both processes have nearly equal intensities, a generated state close to the maximally entangled state is expected. Also radial profiles of the emitted photons are close to each other which justifies the use of formula (4.30) for the determination of Schmidt number K_θ. It gives $K_\theta = 1.998$. For comparison, the exact numerical decomposition described in Eq. (4.29) provides $K_\theta = 1.994$. The obtained peak in the signal photon-number density $N_s(\lambda_s)$ is 21 nm wide (FWHM) and its profile is shown in Fig. 4.12. The curve plotted in Fig. 4.12 corresponds to 30 signal photons generated per 1 s and 1 μW of pumping, which characterizes an intense source of photon pairs.

The generated state is simultaneously entangled also in the signal and idler frequen-

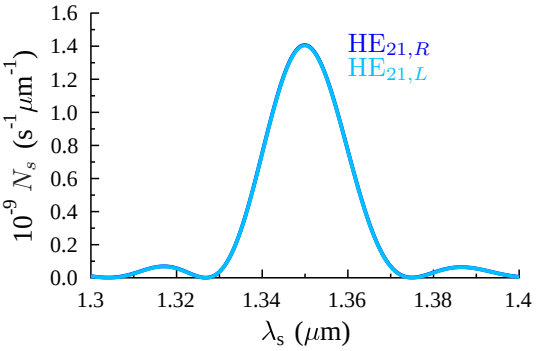

Figure 4.12: Spectral photon-number density $N_s = \sum_{\eta_p,\eta_s,\eta_i} N^{\eta_p}_{s,\eta_s\eta_i}$ arising from non-linear processes ($HE^p_{11,R}$,$HE^s_{21,R}$,$HE^i_{21,L}$) and ($HE^p_{11,R}$,$HE^s_{21,L}$,$HE^i_{21,R}$) in dependence on wavelength λ_s. The curves nearly coincide; $\Lambda = 41.06$ μm, $L = 10$ cm.

cies. It can be expressed as

$$|\psi\rangle = \int d\omega_s d\omega_i \, \Phi_{1_s,-1_i}(\omega_s,\omega_i)|l_s = 1,\omega_s\rangle_s|l_i = -1,\omega_i\rangle_i + \Phi_{-1_s,1_i}(\omega_s,\omega_i)|l_s = -1,\omega_s\rangle_s|l_i = 1,\omega_i\rangle_i. \tag{4.39}$$

We analyze spectral entanglement assuming separability of the spectral profile and that in the transverse plane for both fields. We also analyze the two-photon spectral amplitude $\Phi_{1_s,-1_i}(\omega_s,\omega_i)$ arising from the process ($HE^p_{11,R}$,$HE^s_{21,R}$,$HE^i_{21,L}$) and note that the two-photon amplitude $\Phi_{-1_s,1_i}(\omega_s,\omega_i)$ of process ($HE^p_{11,R}$,$HE^s_{21,L}$,$HE^i_{21,R}$) is very similar to the former one. As the amount of spectral entanglement depends on the pump-field spectral width σ_p, we consider the Gaussian spectrum $\mathcal{E}_p$ centered at frequency ω_p^0 corresponding to $\lambda_p^0 = 0.775$ μm,

$$\mathcal{E}_p(\omega) = \sqrt{\sqrt{\frac{2}{\pi}}\frac{1}{\sigma_p}} \exp\left[-\frac{(\omega-\omega_p^0)^2}{\sigma_p^2}\right]. \tag{4.40}$$

The two-photon spectral amplitude $\Phi_{1_s,-1_i}(\omega_s,\omega_i)$ considered for a pulsed pump field has a typical elliptical shape with axes oriented at directions $\omega_s = \omega_i - \omega_i^0 + \omega_s^0$ and $\omega_s = \omega_p^0 - \omega_i$. For the analyzed configuration, the pump-field spectrum cannot be wider than $\sigma_p = 0.85$ nm (the corresponding intensity FWHM equals 2 nm) to assure negligible contributions from other non-linear processes discussed above. In this case, the two-photon amplitude $\Phi_{1_s,-1_i}$ is elongated along the direction $\omega_s = \omega_p^0 - \omega_i$. This is caused by the fact that the extension of amplitude $\Phi_{1_s,-1_i}$ in direction $\omega_s =$

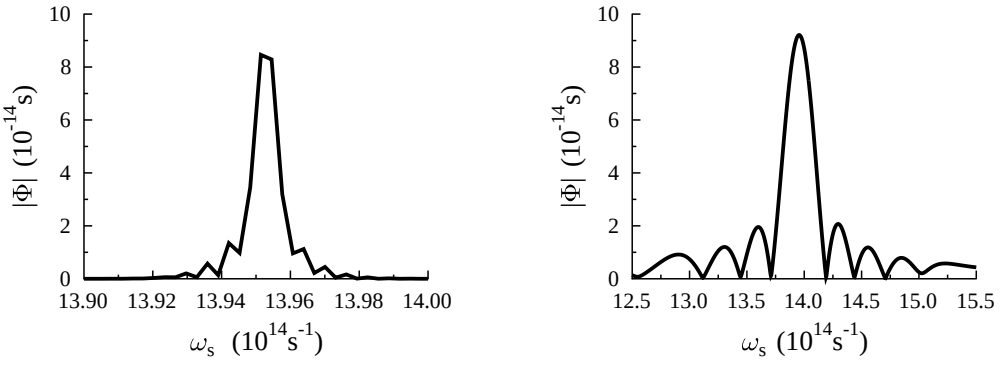

Figure 4.13: (a) Cut of absolute value $|\Phi_{1_s,-1_i}(\omega_s,\omega_i)|$ of two-photon spectral amplitude along the line $\omega_s = \omega_i - \omega_i^0 + \omega_s^0$ and (b) $\omega_s = \omega_p^0 - \omega_i$ appropriate for the process ($\mathrm{HE}^p_{11,R}$,$\mathrm{HE}^s_{21,R}$,$\mathrm{HE}^i_{21,L}$) pumped by a pulsed field; $\sigma_p = 0.85$ nm, $\Lambda = 41.06$ μm, $L = 10$ cm. It holds that $\int d\omega_s d\omega_i \, |\Phi(\omega_s,\omega_i)|^2 = 1$.

$\omega_i - \omega_i^0 + \omega_s^0$ is limited by the product of pump-field spectrum $\mathcal{E}_p$ and spatial spectrum $\tilde{\chi}^{(2)}$ of non-linear modulation. As shown in Fig. 4.13(a) for the pump field with width $\sigma_p = 0.85$ nm, spatial spectrum $\tilde{\chi}^{(2)}$ introduces oscillations in this direction. The extension of amplitude $\Phi_{1_s,-1_i}$ in direction $\omega_s = \omega_p^0 - \omega_i$ depends on phase-matching properties of the structure as well as on the width of the pump-field spectrum. This admits much broader profiles, as documented in Fig. 4.13(b). Oscillations in spectrum $\tilde{\chi}^{(2)}$ of non-linear grating are also visible in this profile, as it depends on variation from the optimal phase-matching condition.

There typically occur several tens of independent spectral modes for the considered pulsed pumping. The number K_ω of independent spectral modes determined by Eq. (4.24) increases nearly linearly with the increasing pump-field spectral width σ_p in the interval depicted in Fig. 4.14. This originates in considerable broadening of the signal- and idler-field spectra with the increasing values of spectral width σ_p. The overall number of independent modes is given by the product $K_\theta K_\omega$ of numbers of modes in the spectral and azimuthal variables and thus reaches approx. 200 for the pump field having 0.85 nm wide spectrum. All these modes can, in principle, be used for quantum communications for delivering entangled information.

We have considered 10 cm long periodically poled ring fiber as it can be fabricated by a simple method [67]. However, there exists a more sophisticated fabrication method allowing production of poled ring fibers up to 1 m long [92]. The numbers of generated

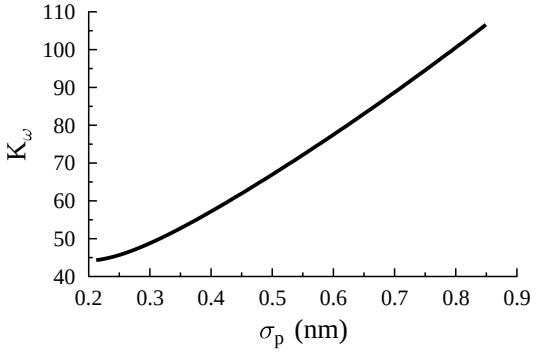

Figure 4.14: Number K_ω of independent spectral modes as it depends on pump-field spectral width σ_p; $\Lambda = 41.06$ μm, $L = 10$ cm.

photon pairs more than one order of magnitude greater are expected in such fibers.

In many applications, the signal-to-noise ratio of a photon-pair source is an important parameter. In the analyzed ring fiber, three sources of noise can be identified. The first source is related to the presence of other non-linear processes. The second source of noise is caused by the photon losses in the fiber. One photon from a generated photon pair can be lost leaving the remaining photon in the form of noise. Finally, a photon pair can be emitted into an unwanted pair of modes and so both its photons contribute to the noise. However, it has been shown in [45] that the Raman scattering as well as other non-linear processes are negligible in regular fibers with the same material structure. As for the broken photon pairs, any measurement based on the detection of photon coincidences eliminates this kind of noise. Our results have shown that the probability of generation of a photon pair into an unwanted pair of modes is lower than 1/100 for the discussed configuration. Thus, all three sources of noise can be neglected.

The discussed noise weakens entanglement of the generated state entangled in OAM numbers. This weakening can be quantified, e.g., using the Clauser-Horne-Shimony-Holt (CHSH) form of the Bell inequalities [93]. To simplify calculations, we first determine a reduced statistical operator $\hat{\rho}_{\mathrm{OAM}}$ corresponding to the state $|\psi\rangle$ in Eq. (4.39) reduced over the signal (ω_s) and idler (ω_i) frequencies. Considering additional noise with relative weight p, an appropriate statistical operator $\hat{\rho}'_{\mathrm{OAM}}$ can be expressed as

$$\hat{\rho}'_{\mathrm{OAM}} = (1-p)\hat{\rho}_{\mathrm{OAM}} + p\frac{\hat{I}}{4} \tag{4.41}$$

using the unity operator $\hat{I}$. Maximal violation of the CHSH inequalities occurs under

conditions discussed in [94]. In this case and assuming $p = 0.01$, parameter S quantifying this violation ($S > 2$) equals 2.8. The boundary value of parameter S (S = 2) is observed for $p = 0.283$, which does not represent a real limitation for experiments. For comparison, recent measurements with states entangled in OAM numbers have reached $S = 2.78$ for $l \pm 1$ [95] and $S = 2.69$ for $l \pm 2$ [96].

The results obtained is this Chapter can also be applied to fibers with vortex geometry [48]. Compared to ring fibers, they contain an additional central core. As a consequence, their fundamental mode HE_{11} is more stable. Altought, the dispersion curves of individual modes are expected to by slightly different, the non-linear process should behave in the same manner.

Chapter 5

Generation of photon pairs in layered structures

The advantages of the use of the layered structures for SPDC are mentioned in Section 5.1. It also includes the current state of art in the field of SPDC in the layered dielectric and metallo-dielectric systems. The advantages and disadvantages of the metallo-dielectric systems in comparision with the purely dielectric ones are highlighted. The non-linear tensor of the second order for metal is derived in Section 5.2. The proposed model assumes that the non-linearity is caused by the Lorentz force. The quantities characterizing a photon pair and parameters evaluating efficiency of layered structures are defined in Section 5.4. Section 5.5 includes theory of the photon losses in the investigated metallo-dielectric layered structures. The emission of photon pairs from a metal-dielectric-metal resonator is examined in Section 5.6. The design procedure is applied in order to obtain the resonator with the highest emission rate. The properties of photon pairs emitted from the designed structure are explored. Particularly, the angular-wavelength density of photon pairs. The emission efficiency is compared to both a single dielectric layer of the same length and to a reference structure. The most efficient structure with 11 layers is obtained and analyzed along the same vein in Section 5.7. In addition, mode profiles, correlated areas (both in Sec. 5.7), temporal properties (Sec. 5.8) and photon losses (Sec. 5.9) are examined.

5.1 Introduction

Modern optical structures that confine the fields in one (layered structures) or two (waveguides, optical fibers) dimensions represent qualitative improvement from the

point of view of efficiency of photon-pair generation. The confinement of interacting fields enhances their electric-field amplitudes on one side, it qualitatively changes the conditions for an efficient non-linear interaction on the other side. The requirement for phase matching of wave vectors is then replaced by the need of large spatial overlap of the electric-field amplitudes of all three interacting fields. As spatial profiles of the electric-field amplitudes depend strongly on parameters and geometry of the structures, much broader possibilities for tailoring properties of the emitted photon pairs exist.

Non-linear layered structures confine the fields along their propagation direction. Back-scattering of the fields creates a one dimensional photonic-band structure (PBG) with transmission peaks and forbidden bands [87, 97–99]. The electric-field amplitudes can be enhanced by this back-scattering, which under suitable conditions gives an efficient non-linear interaction. However, as the confinement of optical fields occurs only in one dimension, the enhancement of optical fields is considerably weaker compared to waveguiding structures, at least for dielectric structures. On the other hand, there exist the usual transverse phase-matching conditions and the impinging fields can be easily coupled into the modes of the structure [87]. Also properties of a two-photon state can be efficiently and easily controlled by spatial and temporal spectra of the pump beam. Taking into account the precision of well-established fabrication techniques [100–102], one-dimensional PBGs represent promising sources of photon pairs.

Non-linear dielectric layered structures have been already investigated from the point of view of SPDC. Both semiclassical (stochastic) [98] and quantum models [87, 99] of SPDC in dielectric layered structures have been elaborated. These structures have been shown to be able to provide entangled photon pairs anti-symmetric with respect to the exchange of signal and idler frequencies [33]. Also random non-linear dielectric layered structures have been analyzed as sources of spectrally ultra-narrow photon pairs [103, 104]. Surface SPDC has been shown to give important contribution to photon-pair generation rates [105–107].

The metallo-dielectric layered structures have been investigated from the point of view of linear transmission properties [108, 109]. It has been shown that, considering the overall transmission, the total amount of metal inside the structure can be considerably larger provided that it is split into thin layers sandwiched by dielectric layers. The enhanced transmission takes place due to resonant tunnelling effect of light[1], which relates to the entire periodical system. The strong back-scattering effects in metallo-dielectric

[1]The resonant tunnelling effect originates from three simultaneously occurring effects. Tunnelling of light through the metallic layers, negative interference of light in metallic layers and enhancement of field's amplitudes in dielectric regions. As a result the electromagnetic field is transmitted through a periodic layered structure with high efficiency.

structures, which result from high reflectivity of metallic layers, enhances the electric-field amplitudes. The amplification is considerably stronger compared to only dielectric structures [110]. This allows to consider efficient non-linear processes in more complex metallo-dielectric structures. Narrow spectral interaction regions and strong directionality of photon emissions are distinguished properties of such structures. For this reason, the emitted photon pairs are suitable for photon-atom interactions that require both properties to maximize the strength of interaction [111]. We note that such photon-atom interaction is in the center of attention in recent years in quantum-information processing as entanglement is easily generated in optical fields but excitations are easily stored in atomic systems [112–114]. Recently, the process of second harmonic generation in metallo-dielectric layered structures has been investigated both theoretically and experimentally [115, 116]. Also the first brief investigation of SPDC in such structures has confirmed high enhancement of photon-pair generation rates due to strong back-scattering occurring at metal-dielectric boundaries with high contrast of refraction indices [A3]. The detailed analysis of these structures confirmed the preliminary results and showed that the transmission properties influence as well correlated areas and temporal properties of photon pairs [A4].

5.2 Non-linear model of metal

Optical non-linear response of metals can arise due to several physical processes including the Fermi smearing [115], strong redistribution of charges [116, 117] and affecting the path of electrons by a strong magnetic field [118]. Other mechanisms leading to non-linearity are discussed in [116, 118].

The linear and non-linear properties of free electrons in metal can be described by the hydrodynamical model [116]. The hydrodynamical model of metal originates from equation of motion for free electron

$$m\frac{\mathrm{d}\mathbf{v}}{\mathrm{d}t}(\mathbf{r},t) + m\gamma\mathbf{v}(\mathbf{r},t) = -e\mathbf{E} - e\mathbf{v}(\mathbf{r},t)\times\mathbf{B} - \frac{\nabla p}{n}. \tag{5.1}$$

m is an effective mass of electron, $\mathbf{v}$ is velocity of an electron, γ is a damping factor, e is absolute value of elementary charge, p is an electron gas pressure and n is volume density of electrons. With the use of the relation between the total time derivative and the partial spatial and time derivatives

$$\frac{\mathrm{d}}{\mathrm{d}t} = \frac{\partial}{\partial t} + \mathbf{v}\cdot\nabla, \tag{5.2}$$

the relation between electric current density $\mathbf{j}$ and electron velocity $\mathbf{v}$,

$$\mathbf{j} = ne\mathbf{v}, \tag{5.3}$$

and relation between electric current density and polarization vector $\mathbf{P}$,

$$\frac{\partial \mathbf{P}}{\partial t} = \mathbf{j}, \tag{5.4}$$

the equation of motion for polarization vector $\mathbf{P}$ is obtained:

$$\frac{\partial^2 \mathbf{P}}{\partial t^2} - \frac{1}{n}\frac{\partial n}{\partial t}\frac{\partial \mathbf{P}}{\partial t} - \left(\frac{\partial \mathbf{P}}{\partial t}\cdot\nabla\right)\left(\frac{1}{ne}\frac{\partial \mathbf{P}}{\partial t}\right) + \gamma\frac{\partial \mathbf{P}}{\partial t} = \frac{ne^2}{m}\mathbf{E} - \frac{e}{m}\frac{\partial \mathbf{P}}{\partial t}\times\mathbf{B} + \frac{e}{m}\nabla p. \tag{5.5}$$

Noting Eq. (5.5) is non-linear partial differential equation of motion. In the simplest case, it is assumed that there are no significant spatial variations in the electron charge density $n \approx n_0/^2$, and that the electron gas pressure p can be neglected [118]. Than, Eq. (5.5) can be simplified

$$\frac{\partial^2 \mathbf{P}}{\partial t^2} + \gamma\frac{\partial \mathbf{P}}{\partial t} = \frac{ne^2}{m}\mathbf{E} - \frac{e}{m}\frac{\partial \mathbf{P}}{\partial t}\times\mathbf{B}. \tag{5.6}$$

Equation (5.6) is still non-linear equation of motion. The non-linearity arises from the Lorentz-force term $\partial_t\mathbf{P}\times\mathbf{B}$ [118].

Perturbation approach is applied to find the solution of Eq. (5.6). The polarization $\mathbf{P}$ is decomposed into strong linear and weak non-linear parts. Solution of Eq. (5.6) for three monochromatic waves representing the pump, signal and idler fields can then be easily found following [2]. It allows us to express the non-linear tensor $\chi^{(2)}$ as follows:

$$\begin{aligned}\chi^{(2)}_{jlm}(\mathbf{k}_p,\mathbf{k}_s,\mathbf{k}_i) \;=\; & -\frac{i\varepsilon_0}{2\pi Ne}\sum_{o,q=x,y,z} \\ & \Big[L^*(\omega_p)L^*(\omega_s)A(\omega_s,\omega_i)\varepsilon_{jlo}\varepsilon_{oqm}k^*_{i,q} + L^*(\omega_p)L^*(\omega_i)A(\omega_i,\omega_s)\varepsilon_{imo}\varepsilon_{oql}k^*_{s,q} \\ & + L(\omega_i)L^*(\omega_s)A(\omega_s,\omega_p)\varepsilon_{mlo}\varepsilon_{oqj}k_{p,q} - L(\omega_i)L(\omega_p)A(\omega_p,\omega_s)\varepsilon_{mjo}\varepsilon_{oql}k^*_{s,q} \\ & - L(\omega_s)L(\omega_p)A(\omega_p,\omega_i)\varepsilon_{ljo}\varepsilon_{oqm}k^*_{i,q} + L(\omega_s)L^*(\omega_i)A(\omega_i,\omega_p)\varepsilon_{lmo}\varepsilon_{oqj}k_{p,q}\Big].\end{aligned} \tag{5.7}$$

[2]The assumption of a small variation of the electron charge density n is valid only when the polarization of electric field amplitude $\mathbf{E}$ of a strong pump beam is parallel to the surfaces of metallic layers. Otherwise, there is non-zero spatial distribution of charges at the boundaries of the metallic and dielectric layers, which have to be taken into account. The assumption is in agreement with the performed simulations, where polarization of the electric field amplitude of the pump beam satisfy this requirement.

In Eq. (5.7), ε_{ijk} denotes the Levi-Civita tensor, $L(\omega) = \Omega_p^2/(\omega^2 + i\gamma\omega)$ and $A(\omega, \omega') = \omega/\omega'$. The expression in Eq. (5.7) for tensor $\chi^{(2)}$ reveals its strong dependence on frequencies and wave vectors of the interacting fields. Wave vectors $\mathbf{k}$ occurring in Eq. (5.7) are assumed to be complex, as the fields are strongly attenuated in metals (due to the skin effect). The expected values of elements of $\chi^{(2)}$ tensor for metals are of the order of 10^{-13} m/V.

5.3 Model of spontaneous parametric down-conversion

Vectorial model of SPDC in non-linear layered structures has been formulated in [87] using the interaction Hamiltonian $\hat{H}_{\mathrm{int}}$. Alternatively, the interaction momentum operator $\hat{G}_{\mathrm{int}}$/[3] can be used to describe SPDC caused by a strong pump beam propagating along the z axis [72, 110, 119]:

$$\hat{G}_{\mathrm{int}}(z) = 2\varepsilon_0 \int_{-\infty}^{\infty} dt \int_{\mathcal{S}} dxdy\, \chi^{(2)}(\mathbf{r}) : \left[\mathbf{E}_p^{(+)}(\mathbf{r},t)\hat{\mathbf{E}}_s^{(-)}(\mathbf{r},t)\hat{\mathbf{E}}_i^{(-)}(\mathbf{r},t) + \mathrm{h.c.}\right]; \quad (5.8)$$

$\mathbf{r} = (x, y, z)$. The pump-field is characterized by its positive-frequency electric-field vector $\mathbf{E}_p^{(+)}(\mathbf{r}, t)$. The signal and idler fields are described by their negative-frequency electric-field operator vector amplitudes $\hat{\mathbf{E}}_s^{(-)}(\mathbf{r}, t)$ and $\hat{\mathbf{E}}_s^{(-)}(\mathbf{r}, t)$, respectively. Shortening of the tensor of non-linear susceptibility $\chi^{(2)}$ with respect to its three indices is denoted by :. Symbol ε_0 stands for the vacuum permittivity; h.c. replaces the Hermitian conjugated term.

The strong un-depleted pump field is characterized by its incident temporal spectrum $\mathcal{E}_p(\omega_p)$ and spatial spectrum $\mathcal{E}_p^{\mathrm{tr}}(k_{p,x}, k_{p,y})$ defined in the transverse plane $\mathcal{S}$. The pump positive-frequency electric field vector $\mathbf{E}_p^{(+)}(\mathbf{r}, t)$ occurring in Eq. (5.8) can be decomposed in a layered structure with boundaries localized at positions z_j, $j = 0, \ldots, N$,

[3] Whereas the non-linear interaction Hamiltonian $\hat{H}_{\mathrm{int}}$ gives the interaction energy, the momentum operator $\hat{G}_{\mathrm{int}}(z)$ provides the overall flux of this energy through the transverse plane $\mathcal{S}$ positioned at distance z.

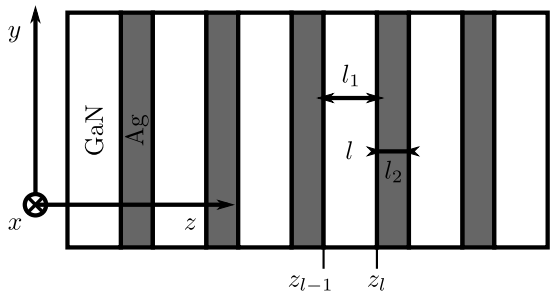

Figure 5.1: Scheme of a metallo-dielectric layered structure composed of six GaN layers and five Ag layers.

(for the scheme of the structure, see Fig. 5.1) as follows:

$$\begin{aligned}\mathbf{E}_p^{(+)}(\mathbf{r},t) &= \frac{1}{\sqrt{2\pi}^3 c^2}\int_{-\pi/2}^{\pi/2} |\sin(\vartheta_p)|\, d\vartheta_p \int_{-\pi/2}^{\pi/2} d\psi_p \int_0^{\infty} \omega_p^2 d\omega_p\, \mathcal{E}_p(\omega_p) \\ &\quad \mathcal{E}_p^{\mathrm{tr}}\left[k_{p,x}(\mathbf{\Omega_p}), k_{p,y}(\mathbf{\Omega_p})\right] \exp\left[ik_{p,x}(\mathbf{\Omega_p})x + ik_{p,y}(\mathbf{\Omega_p})y\right] \\ &\quad \sum_{\gamma=\mathrm{TE,TM}} \sum_{g=F,B} \sum_{l=0}^{N+1} \mathrm{rect}^{(l)}(z) A_{p_g,\gamma}^{(l)}(\mathbf{\Omega_p}) \mathbf{e}_{p,\gamma}^{(l)}(\mathbf{\Omega_p}) \\ &\quad \times \exp\left[ik_{p_g,z}^{(l)}(\mathbf{\Omega}_p)(z - z_{l-1})\right] \exp(-i\omega_p t) \end{aligned} \tag{5.9}$$

using the notation $\mathbf{\Omega}_p \equiv (\omega_p, \vartheta_p, \psi_p)$ for 'spherical coordinates' composed of the frequency ω_p, radial propagation angle ϑ_p and azimuthal propagation angle ψ_p. The scalar electric-field amplitudes $A_{p_F,\gamma}^{(l)}$ and $A_{p_B,\gamma}^{(l)}$ in Eq. (5.9) characterize the forward- and backward-propagating pump fields, respectively, with γ polarization in an l-th layer with index of refraction $n_p^{(l)}$. Polarization vectors $\mathbf{e}_{p_F,\gamma}^{(l)}$ and $\mathbf{e}_{p_B,\gamma}^{(l)}$ determine polarization directions of γ-polarized waves in an l-th layer propagating forward (index F) and backward (B), respectively. Function $\mathrm{rect}^{(l)}(z)$ for $l = 1, \ldots, N$ equals 1 for $z_{l-1} \leq z < z_l$ and is zero otherwise; function $\mathrm{rect}^{(0)}(z)$ [$\mathrm{rect}^{(N+1)}(z)$] is non-zero only for $z < z_0$ [$z_N \leq z$] and equals 1. Speed of light in vacuum is denoted as c. Decomposition of the pump electric field $\mathbf{E}_p^{(+)}$ into its TE- and TM-polarized waves [120] in Eq. (5.9) is done with respect to the plane of incidence of a plane wave with given wave vector $\mathbf{k}_p$.

Cartesian components of the pump-field wave vector $\mathbf{k}_p$ in spherical coordinate sys-

tem can be written in the form:

$$\begin{aligned} k_{p,x}(\mathbf{\Omega}_p) &= -\frac{\omega_p \sin(\psi_p)\sin(\vartheta_p)}{c}, \\ k_{p,y}(\mathbf{\Omega}_p) &= \frac{\omega_p \cos(\psi_p)\sin(\vartheta_p)}{c}, \\ k^{(l)}_{p_a,z}(\mathbf{\Omega}_p) &= \pm\frac{n_p^{(l)}(\omega_p)\omega_p}{c}\cos(\vartheta_p^{(l)}); l = 0,\ldots,N+1, \end{aligned} \tag{5.10}$$

where the radial propagation angle $\vartheta_p^{(l)}$ in an l-th layer obeys the Snell law:

$$n_p^{(0)}\sin(\vartheta_p^{(0)}) = n_p^{(l)}\sin(\vartheta_p^{(l)}), \quad l = 1,\ldots,N+1, \tag{5.11}$$

$\vartheta_p^{(0)} \equiv \vartheta_p$. When writing Eq. (5.10), air around the structure was assumed ($n_p^{(0)} = n_p^{(N+1)} = 1$). As the transverse components of wave vectors do not change during the propagation, the x and y components of wave vector $\mathbf{k}_p$ in Eq. (5.10) are not indexed. Also sign + (−) in Eq. (5.10) corresponds to the forward- (backward-) propagating field.

The signal and idler fields with intensities at single-photon level can be decomposed in the same way as the pump field in Eq. (5.9). However, instead of coefficients $A^{(l)}_{p_g,\gamma}$ characterizing the classical pump amplitudes, operator coefficients $\hat{A}^{(l)}_{m_a,\alpha}$ describing the quantized signal ($m = s$) and idler ($m = i$) fields are needed [72]. The formula (5.9) for the pump field can be transformed into the form applicable to the signal and idler fields:

$$\begin{aligned} \hat{\mathbf{E}}^{(+)}_m(\mathbf{r},t) &= \frac{1}{\sqrt{2\pi}^3 c^2}\int_{-\pi/2}^{\pi/2} |\sin(\vartheta_m)|\, d\vartheta_m \int_{-\pi/2}^{\pi/2} d\psi_m \\ &\int_0^\infty \omega_m^2 d\omega_m \ \exp\left[ik_{m,x}(\mathbf{\Omega}_m)x + ik_{m,y}(\mathbf{\Omega}_m)y\right] \\ &\sum_{\gamma=\mathrm{TE,TM}}\sum_{a=F,B}\sum_{l=0}^{N+1} \mathrm{rect}^{(l)}(z)\hat{A}^{(l)}_{m_a,\alpha}(\mathbf{\Omega}_m) \\ &\times \mathbf{e}^{(l)}_{m,\alpha}(\mathbf{\Omega}_m)\exp\left[ik^{(l)}_{m_a,z}(\mathbf{\Omega}_m)(z - z_{l-1})\right] \\ &\times \exp(-i\omega_m t); \quad m = s,i. \end{aligned} \tag{5.12}$$

Symbols introduced in Eq. (5.12) have the same meaning for the signal and idler fields as those defined below Eq. (5.9) for the pump field.

The pump electric-field amplitudes $A^{(l)}_{p_F,\gamma}$ and $A^{(l)}_{p_B,\gamma}$ as well as the signal and idler electric-field operator amplitudes $\hat{A}^{(l)}_{m_F,\alpha}$ and $\hat{A}^{(l)}_{m_B,\alpha}$ occurring in Eqs. (5.9) and (5.12), respectively, are mutually coupled through the Fresnel relations at the boundaries and

free-space evolution inside the layers. These relations allow to express the pump electric-field amplitudes inside the layers in terms of the amplitudes $A^{(0)}_{p_F,\gamma}$ and $A^{(N+1)}_{p_B,\gamma}$ characterizing the forward- and backward-propagating incident pump fields. On the other hand, the same relations applied to the signal and idler fields provide the signal and idler electric-field operator amplitudes inside the layers in terms of operator amplitudes $\hat{A}^{(N+1)}_{m_F,\alpha}$ and $\hat{A}^{(0)}_{m_B,\alpha}$ that correspond to the forward- and backward-propagating outgoing signal and idler fields. The transfer matrix formalism describing these relations has been developed in [87,110,120]. Using quantization of photon flux [75,76], the operator amplitudes $\hat{A}^{(N+1)}_{m_F,\alpha}$ and $\hat{A}^{(0)}_{m_B,\alpha}$ can be written using the annihilation operators $\hat{a}^{(N+1)}_{m_F,\alpha}(\mathbf{\Omega}_m)$ and $\hat{a}^{(0)}_{m_B,\alpha}(\mathbf{\Omega}_m)$:

$$\begin{aligned} \hat{A}^{(N+1)}_{m_F,\alpha}(\mathbf{\Omega}_m) &= i\sqrt{\frac{\hbar\omega_m}{2\varepsilon_0 c}}\,\hat{a}^{(N+1)}_{m_F,\alpha}(\mathbf{\Omega}_m); \\ \hat{A}^{(0)}_{m_B,\alpha}(\mathbf{\Omega}_m) &= i\sqrt{\frac{\hbar\omega_m}{2\varepsilon_0 c}}\,\hat{a}^{(0)}_{m_B,\alpha}(\mathbf{\Omega}_m), \end{aligned} \tag{5.13}$$

obeying the usual boson commutation relations:

$$[\hat{a}^{(l)}_{m_a,\alpha}(\mathbf{\Omega}_m), \hat{a}^{(l')\dagger}_{m_{a'},\alpha'}(\mathbf{\Omega}'_m)] = \frac{c^2}{|\sin(\vartheta_m)|\omega_m^2}\delta_{l,l'}\delta_{a,a'}\delta_{\alpha,\alpha'}\delta(\omega_m-\omega'_m)\delta(\theta_m-\theta'_m)\delta(\psi_m-\psi'_m). \tag{5.14}$$

Symbol $\hbar$ stands for the reduced Planck constant. More details can be found in [87,110].

An outgoing photon pair in the state $|\psi^{\text{out}}_{s,i}\rangle$ is described by the first-order perturbation solution of the Schrödinger equation written as

$$|\psi^{\text{out}}_{s,i}\rangle = \frac{i}{\hbar}\int_0^L dz\,\hat{G}_{\text{int}}(z)|\text{vac}\rangle. \tag{5.15}$$

In Eq. (5.15), L denotes the structure length and $|\text{vac}\rangle$ means the signal and idler vacuum state.

Substituting Eqs. (5.8), (5.9), (5.12), and (5.13) into Eq. (5.15) the expression for

the two-photon state $|\psi_{s,i}^{\text{out}}\rangle$ is revealed:

$$
\begin{aligned}
|\psi_{s,i}^{\text{out}}\rangle \;=\; & -\frac{2i}{\sqrt{2\pi}^3 c^7}\sum_{l=1}^{N}\sum_{a,b,g=F,B}\sum_{\alpha,\beta,\gamma=\text{TE,TM}}\left[\prod_{m=p,s,i}\int_{-\pi/2}^{\pi/2}|\sin(\vartheta_m)|d\vartheta_m\int_{-\pi/2}^{\pi/2}d\psi_m\right. \\
& \left.\times\int_0^{\infty}\omega_m^2 d\omega_m\right]\sqrt{\frac{\omega_s\omega_i}{n_s^{(l)}(\omega_s)n_i^{(l)}(\omega_i)}}\,\mathcal{E}_p(\omega_p)\mathcal{E}_p^{\text{tr}}[k_{p,x}(\mathbf{\Omega}_p),k_{p,y}(\mathbf{\Omega}_p)] \\
& \times\delta(\omega_p-\omega_s-\omega_i)\delta\left[k_{p,x}(\mathbf{\Omega}_p)-k_{s,x}(\mathbf{\Omega}_s)-k_{i,x}(\mathbf{\Omega}_i)\right] \\
& \times\delta\left[k_{p,y}(\mathbf{\Omega}_p)-k_{s,y}(\mathbf{\Omega}_s)-k_{i,y}(\mathbf{\Omega}_i)\right] \\
& \times\chi^{(2)(l)}(\mathbf{\Omega}_p,\mathbf{\Omega}_s,\mathbf{\Omega}_i):\mathbf{e}_{p_g,\gamma}^{(l)}(\mathbf{\Omega}_p)\,\mathbf{e}_{s_a,\alpha}^{(l)*}(\mathbf{\Omega}_s)\,\mathbf{e}_{i_b,\beta}^{(l)*}(\mathbf{\Omega}_i) \\
& \times L_l f\left[\frac{1}{2}\Delta k_{g,ab,z}^{(l)}(\mathbf{\Omega}_p,\mathbf{\Omega}_s,\mathbf{\Omega}_i)L_l\right]A_{p_g,\gamma}^{(l)}(\mathbf{\Omega}_p)\hat{a}_{s_a,\alpha}^{(l)\dagger}(\mathbf{\Omega}_s)\hat{a}_{i_b,\beta}^{(l)\dagger}(\mathbf{\Omega}_i)|\text{vac}\rangle; \quad (5.16)
\end{aligned}
$$

$f(x)=\exp(ix)\sin(x)/x$. Phase mismatch $\Delta k_{g,ab,z}^{(l)}(\mathbf{\Omega}_p,\mathbf{\Omega}_s,\mathbf{\Omega}_i)=k_{p_g,z}^{(l)}(\mathbf{\Omega}_p)-k_{s_a,z}^{(l)}(\mathbf{\Omega}_s)-k_{i_b,z}^{(l)}(\mathbf{\Omega}_i)$ occurs in an l-th layer of length $L_l=z_l-z_{l-1}$. There also exist photon pairs emitted at the boundaries [105,106,110] that are not described by Eq. (5.16). Contribution of this surface SPDC behaves similarly as the analyzed volume contribution given in Eq. (5.16). It increases the photon-pair generation rates. The general dependency of the second-order susceptibility tensor $\chi^{(2)}$ on the pump, signal and idler vectors $\mathbf{\Omega}_m$ is assumed. This dependency has to be taken into account, while the non-linear properties of metal are angular-frequency dependent[4]. For GaN layers, non-zero elements of the susceptibility tensor $\chi^{(2)}$ take the values [121]

$$
\begin{gathered}
\chi_{xxz}^{(2)}=\chi_{xzx}^{(2)}=\chi_{yyz}^{(2)}=\chi_{yzy}^{(2)}=\chi_{zxx}^{(2)}=\chi_{zyy}^{(2)}=10\,\text{pm/V}, \\
\chi_{zzz}^{(2)}=-20\,\text{pm/V}.
\end{gathered}
$$

The output state $|\psi_{s,i}^{\text{out}}\rangle$ in Eq. (5.16) can be further decomposed with respect to the signal and idler propagation directions and field polarizations. Each term describing the signal field at position $\mathbf{r}_s$ and the idler field at position $\mathbf{r}_i$ outside the structure reaches

[4]The second-order susceptibility tensor $\chi^{(2)}$ for metal is derived in Section 5.2

the form:

$$|\psi^{\alpha\beta}_{s_a,i_b}(\mathbf{r}_s,\mathbf{r}_i,t)\rangle = \prod_{m=s,i}\left[\frac{1}{c^2}\int_{-\pi/2}^{\pi/2}|\sin\vartheta_m|d\vartheta_m\int_{-\pi/2}^{\pi/2}d\psi_m\int_0^{\infty}\omega_m^2 d\omega_m\right] \times\phi^{\alpha\beta}_{ab}(\mathbf{\Omega}_s,\mathbf{\Omega}_i)\exp[i(\omega_s+\omega_i)t]\exp[-i(\mathbf{k}^{\rm out}_{s_a}\mathbf{r}_s+\mathbf{k}^{\rm out}_{i_b}\mathbf{r}_i)] \times\hat{a}^{\dagger}_{s_a,\alpha}(\mathbf{\Omega}_s)\hat{a}^{\dagger}_{i_b,\beta}(\mathbf{\Omega}_i)|\text{vac}\rangle, a,b=F,B;\ \alpha,\beta=\text{TE, TM}. \tag{5.17}$$

Wave vectors $\mathbf{k}^{\rm out}_{s_a}$ and $\mathbf{k}^{\rm out}_{i_b}$ are defined outside the structure. Spectral two-photon amplitude $\phi^{\alpha\beta}_{ab}(\mathbf{\Omega}_s,\mathbf{\Omega}_i)$ defined by Eq. (5.17) gives the probability amplitude of emitting an α-polarized signal photon at frequency ω_s and propagation direction (ϑ_s,ψ_s) together with its β-polarized idler twin at frequency ω_i and propagation direction (ϑ_i,ψ_i) at the outputs a and b of the structure.

5.4 Quantities characterizing photon pairs

Spatial and spectral intensity properties of photon pairs [99,110] can be derived from the joint signal-idler photon-number density $n^{\alpha\beta}_{ab}(\mathbf{\Omega}_s,\mathbf{\Omega}_i)$ related to signal [idler] photons with polarization α [β] and frequency ω_s [ω_i] propagating at angles (ϑ_s,ψ_s) [(ϑ_i,ψ_i)] in direction a [b]. Using the formula Eq. (5.17) for two-photon state $|\psi^{\alpha\beta}_{s_a,i_b}(\mathbf{r}_s,\mathbf{r}_i,t)\rangle$ the density $n^{\alpha\beta}_{ab}$ can be written as follows:

$$n^{\alpha\beta}_{ab}(\mathbf{\Omega}_s,\mathbf{\Omega}_i)=\frac{|\sin(\vartheta_s)\sin(\vartheta_i)|\omega_s^2\omega_i^2}{c^4}|\phi^{\alpha\beta}_{ab}(\mathbf{\Omega}_s,\mathbf{\Omega}_i)|^2. \tag{5.18}$$

Signal photon-number density $n^{\alpha\beta}_{s,ab}(\mathbf{\Omega}_s)$ is then derived in the form:

$$n^{\alpha\beta}_{s,ab}(\mathbf{\Omega}_s) = \int_{-\pi/2}^{\pi/2}d\vartheta_i\int_{-\pi/2}^{\pi/2}d\psi_i\int_0^{\infty}d\omega_i\, n^{\alpha\beta}_{ab}(\mathbf{\Omega}_s,\mathbf{\Omega}_i). \tag{5.19}$$

Subsequently, the signal spectral photon-number density $n^{\omega,\alpha\beta}_{s,ab}(\omega_s)$ is determined along the formula:

$$n^{\omega,\alpha\beta}_{s,ab}(\omega_s)=\int_{-\pi/2}^{\pi/2}d\vartheta_s\int_{-\pi/2}^{\pi/2}d\psi_s\, n^{\alpha\beta}_{s,ab}(\mathbf{\Omega}_s). \tag{5.20}$$

Similarly, the signal transverse photon-number density $n^{\text{tr},\alpha\beta}_{s,ab}(\vartheta_s,\psi_s)$ characterizing pho-

tons propagating in direction (ϑ_s, ψ_s) is determined as:

$$n_{s,ab}^{\mathrm{tr},\alpha\beta}(\vartheta_s, \psi_s) = \int_0^\infty d\omega_s \, n_{s,ab}^{\alpha\beta}(\mathbf{\Omega}_s). \tag{5.21}$$

Intensity correlations between the signal and idler fields in their transverse planes are described by the joint signal-idler transverse photon-number density $n_{ab}^{\mathrm{cor},\alpha\beta}(\vartheta_s, \psi_s, \vartheta_i, \psi_i)$ characterizing a photon pair with signal [idler] photon propagating along angles (ϑ_s, ψ_s) $[(\vartheta_i, \psi_i)]$ in direction a $[b]$:

$$n_{ab}^{\mathrm{cor},\alpha\beta}(\vartheta_s, \psi_s, \vartheta_i, \psi_i) \;=\; \int_0^\infty d\omega_s \int_0^\infty d\omega_i \, n_{ab}^{\alpha\beta}(\mathbf{\Omega}_s, \mathbf{\Omega}_i). \tag{5.22}$$

If a signal photon is detected at angle $(\vartheta_s^0, \psi_s^0)$, the joint signal-idler transverse photon-number density $n_{ab}^{\mathrm{cor},\alpha\beta}(\vartheta_s^0, \psi_s^0, \vartheta_i, \psi_i)$ gives the probability of detecting the accompanying idler photon at direction (ϑ_i, ψ_i). This probability determines the shape of correlated area [10].

In the time domain, two-photon states are characterized by a two-photon temporal amplitude $\mathcal{A}(\tau_s, \tau_i)$ that gives the probability amplitude of detecting a signal photon at time τ_s together with detecting the accompanying idler photon at time τ_i. Using two-photon spectral amplitude $\phi_{ab}^{\alpha\beta}$ in Eq. (5.17), the two-photon temporal amplitude $\mathcal{A}(\tau_s, \tau_i)$ can be expressed as:

$$\begin{aligned}\mathcal{A}_{ab}^{\alpha\beta}(\theta_s, \psi_s, \tau_s, \theta_i, \psi_i, \tau_i) \;=\; & \frac{\sqrt{|\sin(\vartheta_s)\sin(\vartheta_i)|}\hbar}{4\pi\varepsilon_0 c^3} \int_{-\infty}^\infty d\omega_s \\ & \int_{-\infty}^\infty d\omega_i \sqrt{\omega_s^3 \omega_i^3}\, \phi_{ab}^{\alpha\beta}(\mathbf{\Omega}_s, \mathbf{\Omega}_i) \exp(-i\omega_s\tau_s) \exp(-i\omega_i\tau_i).\end{aligned} \tag{5.23}$$

Temporal properties of photon pairs are usually experimentally investigated employing the Hong-Ou-Mandel interferometer [11]. In this interferometer, two photons are mutually delayed by τ_l and then they interfere on a beam splitter which output ports are monitored by two detectors measuring in coincidence (Fig. 3.1). A normalized coincidence-count rate R depends on time delay τ_l according to the formula:

$$R_{ab}^{\alpha\beta}(\tau_l, \vartheta_s, \psi_s, \vartheta_i, \psi_i) = 1 - \rho_{ab}^{\alpha\beta}(\tau_l, \vartheta_s, \psi_s, \vartheta_i, \psi_i), \tag{5.24}$$

where

$$\begin{aligned}
\rho_{ab}^{\alpha\beta}(\tau_l,\vartheta_s,\psi_s,\vartheta_i,\psi_i) &= \frac{|\sin(\vartheta_s)\sin(\vartheta_i)|\hbar^2}{2c^4 R_{0,ab}^{\alpha\beta}}\int_0^\infty d\omega_s\int_0^\infty d\omega_i\omega_s^3\omega_i^3 \\
&\quad \mathrm{Re}\Big\{\phi_{ab}^{\alpha\beta *}(\mathbf{\Omega}_s,\mathbf{\Omega}_i)\phi_{ab}^{\alpha\beta}(\omega_i,\vartheta_s,\psi_s,\omega_s,\vartheta_i,\psi_i)\exp[i(\omega_s-\omega_i)\tau_l]\Big\} \\
R_{0,ab}^{\alpha\beta}(\vartheta_s,\psi_s,\vartheta_i,\psi_i) &= \frac{|\sin(\vartheta_s)\sin(\vartheta_i)|\hbar^2}{2c^4}\int_0^\infty d\omega_s \\
&\quad \int_0^\infty d\omega_i\,\omega_s^3\omega_i^3|\phi_{ab}^{\alpha\beta}(\mathbf{\Omega}_s,\mathbf{\Omega}_i)|^2.
\end{aligned}$$

Enhancement of the non-linear interaction inside a layered structure originates from increased electric-field amplitudes due to back-scattering on the boundaries. This enhancement can be quantified using a reference structure defined in [87]. This reference structure uses the natural material non-linearity exploiting the greatest non-linear coefficient, but it does not take into account the back-scattering of the propagating light[5]. The reference structure generates a signal photon in direction (ϑ_s,ψ_s) together with an idler photon in direction (ϑ_i,ψ_i) exploiting phase matching in the transverse plane reached with a pump plane wave found in the spatial spectrum $\mathcal{E}_p^{\mathrm{tr}}$. The phase-matching is assumed to be maintained as well in the longitudinal direction z. The corresponding two-photon state $|\psi_{s,i}^{\mathrm{ref}}\rangle$ is expressed as:

$$\begin{aligned}
|\psi_{s,i}^{\mathrm{ref}}\rangle &= -\frac{2i}{\sqrt{2\pi}^3 c^5}\left[\prod_{m=s,i}\int_{-\pi/2}^{\pi/2}|\sin(\vartheta_m)|\,d\vartheta_m\int_{-\pi/2}^{\pi/2}d\psi_m\int_0^\infty \omega_m^2 d\omega_m\right] \\
&\quad \mathcal{E}_p(\omega_s+\omega_i)\mathcal{E}_p^{\mathrm{tr}}\left[k_{s,x}(\mathbf{\Omega}_s)+k_{i,x}(\mathbf{\Omega}_i),k_{s,y}(\mathbf{\Omega}_s)+k_{i,y}(\mathbf{\Omega}_i)\right] \\
&\quad \times\sum_{l=1}^{N}\sqrt{\frac{\omega_s\omega_i}{n_s^{(l)}(\omega_s)n_i^{(l)}(\omega_i)}}\,\max(|\chi^{(2)(l)}|)\,L_l\,\hat{a}_s^\dagger(\mathbf{\Omega}_s)\hat{a}_i^\dagger(\mathbf{\Omega}_i)|\mathrm{vac}\rangle \qquad (5.25)
\end{aligned}$$

Creation operator $\hat{a}_s^\dagger(\mathbf{\Omega}_s)$ $[\hat{a}_i^\dagger(\mathbf{\Omega}_i)]$ describes the signal [idler] photon at the output plane of the structure. Function max gives the maximal value of elements of non-linear tensor $\chi^{(2)(l)}$. Using the signal photon-number density $n_s^{\mathrm{ref}}(\mathbf{\Omega}_s)$ of the reference structure given in Eq. (5.19), the signal relative photon-number density $\eta_{s,ab}^{\alpha\beta}(\mathbf{\Omega}_s)$ at frequency ω_s and

[5]The terms in the two-photon amplitude, which correspond to electric field amplitudes of the interacting fields are discarded. The magnitudes of the original amplitudes are determined by the interference of the light scattered inside the structure. Therefore, the reference structure discards the impact of the interference effects on the non-linear interaction.

in emission direction (ϑ_s, ψ_s) is conveniently defined using the relation:

$$\eta_{s,ab}^{\alpha\beta}(\mathbf{\Omega}_s) = \frac{n_{s,ab}^{\alpha\beta}(\mathbf{\Omega}_s)}{\max_{\vartheta_s,\omega_s}\left[n_s^{\mathrm{ref}}(\mathbf{\Omega}_s)\right]}. \tag{5.26}$$

In Eq. (5.26), the maximum is taken over the whole interval of radial emission angles ϑ_s and frequencies ω_s assuming a fixed azimuthal emission angle ψ_s^0.

In the numerical calculations, a cw pump field with amplitude ξ_p and Gaussian transverse profile is considered, i.e.

$$\mathcal{E}_p(\omega_p) = \xi_p \delta(\omega_p - \omega_p^0), \tag{5.27}$$

$$\mathcal{E}_p^{\mathrm{tr}}(k_x, k_y) = \frac{r_p}{\sqrt{2\pi}} \exp\left[-\frac{r_p^2(k_x^2 + k_y^2)}{4}\right]; \tag{5.28}$$

ω_p^0 is the central frequency and r_p stands for the radius of transverse profile. It holds that $\int dk_x \int dk_y |\mathcal{E}_p^{\mathrm{tr}}(k_x, k_y)|^2 = 1$. Whenever the expression $\delta^2(\omega)$ occurs in the above defined formulas, it has to be replaced by the expression $2T/(2\pi)\delta(\omega)$ obtained for the fields defined inside interval $(-T, T)$. Physical quantities obtained per unit time interval are reached in the limit $T \to \infty$.

5.5 Losses in layered structures and noise photons

The analyzed metallo-dielectric layered structures may produce considerable amount of noise photons due to strong absorption of the metal. The reason is that an absorbed photon leaves its twin in the structure. If this twin exits the structure, it forms the noise that is superimposed on the emitted photon-pair field. In this section, a theory that quantifies the contribution of noise photons is developed. We assume for simplicity that photon pairs are generated only in dielectric layers, in accord with our results that have revealed only weak generation of photon pairs in metal layers.

Detailed inspection of Eq. (5.16) for two-photon state $|\psi_{s,i}^{\mathrm{out}}\rangle$ reveals that this state is composed of contributions describing photon pairs emitted in different layers. We assume that similar decomposition can be done also for the joint signal-idler photon-number density $n_{ab}^{\alpha\beta}(\mathbf{\Omega}_s, \mathbf{\Omega}_i)$ defined in Eq. (5.18):

$$n_{ab}^{\alpha\beta}(\mathbf{\Omega}_s, \mathbf{\Omega}_i) \approx \sum_{l\in\mathrm{diel}} \sum_{a',b'=F,B} T_{s,aa'}^{(l)\alpha}(\mathbf{\Omega}_s) T_{i,bb'}^{(l)\beta}(\mathbf{\Omega}_i) n_{a'b'}^{(l)\alpha\beta}(\mathbf{\Omega}_s, \mathbf{\Omega}_i). \tag{5.29}$$

In Eq. (5.29), symbol $n_{a'b'}^{(l)\alpha\beta}(\mathbf{\Omega}_s, \mathbf{\Omega}_i)$ stands for the joint signal-idler photon-number density of photon pairs emitted in an l-th layer. Symbol $\sum_{l\in\text{diel}}$ means summation over dielectric layers. The photon-number density $n_{a'b'}^{(l)\alpha\beta}(\mathbf{\Omega}_s, \mathbf{\Omega}_i)$ is determined along Eq. (5.18) using a two-photon spectral amplitude $\phi_{a'b'}^{(l)\alpha\beta}(\mathbf{\Omega}_s, \mathbf{\Omega}_i)$ appropriate for the l-th layer. The intensity transmission coefficients $T_{m,aa'}^{(l)\alpha}$ introduced in Eq. (5.29) give the probability that an α-polarized photon, which was created in field m in l-th layer with direction a', leaves the structure in direction a.

Whereas $T_{m,Fa'}^{(l)\alpha} + T_{m,Ba'}^{(l)\alpha} = 1$ holds for dielectric structures, intensity absorption coefficients $D_{m,a'}^{(l)\alpha}$ are needed in metallo-dielectric structures to generalize this relation:

$$\begin{aligned} &T_{m,Fa'}^{(l)\alpha} + T_{m,Ba'}^{(l)\alpha} + D_{m,a'}^{(l)\alpha} = 1; \\ &\qquad m = s,i; \quad \alpha = \text{TE,TM}; \quad a' = F,B. \end{aligned} \tag{5.30}$$

The intensity absorption coefficient $D_{m,a'}^{(l)\alpha}$ determines the probability that an α-polarized photon propagating in direction a' in a l-th layer in field m is absorbed inside the structure. Using absorption coefficients $D_{m,a'}^{(l)\alpha}$, the signal noise photon-number density $d_{si,a}^{\alpha}(\mathbf{\Omega}_s, \mathbf{\Omega}_i)$ quantifying the amount of single α-polarized photons at frequency ω_s propagating at angle (ϑ_s, ψ_s) in direction a and originating in pairs with an idler photon with frequency ω_i at angle (ϑ_i, ψ_i) is expressed as follows:

$$d_{si,a}^{\alpha}(\mathbf{\Omega}_s, \mathbf{\Omega}_i) = \sum_{l\in\text{diel}} \sum_{\beta=\text{TE,TM}} \sum_{a',b'=F,B} T_{s,aa'}^{(l)\alpha}(\mathbf{\Omega}_s) D_{i,b'}^{(l)\beta}(\mathbf{\Omega}_i) n_{a'b'}^{(l)\alpha\beta}(\mathbf{\Omega}_s, \mathbf{\Omega}_i). \tag{5.31}$$

An overall signal noise photon-number density $d_{s,a}^{\alpha}(\mathbf{\Omega}_s)$ is then simply determined by integrating over all possible idler-field frequencies ω_i and propagation angles (ϑ_i, ψ_i):

$$d_{s,a}^{\alpha}(\mathbf{\Omega}_s) = \int_0^{\infty} d\omega_i \int_{-\pi/2}^{\pi/2} d\vartheta_i \int_{-\pi/2}^{\pi/2} d\psi_i \, d_{si,a}^{\alpha}(\mathbf{\Omega}_s, \mathbf{\Omega}_i). \tag{5.32}$$

Formulas analogous to those written in Eqs. (5.31) and (5.32) can be derived also for the idler-field noise contribution.

To judge contributions of noise single photons to the generated state with α-polarized signal photons in direction a and β-polarized idler photons in direction b, we define ratios $R_{m,ab}^{\alpha\beta}(\mathbf{\Omega}_m)$ of noise photon-number densities $d_{s,a}^{\alpha}(\mathbf{\Omega}_s)$ and $d_{i,b}^{\beta}(\mathbf{\Omega}_i)$ with respect

to densities $n^{\alpha\beta}_{m,ab}(\mathbf{\Omega}_m)$ belonging to photon pairs and written in Eq. (5.19):

$$R^{\alpha\beta}_{s,ab}(\mathbf{\Omega}_s) = \frac{d^{\alpha}_{s,a}(\mathbf{\Omega}_s)}{n^{\alpha\beta}_{s,ab}(\mathbf{\Omega}_s)}, \qquad R^{\alpha\beta}_{i,ab}(\mathbf{\Omega}_i) = \frac{d^{\beta}_{i,b}(\mathbf{\Omega}_i)}{n^{\alpha\beta}_{i,ab}(\mathbf{\Omega}_i)}. \tag{5.33}$$

Also photon pairs with polarizations and propagation directions different from the analyzed one and denoted by indices (a,α) and (b,β) in Eq. (5.33) contribute to noise photons provided that one of their two photons is captured by detectors. In this case, ratios $\tilde{R}^{\alpha\beta}_{m,ab}(\mathbf{\Omega}_m)$ defined along the relations

$$\begin{aligned}
\tilde{R}^{\alpha\beta}_{s,ab}(\mathbf{\Omega}_s) &= \frac{d^{\alpha}_{s,a}(\mathbf{\Omega}_s) + \sum_{\beta'=\mathrm{TE}}^{\mathrm{TM}} \sum_{b'=F}^{B} n^{\alpha\beta'}_{s,ab'}(\mathbf{\Omega}_s)}{n^{\alpha\beta}_{s,ab}(\mathbf{\Omega}_s)} - 1, \\
\tilde{R}^{\alpha\beta}_{i,ab}(\mathbf{\Omega}_i) &= \frac{d^{\beta}_{i,b}(\mathbf{\Omega}_i) + \sum_{\alpha'=\mathrm{TE}}^{\mathrm{TM}} \sum_{a'=F}^{B} n^{\alpha'\beta}_{i,a'b}(\mathbf{\Omega}_i)}{n^{\alpha\beta}_{i,ab}(\mathbf{\Omega}_i)} - 1
\end{aligned} \tag{5.34}$$

appropriately characterize the noise of the emitted state. However, this part of noise can be removed in principle when multiple coincidence-count measurements are applied in the experiment.

To determine ratios $R^{\alpha\beta}_{m,ab}(\mathbf{\Omega}_m)$ and $\tilde{R}^{\alpha\beta}_{m,ab}(\mathbf{\Omega}_m)$ characterizing noise in the emitted state, we need intensity transmission $T^{(l)\alpha}_{m,aa'}$ and absorption coefficients $D^{(l)\alpha}_{m,a'}$ for the signal and idler photons born in each dielectric layer. In what follows, we concentrate our attention to photons of field m ($m = s,i$) created in an l-th layer (for the scheme of a general structure, see Fig. 5.2). To describe properly damping in metal layers, we have to introduce time into the description, at least implicitly. We reach this by defining the appropriate boundary conditions and by placing the initial amplitude of the photon at particular position in the structure. There are two distinct cases characterizing the photons propagating forward and backward in the l-th layer.

First, backward-propagating α-polarized photons described by amplitude $A^{(l),\mathrm{ext}}_{m_B,\alpha}(\mathbf{\Omega}_m)$ are added to the l-th layer and their evolution inside the structure is followed. This evolution is described by the transfer-matrix formalism elaborated for the non-linear layered structures in [87, 110]. The remaining boundary conditions are such that photons do not enter the structure from its front ($A^{(0)}_{m_F,\alpha}(\mathbf{\Omega}_m) = 0$) and rear ($A^{(N+1)}_{m_B,\alpha}(\mathbf{\Omega}_m) = 0$) ends. The backward-propagating photons added into the l-th layer propagate first in the layers to the left from the l-th layer, they can penetrate into the layers to the right from the l-th layer later and they can even return back to the left-

hand-side layers from the right-hand-side ones. This consideration takes into an account all possible paths of the photon inside the structure. Following the scheme plotted in Fig. 5.2 and showing the used amplitudes, two sets of linear equations characterizing the propagation through the left- and right-hand-side layers can be written separately:

$$\begin{pmatrix} A^{(l)}_{m_F,\alpha}(\mathbf{\Omega}_m) \\ A^{(l),\mathrm{ext}}_{m_B,\alpha}(\mathbf{\Omega}_m) + [\mathcal{P}^{(l)}_m(\mathbf{\Omega}_m)]^*_{22} B^{(l)}_{m_B,\alpha}(\mathbf{\Omega}_m) \end{pmatrix} = \mathcal{L}^{(l)}_{m,\alpha}(\mathbf{\Omega}_m) \begin{pmatrix} 0 \\ A^{(0)}_{m_B,\alpha}(\mathbf{\Omega}_m) \end{pmatrix},$$

$$\begin{pmatrix} A^{(N+1)}_{m_F,\alpha}(\mathbf{\Omega}_m) \\ 0 \end{pmatrix} = \mathcal{R}^{(l)}_{m,\alpha}(\mathbf{\Omega}_m) \begin{pmatrix} [\mathcal{P}^{(l)}_m(\mathbf{\Omega}_m)]_{11} A^{(l)}_{m_F,\alpha}(\mathbf{\Omega}_m) \\ B^{(l)}_{m_B,\alpha}(\mathbf{\Omega}_m) \end{pmatrix}. \tag{5.35}$$

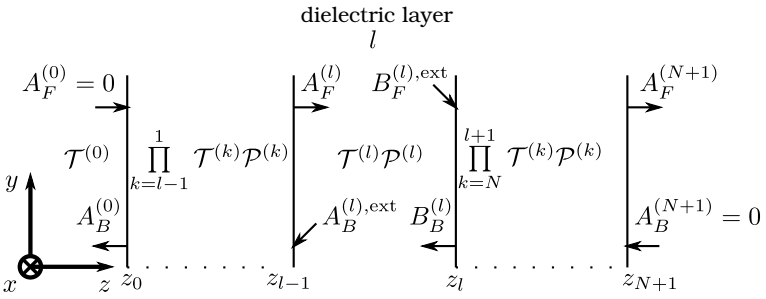

Figure 5.2: Scheme of a structure composed of N layers. Whereas amplitudes $A^{(l)}$ describe the fields at the left-hand side of an l-th layer ($l = 1, \ldots, N+1$), amplitudes $B^{(l)}$ are appropriate for the right-hand side of this layer ($l = 1, \ldots, N$); amplitudes $A^{(0)}$ give the fields in front of the structure. Amplitudes $A_B^{(l),\mathrm{ext}}$ and $B_F^{(l),\mathrm{ext}}$ belong to the fields added into an l-th layer. Subscript F (B) identifies the forward- (backward-) propagating fields. Matrices $\mathcal{T}^{(l)}$ characterize an l-th boundary and matrices $\mathcal{P}^{(l)}$ determine the free-field evolution in an l-th layer.

Matrices $\mathcal{L}^{(l)}_{m,\alpha}(\mathbf{\Omega}_m)$ [$\mathcal{R}^{(l)}_{m,\alpha}(\mathbf{\Omega}_m)$] introduced in Eq. (5.35) describe the propagation of both forward- and backward-propagating fields in the layers positioned to the left [right] from the l-th layer. They can be expressed in terms of matrices $\mathcal{T}^{(j)}_{m,\alpha}(\mathbf{\Omega}_m)$ and $\mathcal{P}^{(j)}_m(\mathbf{\Omega}_m)$ characterizing propagation through a j-th boundary and free-field propagation in a j-th

layer, respectively:

$$\begin{aligned}\mathcal{L}^{(l)}_{m,\alpha}(\mathbf{\Omega}_m) &= \prod_{j=l}^{2}\left[\mathcal{T}^{(j-1)}_{m,\alpha}(\mathbf{\Omega}_m)\mathcal{P}^{(j-1)}_{m}(\mathbf{\Omega}_m)\right]\mathcal{T}^{(0)}_{m,\alpha}(\mathbf{\Omega}_m),\\ \mathcal{R}^{(l)}_{m,\alpha}(\mathbf{\Omega}_m) &= \prod_{j=N}^{l+1}\left[\mathcal{T}^{(j)}_{m,\alpha}(\mathbf{\Omega}_m)\mathcal{P}^{(j)}_{m}(\mathbf{\Omega}_m)\right]\mathcal{T}^{(l)}_{m,\alpha}(\mathbf{\Omega}_m).\end{aligned} \tag{5.36}$$

More details including definitions of the elements of matrices $\mathcal{T}^{(j)}_{m,\alpha}(\mathbf{\Omega}_m)$ and $\mathcal{P}^{(j)}_{m}(\mathbf{\Omega}_m)$ can be found in [87, 110].

Two sets of equations written in (5.35) are coupled. These equations can easily be rearranged such that one linear set of equations for amplitudes $A^{(N+1)}_{m_F,\alpha}(\mathbf{\Omega}_m)$, $B^{(l)}_{m_B,\alpha}(\mathbf{\Omega}_m)$, $A^{(l)}_{m_F,\alpha}(\mathbf{\Omega}_m)$, and $A^{(0)}_{m_B,\alpha}(\mathbf{\Omega}_m)$ is obtained [Eq. (5.37)]. The fields propagating out of the l-the layer are characterized by amplitudes $B^{(l)}_{m_B,\alpha}(\mathbf{\Omega}_m)$, $A^{(l)}_{m_F,\alpha}(\mathbf{\Omega}_m)$, while the fields leaving the whole structure at its front and rear end correspond to amplitudes $A^{(0)}_{m_B,\alpha}(\mathbf{\Omega}_m)$ and $A^{(N+1)}_{m_F,\alpha}(\mathbf{\Omega}_m)$, respectively.

$$\begin{pmatrix}0\\1\\0\\0\end{pmatrix}A^{(l),\mathrm{ext}}_{m_B,\alpha}(\mathbf{\Omega}_m) = \mathcal{M}^{(l)}_{m,\alpha}(\mathbf{\Omega}_m)\begin{pmatrix}A^{(N+1)}_{m_F,\alpha}(\mathbf{\Omega}_m)\\B^{(l)}_{m_B,\alpha}(\mathbf{\Omega}_m)\\A^{(l)}_{m_F,\alpha}(\mathbf{\Omega}_m)\\A^{(0)}_{m_B,\alpha}(\mathbf{\Omega}_m)\end{pmatrix}, \tag{5.37}$$

$$\mathcal{M}^{(l)}_{m,\alpha}(\mathbf{\Omega}_m) = \begin{pmatrix}0 & 0 & -1 & [\mathcal{L}^{(l)}_{m,\alpha}]_{12}\\ 0 & -[\mathcal{P}^{(l)}_{m}]^{*}_{22} & 0 & [\mathcal{L}^{(l)}_{m,\alpha}]_{22}\\ -1 & [\mathcal{R}^{(l)}_{m,\alpha}]_{12} & [\mathcal{R}^{(l)}_{m,\alpha}]_{11}[\mathcal{P}^{(l)}_{m}]_{11} & 0\\ 0 & -[\mathcal{R}^{(l)}_{m,\alpha}]_{22} & -[\mathcal{R}^{(l)}_{m,\alpha}]_{21}[\mathcal{P}^{(l)}_{m}]_{11} & 0\end{pmatrix}. \tag{5.38}$$

The solution of set of Eqs. (5.37) provides the amplitudes that determine photon fluxes both inside the l-th layer and outside the whole layered structure. The obtained amplitudes provide us the needed intensity transmission and absorption coefficients as follows.

According to the Poynting theorem, time-averaged power $P^{(l)}_{m_B,\alpha}(\mathbf{\Omega}_m)$ generated in

the l-th layer by the added field $A^{(l),\mathrm{ext}}_{m_B,\alpha}$ is expressed as follows:

$$\begin{aligned} P^{(l)}_{m_B,\alpha}(\mathbf{\Omega}_m) &= n^{(l)}_m(\omega_m)\cos(\vartheta^{(l)}_m)\Big[|A^{(l),\mathrm{ext}}_{m_B,\alpha}(\mathbf{\Omega}_m) + [\mathcal{P}^{(l)}_m(\mathbf{\Omega}_m)]^*_{22}B^{(l)}_{m_B,\alpha}(\mathbf{\Omega}_m)|^2 \\ &\quad +|[\mathcal{P}^{(l)}_m(\mathbf{\Omega}_m)]_{11}A^{(l)}_{m_F,\alpha}(\mathbf{\Omega}_m)|^2 - |A^{(l)}_{m_F,\alpha}(\mathbf{\Omega}_m)|^2 - |B^{(l)}_{m_B,\alpha}(\mathbf{\Omega}_m)|^2\Big]. \end{aligned} \tag{5.39}$$

This power is partly dissipated both in the left- and right-hand-side layers and its remaining part leaves the structure either at its front or rear end. Power $P^{(l)F}_{m_B,\alpha}(\mathbf{\Omega}_m)$ $[P^{(l)B}_{m_B,\alpha}(\mathbf{\Omega}_m)]$ beyond the rear end [in front] of the structure is determined as follows

$$\begin{aligned} P^{(l)F}_{m_B,\alpha}(\mathbf{\Omega}_m) &= \cos(\vartheta^{(N+1)}_m)|A^{(N+1)}_{m_F,\alpha}(\mathbf{\Omega}_m)|^2, \\ P^{(l)B}_{m_B,\alpha}(\mathbf{\Omega}_m) &= \cos(\vartheta^{(0)}_m)|A^{(0)}_{m_B,\alpha}(\mathbf{\Omega}_m)|^2. \end{aligned} \tag{5.40}$$

Power $P^{(l)D}_{m_B,\alpha}(\mathbf{\Omega}_m)$ dissipated in the left- and right-hand-side layers can then be derived from the conservation law of energy:

$$P^{(l)D}_{m_B,\alpha}(\mathbf{\Omega}_m) = P^{(l)}_{m_B,\alpha}(\mathbf{\Omega}_m) - P^{(l)F}_{m_B,\alpha}(\mathbf{\Omega}_m) - P^{(l)B}_{m_B,\alpha}(\mathbf{\Omega}_m). \tag{5.41}$$

If power $P^{(l)}_{m_B,\alpha}(\mathbf{\Omega}_m)$ equals to that of one photon per second, the powers $P^{(l)F}_{m_B,\alpha}(\mathbf{\Omega}_m)$, $P^{(l)B}_{m_B,\alpha}(\mathbf{\Omega}_m)$ and $P^{(l)D}_{m_B,\alpha}(\mathbf{\Omega}_m)$ give in turn intensity transmission coefficients $T^{(l)\alpha}_{m,FB}(\mathbf{\Omega}_m)$ and $T^{(l)\alpha}_{m,BB}(\mathbf{\Omega}_m)$ and intensity absorption coefficient $D^{(l)\alpha}_{m,B}(\mathbf{\Omega}_m)$:

$$\begin{aligned} T^{(l)\alpha}_{m,aB}(\mathbf{\Omega}_m) &= \frac{P^{(l)a}_{m_B,\alpha}(\mathbf{\Omega}_m)}{P^{(l)}_{m_B,\alpha}(\mathbf{\Omega}_m)}, \quad a = F, B, \\ D^{(l)\alpha}_{m,B}(\mathbf{\Omega}_m) &= \frac{P^{(l)D}_{m_B,\alpha}(\mathbf{\Omega}_m)}{P^{(l)}_{m_B,\alpha}(\mathbf{\Omega}_m)}. \end{aligned} \tag{5.42}$$

In the second case, forward-propagating α-polarized photons described by amplitude $B^{(l),\mathrm{ext}}_{m_F,\alpha}(\mathbf{\Omega}_m)$ is added into the l-th layer. These photons propagate first in the right-hand-side layers, they enter into the left-hand-side layers later and they can propagate back to the right-hand-side layers again. Also in this case, no photon enters the structure from its front $[A^{(0)}_{m_F,\alpha}(\mathbf{\Omega}_m) = 0]$ and rear $[A^{(N+1)}_{m_B,\alpha}(\mathbf{\Omega}_m) = 0]$ ends. Similarly as for the added backward-propagating photons, we can write two sets of linear equations

characterizing the propagation through the left- and right-hand-side layers separately:

$$\begin{pmatrix} A^{(l)}_{m_F,\alpha}(\mathbf{\Omega}_m) \\ [\mathcal{P}^{(l)}_m(\mathbf{\Omega}_m)]^*_{22} B^{(l)}_{m_B,\alpha}(\mathbf{\Omega}_m) \end{pmatrix} = \mathcal{L}^{(l)}_{m,\alpha}(\mathbf{\Omega}_m) \begin{pmatrix} 0 \\ A^{(0)}_{m_B,\alpha}(\mathbf{\Omega}_m) \end{pmatrix},$$
$$\begin{pmatrix} A^{(N+1)}_{m_F,\alpha}(\mathbf{\Omega}_m) \\ 0 \end{pmatrix} = \mathcal{R}^{(l)}_{m,\alpha}(\mathbf{\Omega}_m) \begin{pmatrix} B^{(l),\mathrm{ext}}_{m_F,\alpha}(\mathbf{\Omega}_m) + [\mathcal{P}^{(l)}_m(\mathbf{\Omega}_m)]_{11} A^{(l)}_{m_F,\alpha}(\mathbf{\Omega}_m) \\ B^{(l)}_{m_B,\alpha}(\mathbf{\Omega}_m) \end{pmatrix}. \tag{5.43}$$

Matrices $\mathcal{L}^{(l)}_{m,\alpha}(\mathbf{\Omega}_m)$ and $\mathcal{R}^{(l)}_{m,\alpha}(\mathbf{\Omega}_m)$ are defined in Eqs. (5.36). Eqs. (5.43) can be transformed into a linear set of equations for amplitudes $A^{(N+1)}_{m_F,\alpha}(\mathbf{\Omega}_m)$, $B^{(l)}_{m_B,\alpha}(\mathbf{\Omega}_m)$, $A^{(l)}_{m_F,\alpha}(\mathbf{\Omega}_m)$, and $A^{(0)}_{m_B,\alpha}(\mathbf{\Omega}_m)$ of fields:

$$\begin{pmatrix} 0 \\ 0 \\ -[\mathcal{R}^{(l)}_{m,\alpha}(\mathbf{\Omega}_m)]_{11} \\ [\mathcal{R}^{(l)}_{m,\alpha}(\mathbf{\Omega}_m)]_{21} \end{pmatrix} B^{(l),\mathrm{ext}}_{m,\alpha}(\mathbf{\Omega}_m) = \mathcal{M}^{(l)}_{m,\alpha}(\mathbf{\Omega}_m) \begin{pmatrix} A^{(N+1)}_{m_F,\alpha}(\mathbf{\Omega}_m) \\ B^{(l)}_{m_B,\alpha}(\mathbf{\Omega}_m) \\ A^{(l)}_{m_F,\alpha}(\mathbf{\Omega}_m) \\ A^{(0)}_{m_B,\alpha}(\mathbf{\Omega}_m) \end{pmatrix}; \tag{5.44}$$

matrix $\mathcal{M}^{(l)}_{m,\alpha}(\mathbf{\Omega}_m)$ is defined in Eq. (5.38). The solution of system of Eqs. (5.44) allows us to determine photon fluxes that give the powers discussed above. For the forward-propagating photons added into the l-th layer, power $P^{(l)}_{m_F,\alpha}(\mathbf{\Omega}_m)$ given into this layer by the external field with amplitude $B^{(l),\mathrm{ext}}_{m_F,\alpha}$ is derived in the form:

$$\begin{aligned} P^{(l)}_{m_F,\alpha}(\mathbf{\Omega}_m) &= n^{(l)}_m(\omega_m)\cos(\vartheta^{(l)}_m)\Big[|B^{(l),\mathrm{ext}}_{m_F,\alpha}(\mathbf{\Omega}_m) + [\mathcal{P}^{(l)}_m(\mathbf{\Omega}_m)]_{11} A^{(l)}_{m_F,\alpha}(\mathbf{\Omega}_m)|^2 \\ &\quad + |[\mathcal{P}^{(l)}_m(\mathbf{\Omega}_m)]^*_{22} B^{(l)}_{m_B,\alpha}(\mathbf{\Omega}_m)|^2 - |B^{(l)}_{m_B,\alpha}(\mathbf{\Omega}_m)|^2 - |A^{(l)}_{m_F,\alpha}(\mathbf{\Omega}_m)|^2\Big]. \end{aligned} \tag{5.45}$$

This power can be divided into three parts. Its first part $[P^{(l)F}_{m_F,\alpha}(\mathbf{\Omega}_m)]$ is delivered beyond the rear end of the structure, whereas its second part $[P^{(l)B}_{m_F,\alpha}(\mathbf{\Omega}_m)]$ is transferred into the space in front of the structure. Finally, the third part $[P^{(l)D}_{m_F,\alpha}(\mathbf{\Omega}_m)]$ dissipates inside the metal layers. These powers then serve for the determination of intensity transmission coefficients $T^{(l)\alpha}_{m,FF}(\mathbf{\Omega}_m)$ and $T^{(l)\alpha}_{m,BF}(\mathbf{\Omega}_m)$ and intensity absorption coefficient $D^{(l)\alpha}_{m,F}(\mathbf{\Omega}_m)$. Whereas formulas analogous to those written in Eqs. (5.39) and (5.40) give powers $P^{(l)F}_{m_F,\alpha}(\mathbf{\Omega}_m)$, $P^{(l)B}_{m_F,\alpha}(\mathbf{\Omega}_m)$ and $P^{(l)D}_{m_F,\alpha}(\mathbf{\Omega}_m)$, expressions derived from those in Eqs. (5.41) provide coefficients $T^{(l)\alpha}_{m,FF}(\mathbf{\Omega}_m)$, $T^{(l)\alpha}_{m,BF}(\mathbf{\Omega}_m)$ and $D^{(l)\alpha}_{m,F}(\mathbf{\Omega}_m)$.

5.6 A simple metallo-dielectric resonator

Though both the metal and dielectric layers are non-linear, the dielectric layers are able to provide much higher photon-pair fluxes[6]. For this reason, the presence of thin metal layers is important for an enhancement of electric-field amplitudes inside the structure. This enhancement then results in much stronger non-linear interaction and efficient production of photon pairs. Compared to pure dielectric layered structures like those composed of GaN and AlN, analyzed in [87,110], metallo-dielectric layered structures allow for much higher enhancement of electric-field amplitudes due to the high refraction-index contrast of the used metal and dielectric materials. For comparison and considering the wavelength 800 nm, this indices of refraction are equal to 2.51 [2.16] for GaN [AlN] layers and 5.3 [2.51] for Ag [GaN] layers analyzed here. However, strong attenuation, reflection and losses of the electric-field amplitudes occur in metal layers. This puts restrictions to the possible thicknesses of metal layers as well as to the number of metal layers embedded into the structure.

To get deeper insight into the behavior of metallo-dielectric layered structures, we first consider the simplest possible structure composed of only one non-linear GaN layer sandwiched by two thin Ag layers. Thus, the Ag layers form mirrors of a simple resonator that enhances the electric-field amplitudes inside the GaN layer. To achieve efficient non-linear interaction, we apply the method for designing an efficient layered structure for SPDC suggested in [87]. Lengths l_2 of GaN layers and l_1 of Ag layer vary in the method to reveal the most efficient structure. In the method, only pairs (l_1, l_2) of lengths that provide transmission maxima for the pump field at a chosen wavelength λ_p^0 are analyzed. Concentrating on the highest transmission maximum that also gives the greatest enhancement of the pump field, the appropriate pairs (l_1, l_2) of lengths form a one-dimensional parametric system. This means that for any value of GaN-layer length l_2 there exists only one value of Ag-layers length l_1.

In the analysis, we consider a plane-wave TE-polarized[7] pump-field at central wavelength $\lambda_p^0 = 400$ nm impinging on the structure at normal incidence. The simulated power transmission of the pump beam is shown in the Fig. 5.3. Structures with thick Ag layers ($l_1 > 10$ nm) provide frequency-degenerated photon pairs. On the other hand, structures with thin Ag layers emit frequency non-degenerated photon pairs. The greatest value of relative signal photon-number density η defined in Eq. (5.26) is reached for slightly frequency non-degenerated photon-pair emission for $l_1 = 9.6376$ nm

[6] Non-linear suscetibility tensor $\chi^{(2)}$ of GaN has at least two orders of magnitude larger terms in comparison with Ag.

[7] The TE polarized electric field amplitude of the pump beam is oriented along the axis x.

and $l_2 = 95.1195$ nm. It is important to note that the signal and idler photons can leave the structure either along the $+z$ or $-z$ axes, so four possible combinations for photon pairs exist. Nevertheless different photon pairs have comparable properties. That is why, we pay attention to only photon pairs with both photons propagating along the $+z$ direction. The structure generates photon pairs around the radial emission angle $\vartheta = 83$ deg. Two emission maxima are observed in relative signal photon-number density η_s [see Fig. 5.4(a)][8]. Whereas one maximum contains TE-polarized photons, the other maximum is composed of TM-polarized photons. As elements $\chi^{(2)}_{xxz}$ and $\chi^{(2)}_{xzx}$ of susceptibility tensor participate in the non-linear interaction, a TE-polarized photon is accompanied by a TM-polarized photon and vice versa. Two maxima in relative signal photon-number density η_s, shown in Fig. 5.4(a), are sharp compared to similar dielectric structures. This is a consequence of strong interference of back-scattered optical fields caused by the high refractive-index contrast. These sharp features are characteristic for both spectral and spatial properties of photon pairs.

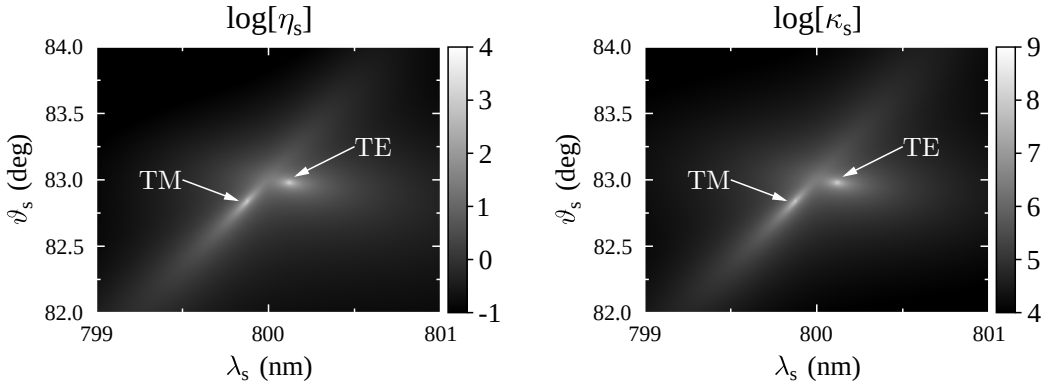

(a) (b)

Figure 5.4: (a) The relative signal photon-number density η_s in dependence on signal radial emission angle ϑ_s and wavelength λ_s for a simple 'metallo-dielectric' resonator structure composed of one GaN layer and two Ag layers. Both photons with arbitrary polarizations propagate along the $+z$ axis; $\lambda_p^0 = 400$ nm, $l_1 = 95.1195$ nm, $l_2 = 9.6376$ nm, $\psi_s^0 = 0$ deg; log denotes the decimal logarithm. (b) The ratio κ of signal photon-number densities n_s of the simple 'metallo-dielectric' resonator structure and GaN monolayer of equal thickness as it depends on signal radial emission angle ϑ_s and wavelength λ_s.

The advantage of 'metal resonator' surrounding the non-linear GaN layer can be quantified comparing its signal photon-number density n_s [Eq. (5.19)] with that char-

[8]The quantity η_s was plotted for azimuthal angle $\psi_s^0 = 0$ deg.

acterizing one GaN monolayer structure of the same length ($l = 114.3947$ nm). Ratio κ of these photon-number densities n_s [see Fig. 5.4(b)] shows that the enhancement of up to nine orders in magnitude is reached in areas of maximal emission intensities, i.e. under conditions of the strongest constructive interference of the signal [idler] field. The enhancement factor rapidly drops down when wavelengths λ_s and radial emission angles ϑ_s move away from these optimal conditions.

5.7 An efficient metallo-dielectric structure

In order to sufficiently enhance the non-linear interaction, more complex metallo-dielectric layered structures have to be considered. There exists an interval of suitable numbers of the used layers. On one side, larger number of layers leads to strong interference and also to high enhancement of electric-field amplitudes. On the other side, larger number of metal layers results in strong attenuation of the electric fields. To keep balance between these effects, we have decided to design a structure with five metal Ag layers sandwiched by six GaN layers (for the scheme, see Fig. 5.1).

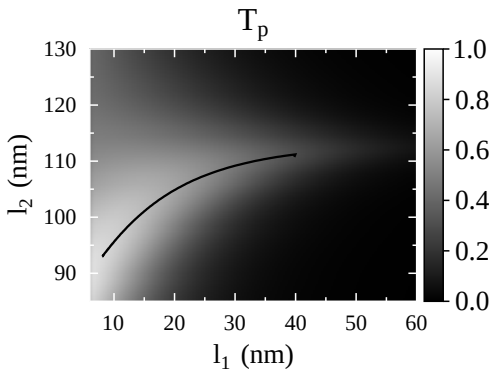

Figure 5.3: Power transmission coefficient T_p in dependence on the length of the metallic layers l_1 and dielectric layer l_2.

Following the design procedure, we have plotted the pump-field intensity transmission coefficient T_p at the wavelength $\lambda_p^0 = 400$ nm and for TE polarization [see Fig. 5.5(a)] as it depends on lengths of the dielectric layers l_1 and metallic layers l_2. The pump field impinging on the structure at normal incidence has been assumed. In this graph, five transmission bands can be seen. It follows from the theory of band-gap structures that the greatest enhancement of electric-field amplitudes occurs in the transmission band closest to the band gap. In this band, also the greatest values of absorption A_p are found [see Fig. 5.5(b)] indicating large electric-field amplitudes inside the metal layers [118].

Structures corresponding to the maxima of the first transmission band have been parameterized by the ratio $L = l_2/l_1$. Maximum $\eta_s^{\max}$ of relative signal photon-number density η_s taken over frequency ω_s and radial emission angle ϑ_s assuming fixed azimuthal angle $\psi_{s,0} = 0$ deg was chosen for quantification of efficiency of the non-linear process.

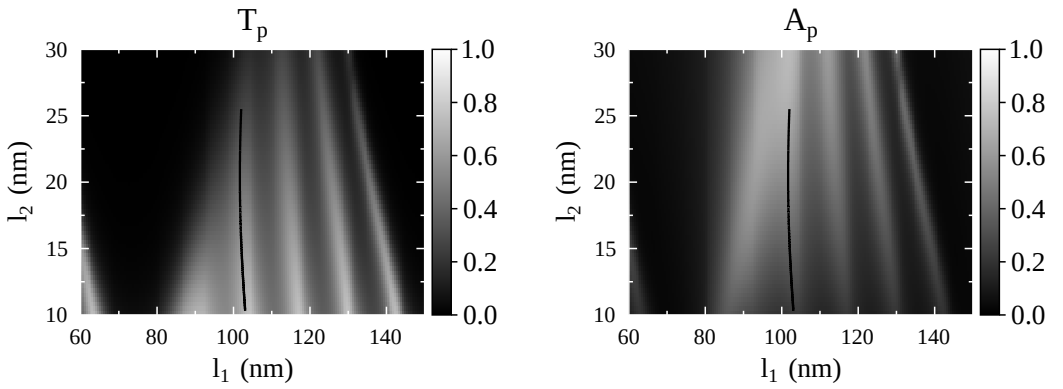

(a) (b)

Figure 5.5: (a) Intensity transmission coefficient T_p. (b) Intensity absorption coefficient A_p. Both quantities T_p and A_p depend on lengths of the layers l_1 - dielectric, and l_2 - metallic. The obtained results are valid for TE-polarized field at $\lambda_p^0 = 400$ nm impinging on the structure under normal incidence . Positions of maxima in the first transmission band are indicated by solid black curves.

Structures with parameter L in the interval $(0.1, 0.25)$ were only considered because very thin metal layers do not sufficiently enhance the electric-field amplitudes. Moreover, their transmission bands are broader. On the other hand, thick metal layers attenuate the propagating electric fields. Maximal values $\eta_s^{\max}$ of relative signal photon-number density η_s were found in two regions: $L \in (0.17, 0.18)$ and $L \in (0.225, 0.24)$. In these regions, $\eta_s^{\max}$ reaches values around 10^6. The first region of L, analyzed in Fig. 5.6, is more suitable and contains the most efficient structure ($L = 0.178$) with lengths $l_1 = 101.752$ nm and $l_2 = 18.083$ nm. The obtained values of maxima $\eta_s^{\max}$ are higher by two orders in magnitude compared to the values of maxima $\eta_s^{\max}$ of the 'metal resonator' investigated in Section 5.6. Additionally, these values are even higher by seven orders in magnitude compared to those of pure dielectric layered structures studied in [87]. Detailed analysis of SPDC inside the metallo-dielectric structures shows that dielectric layers are the major source of photon pairs. Metal layers give photon-pair numbers lower by six orders in magnitude compared to the dielectric layers. Nevertheless, they play a critical role in the enhancement of electric-field amplitudes inside the structure due to their high indices of refraction. We have also analyzed SPDC involving a TM-polarized pump field along the same vein. However, the obtained values of maxima $\eta_s^{\max}$ have been found considerably lower than those discussed above for the TE-polarized pump field.

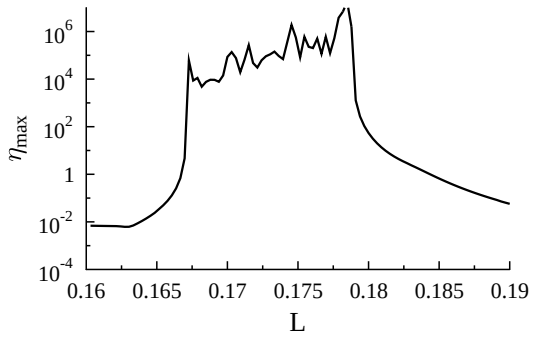

Figure 5.6: Maximum $\eta_s^{\max}$ of relative signal photon-number density η_s depending on ratio L of layers' lengths, $L = l_2/l_1$, for structures composed of 11 layers such that the pump field at $\lambda_p^0 = 400$ nm occurs in the center of the first transmission band (see Fig. 5.5).

Relative signal photon-number density η_s of this structure (plotted in Fig. 5.7) reveals two emission peaks. One peak is centered at the wavelength $\lambda_s = 737.837$ nm and the radial emission angle $\vartheta_s = 47.686$ deg, the other peak occurs at the wavelength $\lambda_s = 873.601$ nm and the radial emission angle $\vartheta_s = 61.095$ deg. The signal photon at wavelength $\lambda_s = 737.837$ nm is TE polarized and its twin has TM polarization. On the other hand, the signal photon at wavelength $\lambda_s = 873.601$ nm has TM polarization, whereas its twin is TE polarized. This means that the first photon pair exploits the element $\chi^{(2)}_{xxz}$ of susceptibility tensor whereas the second photon pair uses the element $\chi^{(2)}_{xzx}$. The emission peaks are very narrow in both the wavelength λ_s and radial emission angle θ_s. The intensity peaks' widths $\Delta\lambda_s$ are narrower than 1×10^{-3} nm (full width at half maximum, FWHM). In radial emission angle, the intensity peaks' widths $\Delta\vartheta_s$ are narrower than 5×10^{-2} deg. It is worth to stress that the sharpness of these peaks arises from the behavior of TM-polarized fields. The analyzed system has nearly radial symmetry which is only weakly broken by the varying values of $\chi^{(2)}$ elements in azimuthal direction. So the emitted photon pairs form two narrow concentric rings; slightly changing intensities are found around these rings.

The electric-field amplitude profiles of the interacting fields along the propagating z axis for $(p, s, i) = (\mathrm{TE}, \mathrm{TE}, \mathrm{TM})$ interaction are shown in Fig. 5.8. The pump electric-field amplitude profile is determined for the incident electric-field amplitude 1 V/m impinging on the structure at $z = 0$ m. The signal and idler electric-field amplitude profiles are such that they give the outgoing amplitude 1 V/m at the end of the structure and 0 V/m for the outgoing amplitude at $z = 0$ m. The TE-polarized pump and signal

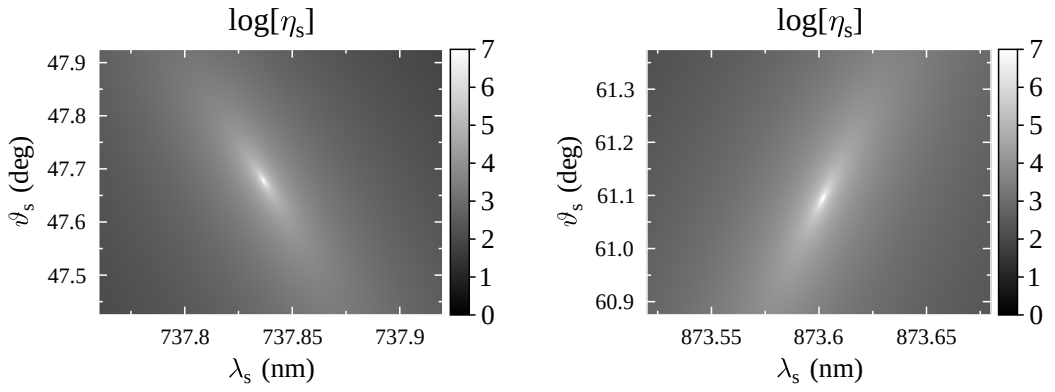

(a) (b)

Figure 5.7: Relative signal photon-number density η_s in dependence on signal wavelength λ_s and radial emission angle ϑ_s for two regions containing (a) TE-polarized and (b) TM-polarized photons; $\lambda_p^0 = 400$ nm, $l_1 = 101.752$ nm, $l_2 = 18.083$ nm.

fields have their electric-field amplitudes inside the structure enhanced several times. In contrast, the enhancement factor of TM-polarized idler field equals around 10^5 due to highly constructive interference of the back-scattered fields at the boundaries. For comparison, the enhancement factor for GaN/AlN layered structures typically equals several tens [87].

Also correlated areas characterizing spatial correlations between the signal and idler intensities are narrow. Two different shapes of correlated areas found in the analyzed structure are shown in Fig. 5.9 for a pump beam with Gaussian transverse profile of radius $r_p = 1$ mm. If we fix the emission direction of the TM-polarized idler photon at $\vartheta_i = -61.095$ deg, the correlated area of TE-polarized signal photon has roughly a Gaussian shape which originates in the Gaussian pump-field transverse shape [see Fig. 5.9(a)]. On the other hand, when the TE-polarized signal photon is detected at $\vartheta_s = 47.686$ deg, the correlated area of TM-polarized idler photon is highly elliptic [see Fig. 5.9(b)]. The reason is that its extension along the azimuthal angle ψ_i is determined by the pump-beam radius r_p, whereas its extension along the radial angle ϑ_i is strongly limited by the properties of TM modes related to their strong back-scattering on the boundaries. The dependence on pump-beam radius r_p can be used to tailor the extensions of correlated areas [10].

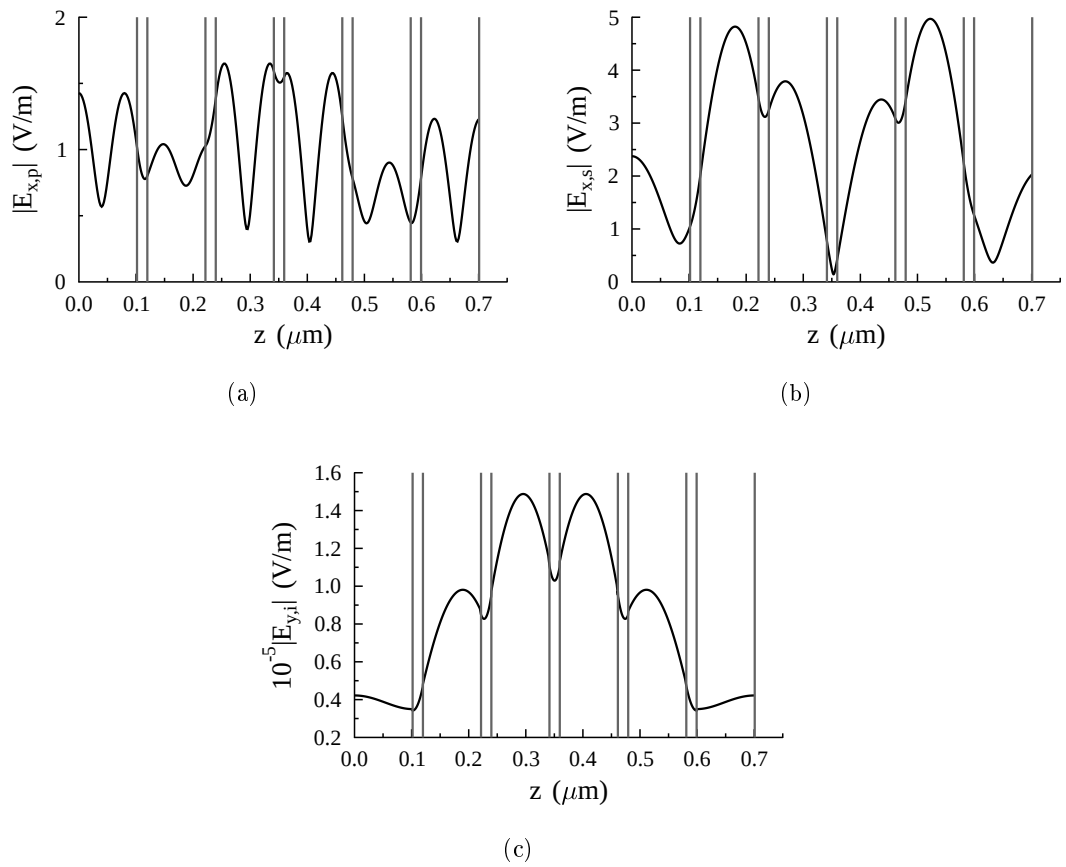

Figure 5.8: Profile of modulus of the electric-field amplitude for (a) pump, (b) signal and (c) idler fields along the z axis for the pump field with amplitude 1 V/m incident at $z = 0$ m and outgoing signal and idler fields with amplitudes 1 V/m at the end of the structure composed of eleven GaN/Ag layers described in the caption of Fig. 5.7. In the TM-polarized idler field, the z component of electric-field amplitude is by several orders in magnitude lower than the plotted y component; $\lambda_p = 400$ nm, $\vartheta_p = 0$ deg, $\lambda_s = 737.8367$ nm, $\vartheta_s = 47.686$ deg, $\lambda_i = 873.6015$ nm, $\vartheta_i = -61.095$ deg.

5.8 Temporal properties of emitted photon pairs

Due to stationarity, the two-photon spectral amplitude $\phi(\omega_s, \omega_i)$ gets a general form $f_i(\omega_i)\delta(\omega_p^0 - \omega_s - \omega_i)$, in which the δ-function expresses the energy conservation law. The squared modulus $|f_i|^2$ is then linearly proportional to the idler spectral photon-number density $n_i^\omega(\omega_i)$. For the analyzed structure, the spectral density n_i^ω of a photon pair with signal photon propagating along direction $\vartheta_s^0 = 47.686$ deg and $\psi_s^0 = 0$ deg

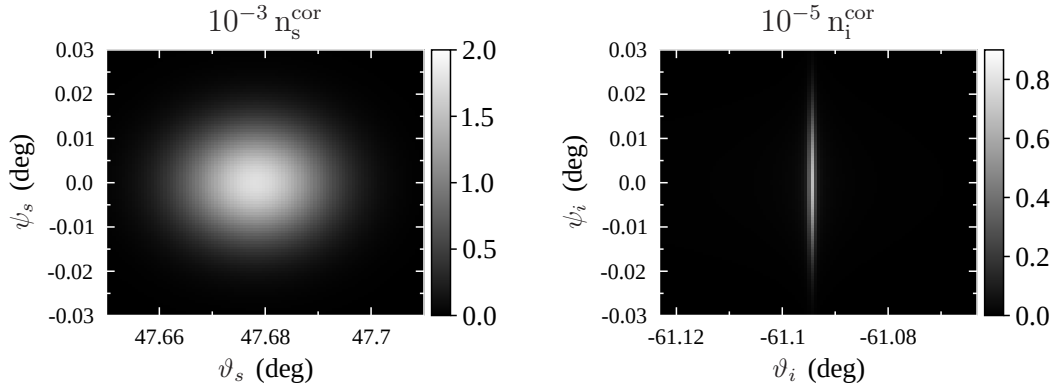

Figure 5.9: Correlated area $n^{\rm cor}$ of (a) signal [(b) idler] photon observed after detection of an idler [signal] photon at direction $\vartheta_i^0 = -61.095$ deg and $\psi_i^0 = 0$ deg [$\vartheta_s^0 = 47.686$ deg and $\psi_s^0 = 0$ deg] for the structure analyzed in Fig. 5.7. The correlated areas are normalized such that $\int d\vartheta \int d\psi\, n^{\rm cor}(\vartheta, \psi) = (\pi/180)^2$.

and idler photon propagating along direction $\vartheta_i^0 = -61.095$ deg and $\psi_i^0 = 0$ deg attains the form of a very narrow peak of width 4.45×10^{-4} nm [FWHM, see Fig. 5.10(a)].

The narrow spectral peak is responsible for longer temporal correlations of fields' intensities compared to those characterizing photon pairs generated in a typical bulk crystals. For the analyzed structure and cw pumping, intensity temporal correlations occur at the time scale of ns [for the conditional probability density p_i of detecting an idler photon at time τ_i, see Fig. 5.10(b)]. It is worth noting that the signal- and idler-field group velocities considerably differ. The TE-polarized signal photons propagate on average faster than the TM-polarized idler photons that undergo on average much higher number of back reflections on the boundaries after their emission. If pulsed SPDC occurred in the structure, the idler-field detection interval would be much wider than that of the signal field.

Different group velocities of the signal and idler photons inside the structure also result in highly asymmetric coincidence-count rate profiles observed in the Hong-Ou-Mandel interferometer, as documented in Fig. 5.11. In this interferometer, a much longer average delay of the idler photon has to be compensated by a delay line placed into the signal-photon path to achieve mutual interference of both photons at a beam splitter. Fast oscillations caused by non-zero difference of the signal and idler central frequencies are also visible in the normalized coincidence-count rate R in Fig. 5.11. It is worth to note that the Hong-Ou-Mandel interferometer represents the simplest tool

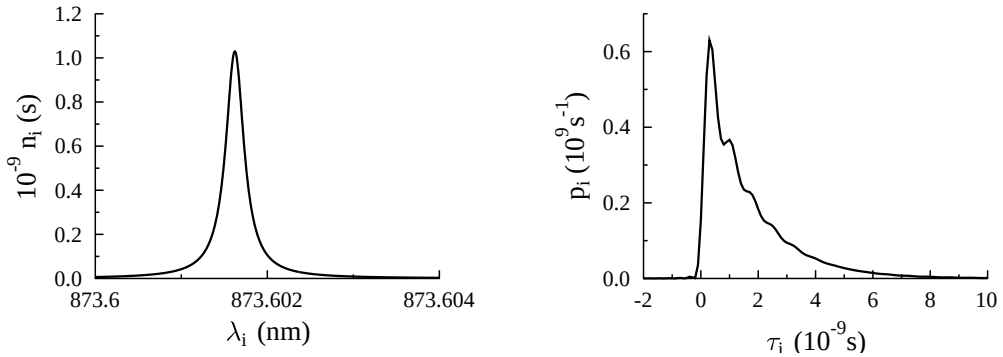

(a) (b)

Figure 5.10: (a) Idler spectral photon-number density n_i as a function of idler wavelength λ_i and (b) probability density p_i of detecting an idler photon at time τ_i provided that its signal twin was detected at time $\tau_s = 0$ s; $p_i(\tau_i) = C|\mathcal{A}(\tau_s = 0, \tau_i)|^2$ using an appropriate normalization constant C. A photon pair is emitted in directions $\vartheta_s = 47.686$ deg and $\psi_s = 0$ deg and $\vartheta_i = -61.095$ deg and $\psi_i = 0$ deg in the structure described in the caption to Fig. 5.7. Normalization is such that $\int d\omega_i\, n_i(\omega_i) = 1$ and $\int d\tau_i\, p_i(\tau_i) = 1$.

for the observation of temporal correlations between photons.

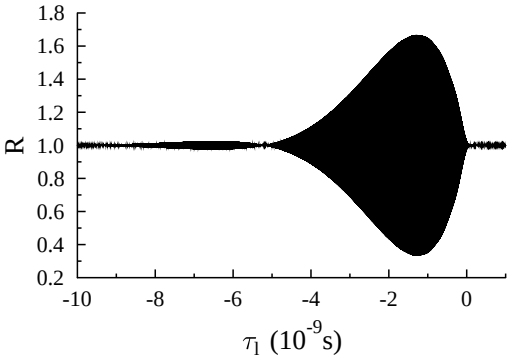

Figure 5.11: Normalized coincidence count rate R in the Hong-Ou-Mandel interferometer depending on mutual time delay τ_l between the signal and idler photons. The structure described in the caption of Fig. 5.7 is analyzed.

5.9 Losses in the structure and noise photons

Non-negligible losses occur in the analyzed metallo-dielectric layered structures because of the presence of highly absorbing metal layers. When one photon from a photon pair is absorbed whereas the other photon leaves the structure, the emitted joint signal and idler field contains also the single-photon noise present both in the signal and idler fields. According to the theory developed in Section 5.5, these noise contributions are comparable to the photon-pair one. Ratios $R_{s,FF}^{\mathrm{TE,TM}}$ and $R_{i,FF}^{\mathrm{TE,TM}}$ given in Eqs. (5.33) in Section 5.5 and quantifying contributions of the signal and idler noise photon-number densities relatively to the photon-number densities n_s and n_i given in Eqs. (5.20), respectively, are plotted in Fig. 5.12. They are appropriate for the structure with 11 layers and the joint signal and idler field composed of the forward-propagating TE-polarized signal and TM-polarized idler photons. From the numbers of emitted signal and idler noise photons follows, that their amount is at the same level as the number of emitted photon pairs. Comparable values of ratios $R_{s,FF}^{\mathrm{TE,TM}}$ (1.20 for $\vartheta_s = 47$ deg and $\lambda_s = 738$ nm) and $R_{i,FF}^{\mathrm{TE,TM}}$ (0.97 for $\vartheta_i = 61$ deg and $\lambda_i = 834$ nm) for the signal noise and idler noise fields at the corresponding radial emission angles ϑ and for the corresponding frequencies ω indicate that the numbers of emitted noise photons depend mainly on the number of photon pairs generated inside the structure. The values of ratios $R_{s,FF}^{\mathrm{TE,TM}}$ and $R_{i,FF}^{\mathrm{TE,TM}}$ increase in the vicinity of forbidden bands, i.e. in the area with strong back-scattering and interference (see Fig. 5.12).

As discussed in Section 5.5, photons from photon pairs in which only one photon enters the detection system represent an additional source of the noise. In the analyzed structure, photon pairs with a forward-propagating TE-polarized signal photon and a backward-propagating TM-polarized idler photon contribute to the noise in the signal field. On the other hand, photon pairs with a backward-propagating TE-polarized signal photon and a forward-propagating TM-polarized idler photon are responsible for an additional noise in the idler field. As the numbers of emitted photon pairs with different propagation directions are comparable, the numbers of noise photons constituting these contributions are also comparable. However, these noise contributions can be decreased if multiple coincidence-count detections are measured.

Considerable amount of the noise present in the generated photon-pair states restricts applicability of such states to the schemes based on coincidence-count measurements. In these schemes, a single-photon noise contributes to the measurement only via random coincidences that are, however, seldom due to the weakness of the field. Possible applications suitable for photon-pair states emitted from metallo-dielectric layered

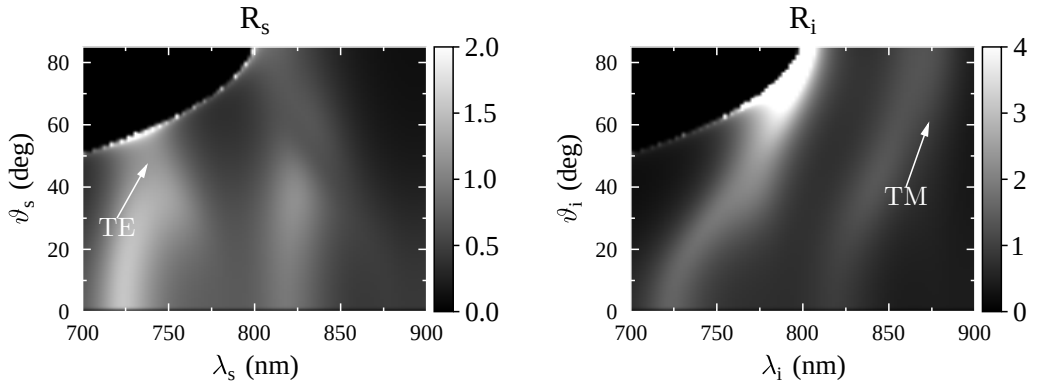

Figure 5.12: Ratio (a) $R_{s,FF}^{\mathrm{TE,TM}}$ [(b) $R_{i,FF}^{\mathrm{TE,TM}}$] of signal [idler] noise photon-number density and photon-pair density in dependence on signal [idler] radial emission angle ϑ_s [ϑ_i] and wavelength λ_s [λ_i] determined along Eq. (5.33) in Section 5.5. The photon-pair field contains the forward-propagating TE-polarized signal and TM-polarized idler photons; $\lambda_p^0 = 400$ nm, $l_1 = 101.752$ nm, $l_2 = 18.083$ nm.

structures include quantum cryptography using photon pairs [122] or quantum optical coherence tomography [123], to name few. On the other hand, these states are not suitable for constructing heralded single-photon sources [124].

Chapter 6

Conclusion

6.1 Summary of the thesis

The introductory Chapter 1 included goals of the thesis (Sec. 1.1) and annotation (Sec. 1.2). The goals of the thesis defined the objects of the research and required results. The annotation described the content of the thesis.

Non-linear phenomena of the second order were introduced in Chapter 2. The linear and non-linear vectors of polarization for dispersive and non-dispersive media were defined in Section 2.1. Non-linear susceptibility of the second order was defined as well. At the end of the Section, equation of coupled waves in non-linear medium was derived. The non-linear processes of the second order were described in Section 2.2. Namely, the second-harmonic generation, sum-frequency generation and difference-frequency generation. The electron transition schemes were used to describe the interactions microscopically.

The properties and use of photon pairs together with the process of their generation were described in Chapter 3. A brief historical introduction mentioning a milestone, which started an era of quantum physics, was given in Section 3.1.1. The quantization procedure of electromagnetic field was described in Section 3.1.2. The properties and usefulness of photon pairs in experimental and theoretical physics were summarized in Section 3.2. The simplest mean of generation of photon pairs - in bulk crystal, is described in Section 3.3. The approach for preparation of photon pairs entangled is frequency, emission direction and polarization were explained.

The generation of photon pairs in a periodically-poled silica ring fiber was studied in Chapter 4. The introduction (Sec. 4.1) covered an overview about integrated photon pairs sources (Sec. 4.1.1), explained the benefits and usefulness of fields carrying orbital

angular momentum (Sec. 4.1.2) and described periodical poling process along with the concept of quasi-phase matching (Sec. 4.1.3). Theoretical approach of SPDC in a fiber was developed in Section 4.2. It included analytical expressions for the modes of the fiber, derivation of a resulting quantum state vector and definitions of quantities characteristic for a photon pair. The theory covering decomposition of transverse profiles of the modes to basis of OAM eigenstates was provided in Section 4.3. The decomposition of a two photon amplitude in the transverse spatial domain as well as in frequency domain to the Schmidt basis was mentioned. The approximative and rigorous formulas for obtaining the effective dimension of the entangled space were defined. The guided modes of the fiber were characterized in Section 4.4. The approach for derivation of an implicit dispersion equation was explained. The effective indicies of refraction of the guided modes for a particular fiber were shown. For the modes of interest, the transversal spatial profiles were depicted together with their angular spectral weights. The spectrally narrow generation of photon pairs in the fiber was investigated in Section 4.5. Particularly, the modes with OAM number equal to $0, +1$ were generated by a pump beam with OAM number equal to $+1$. The emission of spectrally broad-band photon pairs was examined in Section 4.6. The pump beam with OAM number 0 generated photon pairs with photons in TE_{01} modes. The temporal features of both narrow-band and broad-band emission schemes were explored. The generation of photon pairs entangled in frequency and OAM was studied in Section 4.7. The photon pairs consisting of photons with OAM number ± 1 were generated by a pump beam with OAM number equal to 0. The states entangled in OAM were simultaneously entangled in the frequency domain. The impact of noise on the entanglement of photon pairs (entangled in OAM) was studied by means of the Clauser-Horne-Shimony-Holt form of the Bell inequalities.

The emission of photon pairs from metallo-dielectric layered structures consisting of Gallium-Nitride (GaN) and silver (Ag) layers was explored in Chapter 5. The introduction (Sec. 5.1) described advantages and disadvantages of the layered structures and summarized current state of art. The non-linear model of metal was developed in Section 5.7. Outcome of the model was non-linear susceptibility tensor of the second order. The theoretical framework of SPDC was derived in Section 5.3. It covered quantization of modes of layered structure and derivation of the photon-pair state vector. The quantities characterizing the emitted photon pairs were defined in Section 5.4. The theory evaluating the photon losses in the structure was derived in Section 5.5. In Section 5.6 photon pair generation from Ag-GaN-Ag resonator was studied. The design procedure was applied in order to obtain the most efficient structure. The emission rate of the

resonator was compared with the reference structure and with a single GaN monolayer of the same length. A structure with eleven layers was investigated along the same vain in Section 5.7. The spatial mode profiles, corresponding to the most intense generation, were plotted for pump, signal and idler electric field intensity components. The correlated areas around the emission maxima were investigated. The temporal properties of the photon pairs were examined in the Section 5.8. The number of noise photons was investigated in Section 5.9.

The Conclusion summarizes content of the thesis in Chapter 6 followed by the list of author's publications (p. 102) and bibliography (p. 103).

6.2 Shrnutí v češtině

Úvodní Kapitola 1 obsahuje cíle práce (Sek. 1.1) a anotaci (Sek. 1.2). Cíle práce konkrétně specifikovaly zadaný výzkumný úkol a požadované výsledky. Anotace popisovala obsah práce.

Nelineární jevy druhého řádu byly uvedeny v Kapitole 2. Lineární a nelineární vektory polarizace pro nedisperzní a disperzní prostředí byly definovány v Sekci 2.1. Společně s nimi byla definována nelinární susceptibilita druhého řádu. Na konci sekce byla odvozena rovnice vázaných vln. Nelineární procesy druhého řádu byly uvedeny a popsány v Sekci 2.2. Jmenovitě, generace druhé harmonické, součtové frekvence a rozdílové frekvence. Procesy byly analyzovány jak matematicky, tak mikroskopicky pomocí schémat elektronových přechodů v atomech.

Vlastnosti a použití fotonových párů společně s principem jejich generace byly popsány v Kapitole 3. Stručný historický úvod zmiňuje klíčový objev, který odstartoval éru kvantové fyziky (Sek. 3.1.1). Procedura pro kvantování elektromagnetického pole byla popsána v Sekci 3.1.2. Vlastnosti a užitečnost fotonových párů v teoretické a experimentální fyzice byly shrnuty v Sekci 3.2. Nejjednodušší způsob generace fotonových párů - v objemovém nelineárním krystalu, byl popsán v Sekci 3.3. Navíc byly vysvětleny způsoby experimentální přípravy fotonových párů kvantově korelovaných ve frekvenci, směru šíření a polarizaci.

Generace fotonových párů v periodicky pólovaném skleněném vlákně s prstencovým profilem byla popsána v Kapitole 4. Úvod (Sek. 4.1.1) zahrnoval přehled integrovaných zdrojů fotonových párů. Výhody a užitečnost polí s úhlovým momentem byly popsány v Sekci 4.1.2. Experimentální procedura periodického pólování skleněných vláken společně s konceptem kvazi-sfázování byly ozřejmeny v Sekci 4.1.3. Teorie popisující spontánní parametrickou sestupnou frekvenční konverzi (SPDC) ve vlákně byla uve-

dena v Sekci 4.2. Obsahovala analytické vyjádření módů vlákna, odvození generovaného kvantového stavu a definice veličin charakterizujících fotonových pár. Teorie zahrnující dekompozici příčných profilů módů do báze vlastních stavů operátoru úhlového momentu byla popsána v Sekci 4.3. Zmíněna byla též dekompozice dvoufotonové amplitudy do Schmidtovy báze a to jak v prostorové příčné doméně, tak ve frekvenční oblasti. Definovány byly rigorózní i aproximativní rovnice vyčíslující efektivní dimenzi entanglovaného prostoru. Vedené módy vlákna byly charakterizovány v Sekci 4.4. Vysvětleno bylo odvození implicitní disperzní rovnice a byly ukázány efektivní indexy lomu vedených módů. Pro vybrané módy byly zobrazeny profily složek elektrických polí společně s jejich úhlovým spektrem. Úzko-spektrální generace fotonových párů byla zkoumána v Sekci 4.5. Konkrétně byla studována konfigurace, kdy čerpací svazek s kvantovým číslem úhlového momentu (OAM) +1 generoval fotonové páry s kvantovým číslem OAM 0 a +1. Široko-spektrální emise fotonových párů byla analyzována v Sekci 4.6. Čerpací svazek s kvantovým číslem OAM 0 generoval fotonové páry v módech TE_{01}. Časové vlastnosti úzko- a široko-spektrálního procesu byly prověřeny na konci kapitoly. Generace fotonových párů entanglovaných současně v OAM a frekvenci byla studována v Sekci 4.7. Fotonové páry se skládaly z fotonů s kvantovým číslem OAM ± 1 a byly tvořeny čerpacím svazkem s OAM číslem 0. Vliv šumu na entanglement v OAM byl studován pomocí Clauser-Horne-Shimony-Holt nerovnosti Bellova typu.

Emise fotonových párů z metalo-dielektrických vrstevnatých struktur skládajících se z Gallium-Nitridu (GaN) a stříbra (Ag) byla analyzována v Kapitole 5. Úvod (Sek. 5.1) popisuje výhody a nevýhody vrstevnatých struktur a shrnuje současný stav v daném oboru. Nelineární model kovu byl odvozen v Sekci 5.2. Výsledkem modelu byl nelineární tensor susceptibility druhého řádu. Teoretický rámec spontánně parametrického frekvenčně sestupného procesu byl odvozen v Sekci 5.3. Zahrnoval kvantování pole ve vrstevnatých strukturách a odvození dvoufotonového kvantového stavu. Veličiny charakterizující fotonový pár byly definovány v Sekci 5.4. Teorie vyhodnocující fotonové ztráty byla odvozena v Sekci 5.5. V Sekci 5.6 byla studována emise fotonových párů z Ag-GaN-Ag rezonátoru. Konkrétní struktura byla navržena tak, aby směrově a frekvenčně emitovala co největší počet fotonových párů. Míra emise byla porovnána s mírou emise z referenční struktury a GaN monovrstvy o stejné délce. Struktura s jedenácti vrstvami byla zkoumána stejným způsobem. V oblasti nejintenzivnější emise byly studovány prostorové módy čerpacího, signálového a jalového elektrického pole. Předmětem výzkumu byly také korelované plochy. Časové vlastnosti fotonových párů byly studovány v Sekci 5.8. Počet šumových fotonů byl analyzován v Sekci 5.9.

Shrnutí práce se nachází v Kapitole 6. A to jak v anglickém (Sek. 6.1), tak českém

(Sek. 6.2) jazyce. Vědecké publikace autora práce se nacházejí na straně 102. Reference na použitou literaturu pak na straně 103.

List of author's publications

[A1] D. Javůrek, J. Svozilík, and J. Peřina Jr., "Proposal for the generation of photon pairs with nonzero orbital angular momentum in a ring fiber," Opt. Express **22**, 23743–23748 (2014).

[A2] D. Javůrek, J. Svozilík, and J. Peřina, "Emission of orbital-angular-momentum-entangled photon pairs in a nonlinear ring fiber utilizing spontaneous parametric down-conversion," Phys. Rev. A **90**, 043844 (2014).

[A3] D. Javůrek, J. Svozilík, and J. Peřina Jr., "Entangled photon-pair generation in metallo-dielectric photonic bandgap structures," in "Wave and Quantum Aspects of Contemporary Optics," , vol. 8697 of *SPIE Conference proceedings*, J. Peřina Jr., L. Nožka, M. Hrabovský, D. Senderáková, W. Urbanczyk, and O. Haderka, eds., p. 869727 (2012).

[A4] D. Javůrek, J. Svozilík, and J. Peřina, "Photon-pair generation in nonlinear metal-dielectric one-dimensional photonic structures," Phys. Rev. A **90**, 053813 (2014).

[A5] D. Javůrek, J. Peřina Jr., and J. Svozilík, "Spontaneous parametric down conversion in nonlinear metallo-dielectric layered media," in "Wave and Quantum Aspects of Contemporary Optics," , vol. 8697 of *SPIE Conference proceedings*, W. U. A. Popiolek-Masajada, eds., p. 94410V (2014).

Bibliography

[1] P. A. Franken, A. E. Hill, C. W. Peters, and G. Weinreich, "Generation of optical harmonics," Phys. Rev. Lett. **7**, 118–119 (1961).

[2] R. W. Boyd, *Nonlinear Optics* (Academic Press, 2008), 3rd ed.

[3] M. Dušek, *Koncepční otázky kvantové teorie* (Univerzita Palackého v Olomouci, 2002).

[4] W. H. Luisell, *Quantum statistical properties of radiation* (John Wiley & Sons, Inc., 1973).

[5] A. Das, *Lectures on Quantum Field Theory* (World Scientific Publishing Co. Pte. Ltd., 2008).

[6] W. H. Louisell, A. Yariv, and A. E. Siegman, "Quantum fluctuations and noise in parametric processes. I." Phys. Rev. **124**, 1646–1654 (1961).

[7] S. E. Harris, M. K. Oshman, and R. L. Byer, "Observation of tunable optical parametric fluorescence," Phys. Rev. Lett. **18**, 732–734 (1967).

[8] D. Magde and H. Mahr, "Study in ammonium dihydrogen phosphate of spontaneous parametric interaction tunable from 4400 to 16 000 Å," Phys. Rev. Lett. **18**, 905–907 (1967).

[9] A. Aiello, G. Puentes, D. Voigt, and J. P. Woerdman, "Maximally entangled mixed-state generation via local operations," Phys. Rev. A **75**, 062118 (2007).

[10] M. Hamar, J. Peřina Jr., O. Haderka, and V. Michálek, "Transverse coherence of photon pairs generated in spontaneous parametric down-conversion," Phys. Rev. A **81**, 043827 (2010).

[11] C. K. Hong, Z. Y. Ou, and L. Mandel, "Measurement of subpicosecond time intervals between two photons by interference," Phys. Rev. Lett. **59**, 2044–2046 (1987).

[12] A. Joobeur, B. E. A. Saleh, T. S. Larchuk, and M. C. Teich, "Coherence properties of entangled light beams generated by parametric down-conversion: Theory and experiment," Phys. Rev. A **53**, 4360–4371 (1996).

[13] C. P. Cristescu and M. Popescu, "Entangled quantum states, quantum teleportation and quantum information," U.P.B. Sci. Bull. A **71**, 77–94 (2009).

[14] M. Aspelmeyer, H. R. Böhm, A. Fedrizzi, S. Gasparoni, M. Lindenthal, G. Molina-Terriza, A. Poppe, K. Resch, R. Ursin, P. Walther, A. Zeilinger, and T. Jennewein, *Quantum communication and crypthography* (CRC Press, Florida, US, 2005).

[15] T. B. Pittman, Y. H. Shih, A. V. Sergienko, and M. H. Rubin, "Experimental tests of Bell's inequalities based on space-time and spin variables," Phys. Rev. A **51**, 3495–3498 (1995).

[16] A. Einstein, B. Podolsky, and N. Rosen, "Can quantum-mechanical description of physical reality be considered complete?" Phys. Rev. **47**, 777–780 (1935).

[17] Y. H. Shih, A. V. Sergienko, and M. H. Rubin, "Einstein-Podolsky-Rosen state for space-time variables in a two-photon interference experiment," Phys. Rev. A **47**, 1288–1293 (1993).

[18] P. G. Kwiat, K. Mattle, H. Weinfurter, A. Zeilinger, A. V. Sergienko, and Y. Shih, "New high-intensity source of polarization-entangled photon pairs," Phys. Rev. Lett. **75**, 4337–4341 (1995).

[19] D. Bouwmeester, J. V. Pan, K. Mattle, M. Eibl, H. Weinfurter, and A. Zeilinger, "Experimental quantum teleportation," Nature **390**, 575–579 (1997).

[20] G. Ribordy, J. Brendel, J. Gautier, N. Gisin, and H. Zbinden, "Long-distance entanglement-based quantum key distribution," Phys. Rev. A **63**, 012309 (2000).

[21] T. E. Chapuran, P. Toliver, N. A. Peters, J. Jackel, M. S. Goodman, R. J. Runser, S. R. McNown, N. Dallmann, R. J. Hughes, K. P. McCabe, J. E. Nordholt, C. G. Peterson, K. T. Tyagi, L. Mercer, and H. Dardy, "Optical networking for quantum key distribution and quantum communications," New J. Phys. **11**, 105001 (2009).

[22] M. A. Nielsen and I. L. Chuang, *Quantum computation and quantum information* (Cambridge University Press, 2010).

[23] P. Zhang, X.-F. Ren, X.-B. Zou, B.-H. Liu, Y.-F. Huang, and G.-C. Guo, "Demonstration of one-dimensional quantum random walks using orbital angular momentum of photons," Phys. Rev. A **75**, 052310 (2007).

[24] A. Migdall, "Correlated-photon metrology without absolute standards," Physics Today **52**, 41–46 (1999).

[25] A. Fraine, O. Minaeva, D. S. Simon, R. Egorov, and A. V. Sergienko, "Evaluation of polarization mode dispersion in a telecommunication wavelength selective switch using quantum interferometry," Opt. Express **20**, 2025–2033 (2012).

[26] N. Uribe-Patarroyo, A. Fraine, D. S. Simon, O. Minaeva, and A. V. Sergienko, "Object identification using correlated orbital angular momentum states," Phys. Rev. Lett. **110**, 043601 (2013).

[27] D. L. Moehring, P. Maunz, S. Olmschenk, K. C. Younge, D. N. Matsukevich, L. M. Duan, and C. Monroe, "Entanglement of single-atom quantum bits at a distance," Nature **449**, 68–71 (2007).

[28] T. E. Keller and M. H. Rubin, "Theory of two-photon entanglement for spontaneous parametric down-conversion driven by a narrow pump pulse," Phys. Rev. A **56**, 1534–1541 (1997).

[29] J. Svozilík, M. Hendrych, A. S. Helmy, and J. P. Torres, "Generation of paired photons in a quantum separable state in bragg reflection waveguides," Opt. Express **19**, 3115–3123 (2011).

[30] W. P. Grice, R. S. Bennink, Z. Zhao, K. Meyer, W. Whitten, and R. Shaw, "Spectral and spatial effects in spontaneous parametric down-conversion with a focused pump," in "Quantum Communications and Quantum Imaging VI," , vol. 7092 of *SPIE Conference Series*, p. 70920Q (2008).

[31] C. K. Law and J. H. Eberly, "Analysis and interpretation of high transverse entanglement in optical parametric down conversion," Phys. Rev. Lett. **92**, 127903 (2004).

[32] S. E. Harris, "Chirp and compress: Toward single-cycle biphotons," Phys. Rev. Lett. **98**, 063602 (2007).

[33] J. Peřina Jr., M. Centini, C. Sibilia, M. Bertolotti, and M. Scalora, "Anti-symmetric entangled two-photon states generated in nonlinear GaN/AlN photonic-band-gap structures," Phys. Rev. A **75**, 013805 (2007).

[34] P. Ni, B. Ma, X. Wang, B. Cheng, and D. Zhang, "Second-harmonic generation in two-dimensional periodically poled lithium niobate using second-order quasiphase matching," Apl. Opt. **82**, 4230–4232 (2003).

[35] G. Brida, M. V. Chekhova, I. P. Degiovanni, M. Genovese, G. K. Kitaeva, A. Meda, and O. A. Shumilkina, "Chirped biphotons and their compression in optical fibers," Phys. Rev. Lett. **103**, 193602 (2009).

[36] B. Jost, A. Sergienko, A. Abouraddy, B. Saleh, and M. Teich, "Spatial correlations of spontaneously down-converted photon pairs detected with asingle-photon-sensitive CCD camera," Opt. Express **3**, 81–88 (1998).

[37] M. H. Rubin and Y. Shih, "Resolution of ghost imaging for nondegenerate spontaneous parametric down-conversion," Phys. Rev. A **78**, 033836 (2008).

[38] A. Avella, M. Gramegna, A. Shurupov, G. Brida, M. Chekhova, and M. Genovese, "Separable Schmidt modes of a nonseparable state," Phys. Rev. A **89**, 023808 (2014).

[39] A. L. E. Jin, *Entangled state preparation for optical quantum communication: Creating and characterizing photon pairs from Spontaneous parametric down conversion inside bulk uniaxial crystals* (National University of Singapore, Singapore, 2008).

[40] A. Fraine, O. Minaeva, D. S. Simon, R. Egorov, and A. V. Sergienko, "Broadband source of polarization entangled photons," Opt. Lett. **37**, 1910–1912 (2012).

[41] A. Christ, K. Laiho, A. Eckstein, T. Lauckner, P. J. Mosley, and C. Silberhorn, "Spatial modes in waveguided parametric down-conversion," Phys. Rev. A **80**, 033829 (2009).

[42] H. Herrmann, X. Yang, A. Thomas, A. Poppe, W. Sohler, and C. Silberhorn, "Post-selection free, integrated optical source of non-degenerate, polarization entangled photon pairs," Opt. Express **21**, 27981–27991 (2013).

[43] G. Harder, V. Ansari, B. Brecht, T. Dirmeier, C. Marquardt, and C. Silberhorn, "An optimized photon pair source for quantum circuits," Opt. Express **21**, 13975–13985 (2013).

[44] M. Jachura, M. Karpinski, C. Radzewicz, and K. Banaszek, "High-visibility non-classical interference of photon pairs generated in a multimode nonlinear waveguide," Opt. Express **22**, 8624—8632 (2014).

[45] E. Y. Zhu, Z. Tang, L. Qian, L. G. Helt, M. Liscidini, J. E. Sipe, C. Corbari, A. Canagasabey, M. Ibsen, and P. G. Kazansky, "Direct generation of polarization-entangled photon pairs in a poled fiber," Phys. Rev. Lett. **108**, 213902 (2012).

[46] T. G. Euser, G. Whyte, M. Scharrer, J. S. Y. Chen, A. Abdolvand, J. Nold, C. F. Kaminski, and P. S. J. Russell, "Dynamic control of higher-order modes in hollow-core photonic crystal fibers," Opt. Express **16**, 17972–17981 (2008).

[47] S. Ramachandran, P. Kristensen, and M. F. Yan, "Generation and propagation of radially polarized beams in optical fibers," Opt. Lett. **34**, 2525–2527 (2009).

[48] N. Bozinovic, Y. Yue, Y. Ren, M. Tur, P. Kristensen, H. Huang, A. E. Willner, and S. Ramachandran, "Terabit-scale orbital angular momentum mode division multiplexing in fibers," Science **340**, 1545–1548 (2013).

[49] Y. Yue, Y. Yan, N. Ahmed, J.-Y. Yang, L. Zhang, Y. Ren, H. Huang, K. M. Birnbaum, B. I. Erkmen, S. Dolinar *et al.*, "Mode properties and propagation effects of optical orbital angular momentum (OAM) modes in a ring fiber," IEEE Phot. J. **4** (2012).

[50] A. W. Snyder and J. D. Love, *Optical Waveguide Theory* (Chapman & Hall, London, 1983).

[51] C. Yeh and F. Shimabukuro, *The Essence of Dielectric Waveguides* (Springer, 2010).

[52] M. Padgett and R. Bowman, "Tweezers with a twist," Nature Photonics **5**, 343–348 (2011).

[53] B. Guan, R. P. Scott, C. Qin, N. K. Fontaine, T. Su, C. Ferrari, M. Cappuzzo, F. Klemens, B. Keller, M. Earnshaw *et al.*, "Free-space coherent optical communication with orbital angular momentum multiplexing/demultiplexing using a hybrid 3D photonic integrated circuit," Optics Express **22**, 145–156 (2014).

[54] C. S. Hamilton, A. Gábris, I. Jex, and S. M. Barnett, "Quantum walk with a four-dimensional coin," New J. Phys. **13**, 013015 (2011).

[55] S. K. Goyal, F. S. Roux, A. Forbes, and T. Konrad, "Implementing quantum walks using orbital angular momentum of classical light," Phys. Rev. Lett. **110**, 263602 (2013).

[56] L.-P. Deng, H. Wang, and K. Wang, "Quantum CNOT gates with orbital angular momentum and polarization of single-photon quantum logic," JOSA B **24**, 2517–2520 (2007).

[57] C. T. Schmiegelow and F. Schmidt-Kaler, "Light with orbital angular momentum interacting with trapped ions," Eur. Phys. J. D. **66**, 1–9 (2012).

[58] J. A. Armstrong, N. Bloembergen, J. Ducuing, and P. S. Pershan, "Interactions between light waves in a nonlinear dielectric," Phys. Rev. **127**, 1918–1939 (1962).

[59] P. A. Franken and J. F. Ward, "Optical harmonics and nonlinear phenomena," Rev. Mod. Phys. **35**, 23–39 (1963).

[60] J. Svozilík, "Entangled photon pairs in modern photonic structures," Ph.D. thesis, Palacký University (2013).

[61] G. D. Miller, "Periodically poled lithium niobate: Modelling, fabrication, and nonlinear-optical performance," Ph.D. thesis, Stanford University (1998).

[62] M. Dussauze, T. Cremoux, F. Adamietz, V. Rodriguez, E. Fargin, G. Yang, and T. Cardinal, "Thermal poling of optical glasses: Mechanisms and second-order optical properties," International Journal of Applied Glass Science **3**, 309–320 (2012).

[63] H. Ishizuki, I. Shoji, T. Taira, and S. Kurimura, "Fabrication of periodical poling in 3mm-thick MgO:LiNbO3 crystals at elevated temperature," in "Conference on Lasers and Electro-Optics/Quantum Electronics and Laser Science Conference," p. CMF5 (Optical Society of America, 2003).

[64] H. Karlsson, "Fabrication of periodically poled crystals from the KTP family and their applications in nonlinear optics," Ph.D. thesis, Royal Institute of Technology.

[65] M. M. Fejer, G. A. Magel, D. H. Jundt, and R. L. Byer, "Quasi-phase-matched second harmonic generation - Tuning and tolerances," IEEE J. Quant. Electr. **28**, 2631–2654 (1992).

[66] K. P. Huy, A. T. Nguyen, E. Brainis, M. Haelterman, P. Emplit, C. Corbari, A. Canagasabey, P. G. Kazansky, O. Deparis, A. A. Fotiadi, P. Mégret, and S. Massar, "Photon pair source based on parametric fluorescence in periodically poled twin-hole silica fiber," Opt. Express **15**, 4419–4426 (2007).

[67] J. Zhang, "Thermal poling of twin-hole fibers," Master's thesis, Department of Electrical and Computer Engineering, University of Toronto (2008).

[68] A. Canagasabey, C. Corbari, F. Liegeois, A. Gladyshev, S. Guillemet, Y. Hernandez, E. Dianov, M. Ibsen, and P. Kazansky, "236mW average second-harmonic power generated from periodically poled silica fibres," in "Lasers and Electro-Optics 2009 and the European Quantum Electronics Conference. CLEO Europe - EQEC 2009," (2009), p. 1.

[69] X. Li, P. L. Voss, J. E. Sharping, and P. Kumar, "Optical-fiber source of polarization-entangled photons in the 1550 nm telecom band," Phys. Rev. Lett. **94**, 053601 (2005).

[70] J. Fulconis, O. Alibart, W. Wadsworth, P. Russell, and J. Rarity, "High brightness single mode source of correlated photon pairs using a photonic crystal fiber," Opt. Express **13**, 7572—7582 (2005).

[71] J. Fan, A. Migdall, and L. J. Wang, "Efficient generation of correlated photon pairs in a microstructure fiber," Opt. Lett. **30**, 3368—3370 (2005).

[72] L. Mandel and E. Wolf, *Optical Coherence and Quantum Optics* (Cambridge Univ. Press, Cambridge, 1995).

[73] Q. Lin, O. J. Painter, and G. P. Agrawal, "Nonlinear optical phenomena in silicon waveguides: modeling and applications," Opt. Express **15**, 16604–16644 (2007).

[74] E. Y. Zhu, L. Qian, L. G. Helt, M. Liscidini, J. E. Sipe, C. Corbari, A. Canagasabey, M. Ibsen, and P. G. Kazansky, "Measurement of $\chi(2)$ symmetry in a poled fiber," Opt. Lett. **35**, 1530–1532 (2010).

[75] W. Vogel, D. G. Welsch, and S. Walentowicz, *Quantum Optics* (Wiley-VCH, Weinheim, 2001).

[76] B. Huttner, S. Serulnik, and Y. Ben-Aryeh, "Quantum analysis of light propagation in a parametric amplifier," Phys. Rev. A **42**, 5594–5600 (1990).

[77] V. Brückner, *Elements of Optical Networking* (Springer Fachmedien Wiesbaden GmbH: Vieweg+Teubner Verlag, 2011).

[78] T. L. Huynh, "Dispersion in photonic systems," Tech. rep., Dept. Electrical Computer Systems Engineering, Monash University (2004).

[79] J. Peřina Jr., A. V. Sergienko, B. M. Jost, B. E. A. Saleh, and M. C. Teich, "Dispersion in femtosecond entangled two-photon interference," Phys. Rev. A **59**, 2359–2368 (1999).

[80] C. K. Law and J. H. Eberly, "Analysis and interpretation of high transverse entanglement in optical parametric down conversion," Phys. Rev. Lett. **92**, 127903 (2004).

[81] G. Molina-Terriza, J. P. Torres, and L. Torner, "Management of the angular momentum of light: Preparation of photons in multidimensional vector states of angular momentum," Phys. Rev. Lett. **88**, 013601 (2001).

[82] C. I. Osorio, G. Molina-Terriza, and J. P. Torres, "Correlations in orbital angular momentum of spatially entangled paired photons generated in parametric down-conversion," Phys. Rev. A **77**, 015810 (2008).

[83] J. T. Barreiro, N. K. Langford, N. A. Peters, and P. G. Kwiat, "Generation of hyperentangled photon pairs," Phys. Rev. Lett. **95**, 260501 (2005).

[84] D. Kang, L. G. Helt, S. V. Zhukovsky, J. P. Torres, J. E. Sipe, and A. S. Helmy, "Hyperentangled photon sources in semiconductor waveguides," Phys. Rev. A **89**, 023833 (2014).

[85] M. Karpinski, C. Radzewicz, and K. Banaszek, "Experimental characterization of three-wave mixing in a multimode nonlinear $KTiOPO_4$ waveguide," Appl. Phys. Lett. **94**, 181105 (2009).

[86] R. Machulka, J. Svozilík, J. Soubusta, J. Peřina Jr., and O. Haderka, "Spatial and spectral properties of the pulsed second-harmonic generation in a PP-KTP waveguide," Phys. Rev. A **87**, 013836 (2013).

[87] J. Peřina Jr., "Spatial properties of entangled photon pairs generated in nonlinear layered structures," Phys. Rev. A **84**, 053840 (2011).

[88] J. Svozilík and J. Peřina Jr., "Properties of entangled photon pairs generated in periodically poled nonlinear crystals," Phys. Rev. A **80**, 023819 (2009).

[89] J. Svozilík and J. Peřina Jr., "Intense ultra-broadband down-conversion from randomly poled nonlinear crystals," Opt. Express **18**, 27130–27135 (2010).

[90] S. Carrasco, J. P. Torres, L. Torner, A. V. Sergienko, B. E. A. Saleh, and M. C. Teich, "Enhancing the axial resolution of quantum optical coherence tomography by chirped quasi-phase matching," Opt. Lett. **29**, 2429–2431 (2004).

[91] J. Svozilík, J. Peřina Jr., and J. P. Torres, "High spatial entanglement via chirped quasi-phase-matched optical parametric down-conversion," Phys. Rev. A **86**, 052318 (2012).

[92] M. Fokine, L. E. Nilsson, A. Claesson, D. Berlemont, L. Kjellberg, L. Krummenacher, and W. Margulis, "Integrated fiber Mach-Zehnder interferometer for electro-optic switching," Opt. Lett. **27**, 1643–1645 (2002).

[93] J. F. Clauser, M. A. Horne, A. Shimony, and R. A. Holt, "Proposed experiment to test local hidden-variable theories," Phys. Rev. Lett. **23**, 880 (1969).

[94] R. Horodecki, P. Horodecki, and M. Horodecki, "Violating Bell inequality by mixed spin-12 states: Necessary and sufficient condition," Phys. Lett. A **200**, 340–344 (1995).

[95] M. McLaren, M. Agnew, J. Leach, F. S. Roux, M. J. Padgett, R. W. Boyd, and A. Forbes, "Entangled Bessel-Gaussian beams," Opt. Express **20**, 23589–23597 (2012).

[96] J. Leach, B. Jack, J. Romero, M. Ritsch-Marte, R. Boyd, A. Jha, S. Barnett, S. Franke-Arnold, and M. Padgett, "Violation of a Bell inequality in two-dimensional orbital angular momentum state-spaces," Opt. Express **17**, 8287–8293 (2009).

[97] M. Scalora, M. J. Bloemer, A. S. Manka, J. P. Dowling, C. M. Bowden, R. Viswanathan, and J. W. Haus, "Pulsed second-harmonic generation in nonlinear, one-dimensional, periodic structures," Phys. Rev. A **56**, 3166–3174 (1997).

[98] M. Centini, J. Peřina Jr., L. Sciscione, C. Sibilia, M. Scalora, M. J. Bloemer, and M. Bertolotti, "Entangled photon pair generation by spontaneous parametric down-conversion in finite-length one-dimensional photonic crystals," Phys. Rev. A **72**, 033806 (2005).

[99] J. Peřina Jr., M. Centini, C. Sibilia, M. Bertolotti, and M. Scalora, "Properties of entangled photon pairs generated in one-dimensional nonlinear photonic-band-gap structures," Phys. Rev. A **73**, 033823 (2006).

[100] M. J. Roberts, A. Guenthner, G. Lindsay, and S. Feng, "Fabrication of multilayer metal-dielectric nanofilms for coupled plasmon resonant devices," in "Symposium J – Negative Index Materials – From Microwave to Optical," , vol. 919 of *MRS Proceedings* (2006).

[101] Y. Tanaka, M. Murata, M. Kumagai, A. Kobayashi, and T. Shinawaga, "Fabrication of Al(2)O(3)/TiO(2) multilayer mirrors for "water-window" attosecond pulses," in "Synthesis and Photonics of Nanoscale Materials VII," , vol. 7586 of *Proceedings of SPIE-The International Society for Optical Engineering*, p. 75860J (2010).

[102] R. Hussin, K. L. Choy, and X. Hou, "Fabrication of multilayer ZnO/TiO2/ZnO thin films with enhancement of optical properties by atomic layer deposition (ALD)," in "4th Mechanical and Manufacturing Engineering, pts 1 and 2," , vol. 465-466 of *Applied Mechanics and Materials*, p. 916–921 (2013).

[103] J. Peřina Jr., M. Centini, C. Sibilia, and M. Bertolotti, "Random nonlinear layered structures as sources of photon pairs for quantum-information processing," J. Russ. Laser Res. **30**, 508–513 (2009).

[104] J. Peřina Jr., M. Centini, C. Sibilia, and M. Bertolotti, "Photon-pair generation in random nonlinear layered structures," Phys. Rev. A **80**, 033844 (2009).

[105] J. Peřina Jr., A. Lukš, O. Haderka, and M. Scalora, "Surface spontaneous parametric down-conversion," Phys. Rev. Lett. **103**, 063902 (2009).

[106] J. Peřina Jr., A. Lukš, and O. Haderka, "Emission of photon pairs at discontinuities of nonlinearity," Phys. Rev. A **80**, 043837 (2009).

[107] V. Peřinová, A. Lukš, and J. Peřina Jr., "Quantization of radiation emitted at discontinuities of nonlinearity," Phys. Scr. **153**, 014050 (2013).

[108] M. Scalora, M. J. Bloemer, and C. M. Bowden, "Laminated photonic band structures with high conductivity and high transparency: Metals under a new light," Opt. Photon. News **10**, 24–27 (1999).

[109] M. R. Gadsdon, J. Parsons, and J. R. Sambles, "Electromagnetic resonances of a multilayer metal-dielectric stack," J. Opt. Soc. Am. B **26**, 734–742 (2009).

[110] J. Peřina Jr., "Spontaneous parametric down-conversion in nonlinear layered media," in "Progress in Optics," , vol. 59, E. Wolf, ed., p. 89–158 (Elsevier, 2014).

[111] P. Kolchin, S. Du, C. Belthangady, G. Y. Yin, and S. E. Harris, "Generation of narrow-bandwidth paired photons: Use of a single driving laser," Phys. Rev. Lett. **97**, 113602 (2006).

[112] J. M. Raimond, M. Brune, and S. Haroche, "Manipulating quantum entanglement with atoms and photons in a cavity," Rev. Mod. Phys. **73**, 565 (2001).

[113] J. Volz, M. Weber, D. Schlenk, W. Rosenfeld, J. Vrana, C. K. K. Saucke, and H. Weinfurter, "Observation of entanglement of a single photon with a trapped atom," Phys. Rev. Lett. **96**, 030404 (2006).

[114] K. S. Choi, H. Deng, J. Laurat, and H. J. Kimble, "Mapping photonic entanglement into and out of a quantum memory," Nature **452**, 67–71 (2006).

[115] N. N. Lepeshkin, A. Schweinsberg, G. Piredda, R. S. Bennink, and R. W. Boyd, "Enhanced nonlinear optical response of one-dimensional metal-dielectric photonic crystals," Phys. Rev. Lett. **93**, 123902 (2004).

[116] M. Scalora, M. A. Vincenti, D. de Ceglia, V. Roppo, M. Centini, N. Akozbek, and M. J. Bloemer, "Second- and third-harmonic generation in metal-based structures," Phys. Rev. A **82**, 043828 (2010).

[117] P. Ginzburg, A. Hayat, N. Berkovitch, and M. Orenstein, "Nonlocal ponderomotive nonlinearity in plasmonics," Opt. Lett. **35**, 1551–1553 (2010).

[118] M. C. Larciprete, A. Belardini, M. G. Cappeddu, D. de Ceglia, M. Centini, E. Fazio, C. Sibilia, M. J. Bloemer, and M. Scalora, "Second-harmonic generation from metallodielectric multilayer photonic-band-gap structures," Phys. Rev. A **77**, 013809 (2008).

[119] J. Peřina Jr. and J. Peřina, "Quantum statistics of nonlinear optical couplers," in "Progress in Optics," vol. 41, E. Wolf, ed., p. 361–419 (Elsevier, Amsterdam, 2000).

[120] P. Yeh, *Optical Waves in Layered Media* (Wiley, New York, 1988).

[121] J. Miragliotta, D. K. Winckenden, T. J. Kistenmacher, and W. A. Bryden, "Linear- and nonlinear-optical properties of GaN thin film," J. Opt. Soc. Am. B **10**, 1447–1456 (1993).

[122] N. Gisin, G. Ribordy, W. Tittel, and H. Zbinden, "Quantum cryptography," Rev. Mod. Phys. **74**, 145–195 (2011).

[123] A. F. Abouraddy, K. C. Toussaint Jr., A. V. Sergienko, B. E. A. Saleh, and M. C. Teich, "Entangled-photon ellipsometry," J. Opt. Soc. Am. B **19**, 656–662 (2002).

[124] O. Alibart, D. B. Ostrowsky, P. Baldi, and S. Tanzilli, "High-performance guided-wave asynchronous heralded single-photon source," Opt. Lett. **30**, 1539–1541 (2008).

Faculty of Science, Palacký University
in Olomouc

Joint Laboratory of Optics

Nonlinear optics in modern photonic structures - generation of quantum correlated photon pairs

Summary of the Ph.D. Thesis

Dalibor Javůrek

Supervisor:
Doc. RNDr. Jan Peřina Jr., Ph.D.

Olomouc 2015

Přírodovědecká fakulta, Univerzita Palackého
v Olomouci

Společná laboratoř optiky

Nelineární optika v moderních fotonických strukturách - generace kvantově korelovaných fotonových párů

Autoreferát dizertační práce

Dalibor Javůrek

Školitel:
Doc. RNDr. Jan Peřina Jr., Ph.D.

Olomouc 2015

Doctoral thesis was carried out under the full-time doctoral program Physics in specialization Optics and Optoelectronics in 2010 - 2015. The research institute at which the thesis was prepared was the Joint Laboratory of Optics in Olomouc. The program was maintained by the Department of Optics at Faculty of Science at Palacký University in Olomouc.

Ph.D. candidate:	**Ing. Dalibor Javůrek**
Supervisor:	**Doc. RNDr. Jan Peřina Jr., Ph.D.** Joint Laboratory of Optics Faculty of Science Palacký University
Co-supervisor :	**Doc. Ing. Ivan Richter, Dr.** Department of Physical Electronics Faculty of Nuclear Sciences and Physical Engineering Czech Technical University
Reviewers:	**Prof. RNDr. Jiří Petráček, Dr.** Department of Optics and Precise Mechanics Faculty of Mechanical Engineering Brno University of Technology
	Doc. Mgr. Kamil Postava, Dr. Department of Physics Faculty of Mining and Geology VŠB - Technical University of Ostrava

The evaluation of the thesis has been written by Doc. RNDr. Jan Peřina Jr., Ph.D.

The summary of the thesis has been sent to distribution on .....

Oral defence will take place on ..... at Department of Optics in front of the committee for Ph.D. study of program Physics and specialization Optics and Optoelectronics, Faculty of Science, Palacký University, room ....., 17. Listopadu 12, Olomouc.

The Ph.D. thesis is available in the library at Faculty of Science of Palacký University.

Statement of originality

I hereby declare that this thesis is my own work and that, to the best of my knowledge and belief, it contains no material previously published or written by another person nor material which to a substantial extent has been accepted for the award of any other degree or diploma of the university or other institute of higher learning, except where due acknowledgement has been made in the text.

In Olomouc, ..., 2015 .....

Submitted on ....., 2015

The author grants permission to Palacký University in Olomouc to store and display this thesis and its electronic version in the university library and on the official website.

Abstract

Spontaneous parametric down-conversion is a nonlinear quantum process in which correlated photons are created in pairs. Photon pairs have become an indispensable tool for verification of quantum-mechanical principles, in quantum-information processing, for quantum-communication protocols and quantum cryptography.

Modern photonic structures enhance photon-pair emission rates and simultaneously modify the properties of generated photon pairs. Periodically-poled silica ring-shaped fibers are capable of generation and stable guidance of photon pairs in modes with defined orbital angular momentum (OAM). The most stable modes have been selected for the nonlinear interaction. Their transversal profiles together with phase-matching conditions have been analyzed to obtain the desired interaction. Narrow-band and broad-band emission of photon pairs have been obtained in dependence on the mode of the pump beam. In the time domain, the conditional probability of detection of a signal photon has been obtained and correlation times have been evaluated. The emission of photon pairs entangled in OAMs and frequencies have been analyzed. Effective dimension of the entangled space has been quantified by means of the Schmidt number indicating a maximally entangled photon-pair state. The influence of noise on the entangled OAM state has been evaluated by the Clauser-Horne-Shimony-Holt inequality.

Also metallo-dielectric layered structures have been analyzed as highly efficient sources of photon pairs. Layered structures consisting of silver (Ag) and Gallium-Nitride (GaN) have been investigated. Two structures formed by three and eleven layers have been designed to maximize the emission rate. They have been examined with respect to relative signal photon-number density in the angular-spectral domain. Both structures have been found more efficient than dielectric structures due to strong back-scattering effects caused by the high index-of-refraction contrast. Distributions of electric-field amplitudes corresponding to the emission maxima have been analyzed. Correlated areas as well as temporal characteristics including those appropriate for the Hong-Ou-Mandel interferometer have been investigated. Also, numbers of noise photons have been discussed as the metallic layers are absorptive.

Abstrakt

Spontánní parametrická frekvenční konverze je nelineární kvantový proces, při kterém jsou vytvářeny korelované fotonové páry. Fotonové páry se staly jedinečným prostředkem pro ověření fundamentálních principů kvantové mechaniky, pro zpracování kvantové informace, pro kvantově komunikační protokoly a kvantovou kryptografii.

Moderní fotonické struktury zvyšují míru emise fotonových párů a současně modifikují vlastnosti generovaných fotonových párů. Periodicky pólovaná křemičitá prstencová vlákna jsou schopna generace a stabilního vedení fotonových párů s definovaným úhlovým momentem (OAM). Nejstabilnější módy byly vybrány pro nelineární interakci. Jejich příčné profily společně s podmínkou sfázování byly analyzovány za účelem optimalizace procesu. Pro odlišné módy čerpacího svazku byla obdržena úzko- a širokospektrální emise fotonových párů. V časové doméně byla obdržena podmíněná pravděpodobnost detekce jalového fotonu a byly spočteny korelační časy. Analyzována byla emise fotonových párů entanglovaných v OAM a frekvenci. Efektivní dimenze entanglovaného prostoru byla vyčíslena pomocí Schmidtova čísla. To poukázalo, že fotony v páru jsou maximálně entanglované v OAM. Vliv šumu na entanglovaný OAM stav byl vyhodnocen pomocí Clauser-Horne-Shimony-Holtovy nerovnosti.

Metalo-dielektrické fotonické struktury byly rovněž analyzovány jako účinné zdroje fotonových párů. Zkoumány byly vrstevnaté struktury skládající se ze stříbra (Ag) a Gallium-Nitridu (GaN). Dvě struktury skládající se ze tří a jedenácti vrstev byly navrženy tak, aby maximalizovaly míru emise fotonových párů. Byly zkoumány s ohledem na relativní počet emitovaných signálových fotonů v úhlově-spektrální doméně. Obě struktury byly shledány účinnějšími než jejich dielektrické protějšky díky vysokému kontrastu indexů lomu obou materiálů. Analyzovány byly distribuce amplitud elektrických polí, které přísluší nejsilnější emisi fotonových párů. Předmětem zkoumání také byly korelované plochy a časové charakteristiky včetně charakteristik příslušných Hong-Ou-Mandelově interferometru. Diskutován byl i počet šumových fotonů, jelikož metalické vrstvy vykazují nenulovou absorpci.

Contents

The goals of the thesis

The main goal was to study spontaneous parametric down-conversion in metallo-dielectric layered media and periodically-poled ring silica fibers. In both cases spectral, spatial and temporal properties of photon pairs have been studied. Photon-pair emission rates of both sources have been evaluated in order to determine their efficiencies.

Photon-pair generation in periodically-poled silica ring fibers

The designed periodically-poled ring-shaped silica fiber guides the modes with defined OAM numbers steadily [1]. The considered fiber core has its inner diameter $r_1 = 4$ μm and outer diameter $r_2 = 5.5$ μm in order to guide only the radially fundamental modes for the wavelengths longer than 1.2 μm. The cross-section of the fiber is shown in Fig. 1(a). The cladding of the fiber consists of pure silica (SiO_2), while the core of the fiber consists of SiO_2 dopped by 19.3 mol% of GeO_2. The length of the poled fiber has been assumed to be 10 cm/[1].

Effective refractive indices of the most stable guided modes at waveleghts $\lambda_p^0 = 0.775$ μm (wavelength of the cw pump beam) and $\lambda_s^0 = 1.55$ μm (degenerate wavelength of the down-converted photons) are shown in Figs. 1(b) and 1(c), respectively. The most stable eigen-modes at both wavelengths are HE_{11}, HE_{21}, TE_{01}, and TM_{01}. The highest risk of overcalls is expected between modes HE_{21} and TE_{01} or HE_{21}

[1] Periodically-poled silica fibers up to 10 cm long can be fabricated by a simple fabrication method [2].

and TM_{01}, because their effective refractive indices are located close to each other. At the wavelength of the pump beam λ_p^0, the difference in effective indices of refraction $\Delta n_{p,\text{eff}}$ between modes HE_{21} and TE_{01} [TM_{01}] is -9×10^{-5} [1×10^4]. At the degenerate wavelength λ_s^0, the quantity $\Delta n_{s,\text{eff}}$ for the closest modes HE_{21} and TE_{01} equals 1.5×10^{-4}. The calculated values of $\Delta n_{s,\text{eff}}$ are comparable to the results obtained for the a vortex fiber [3][2].

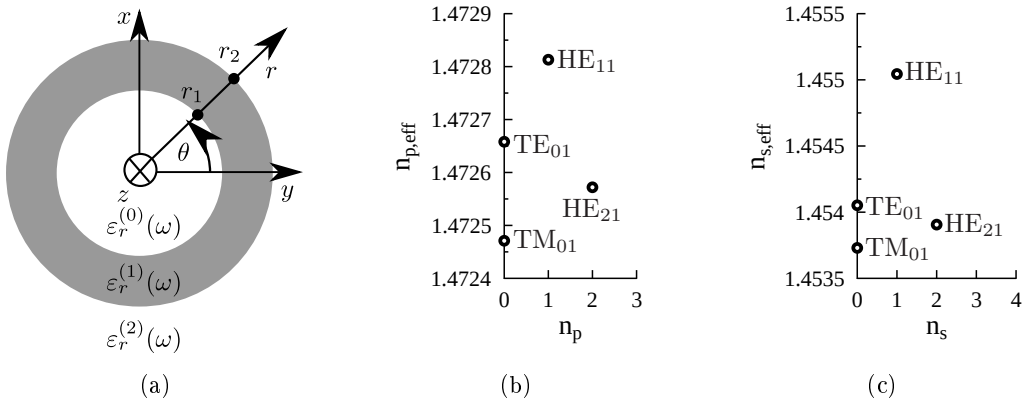

Figure 1: (a) Cross-section of the investigated ring fiber. (b) and (c) Effective indices of refraction $n_{p,\text{eff}}$ and $n_{s,\text{eff}}$ of guided modes for wavelengths $\lambda_p^0 = 0.775$ μm and $\lambda_s^0 = 1.55$ μm, respectively.

The complete set of guided eigen-modes of the fiber is formed by HE and EH modes and TE and TM modes. By a suitable transformation applied to all HE and EH modes,

$$\mathbf{e}_\eta(r,\theta,\omega) = \mathbf{e}_{\tilde{\eta},H}(r,\theta,\omega) \mp i\mathbf{e}_{\tilde{\eta},V}(r,\theta,\omega), \tag{1}$$

the modes with the corresponding OAM are obtained plus TE, TM modes, which remain in their original state. The symbol $\mathbf{e}(r,\theta,\omega)$ is related to an electric-field amplitude in the radial coordinates (r,θ) with frequency ω. Index $\tilde{\eta}$ denotes the original eigen-mode signature (eg. HE_{21}), the indices V and H identify polarization of the eigen-mode and index η contains both the original eigen-mode signature $\tilde{\eta}$, together with its new polarization variant R or L in dependence on the sign in a definition (1). Polarization R [L] is obtained using $-$ [$+$] sign.

The angular spectrum of the electric-field components e_x and e_z/[3] has been com-

[2]It has proved to guide the HE_{21} mode at distance 1 km with low level of noise.

[3]Due to symmetry of the fiber, the electric field components e_x and e_y are identical up to the shift in the angular direction θ by 90 deg.

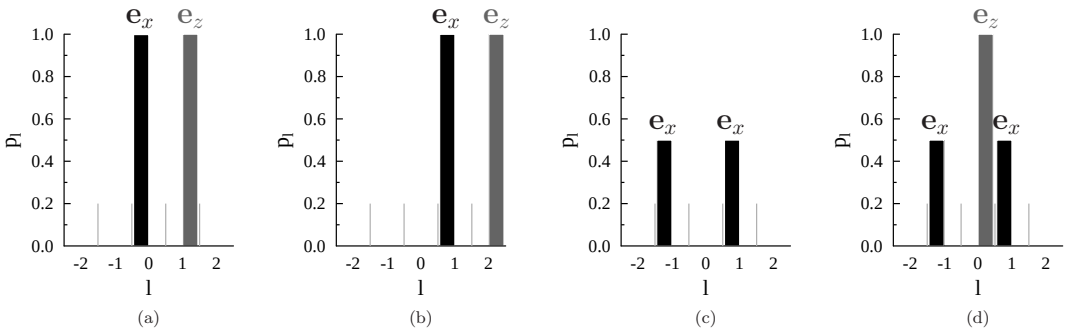

Figure 2: Weights p_l of spectral components l in angular decomposition of field's components according to Eq. 2 for (a) $\mathrm{HE}_{11,R}$, (b) $\mathrm{HE}_{21,R}$, (c) TE_{01}, and (d) TM_{01} mode.

puted for modes $\mathrm{HE}_{11,R}$, $\mathrm{HE}_{21,R}$, TE_{01} and TM_{01} (see Fig. 2) according to Eq. (2). The transversal electric-field component e_x of mode $\mathrm{HE}_{11,R}$ [$\mathrm{HE}_{21,R}$] carries the OAM number equal to 0 [+1]. The variants with the orthogonal polarization L have the OAM number with opposite sign 0 [−1]. The transversal Cartesian components e_x of TE_{01} and TM_{01} modes include OAM equal to ± 1 with the same weights $p_l = 0.5$. The longitudinal component e_z has different OAM than the transversal components by one in the absolute value. It does not take part in the non-linear interactions due to the form of non-linear tensor $\chi^{(2)}$: $\chi^{(2)}_{xxx} \simeq 3\chi^{(2)}_{xyy}$ and $\chi^{(2)}_{xyy} = \chi^{(2)}_{yyx} = \chi^{(2)}_{yxy} = 0.021$ pm/V.

$$p_{l,\eta}(\omega) = \int r dr \left| \int d\theta \, e^{-i\theta l} e_{k,\eta}(r,\theta,\omega) \right|^2 ; \, k \in x, y, z. \tag{2}$$

The non-linear interaction of modes $\mathrm{HE}^p_{21,R}$, $\mathrm{HE}^s_{21,R}$, $\mathrm{HE}^i_{11,R}$, and $\mathrm{HE}^i_{11,L}$ (p, s and i in the superscript denotes pump, signal and idler field) with OAM numbers $+1, +1$ and 0 in turn resulted in narrow-band generation of the photon pairs. The signal photon-number spectrum N_s is shown in Fig. 3(a). The widths of emission peaks (FWHM) are around the 10 nm. The heights of the peaks indicate the generation of tens of photon pairs in each peak per second per μW of the pump beam. The emission is non-degenerate and occurs in the spectral range around the telecommunication wavelength 1.55 μm. The highest peak at wavelength $\lambda_s = 1.5$ μm belongs to mode $\mathrm{HE}_{21,R}$ with the emission rate 20 photons per s per μW (in the peak). The signal and idler photons are emitted as well in modes without a well defined OAM (TE_{01} and TM_{01}). But their contributions are spectrally separated from the modes with defined OAM. It is worth to note that the paired signal and idler photons at wavelengths $\lambda_s = 1.5\,\mu$m and $\lambda_i = 1.603\,\mu$m are simultaneously emitted in either modes $\mathrm{HE}^s_{21,R}$, $\mathrm{HE}^i_{11,R}$ or modes

$\mathrm{HE}^{s}_{21,R}$, $\mathrm{HE}^{i}_{11,L}$. Since the probability of emission is the same, modes $\mathrm{HE}_{11,R}$ and $\mathrm{HE}_{11,L}$ form a common peak in the signal photon-number spectrum in Fig. 3(a). With the use of the wavelength multi/demultiplexers [4], the spectrally separated photons can be used for OAM information processing.

The broad-band emission of photon pairs as been observed for the configuration of the interacting fields: $\mathrm{HE}^{p}_{11,R}$, TE^{s}_{01} and TE^{i}_{01}. The width of the peak (FWHM) in signal photon-number spectrum N_s reaches 142 nm with 150 photon pairs per s per μW in peak [Fig. 3(b)]. The emission is centered around the degenerate wavelength 1.55 μm. In the signal photon-number spectrum N_s the only significant contribution is given by the TE_{01} modes.

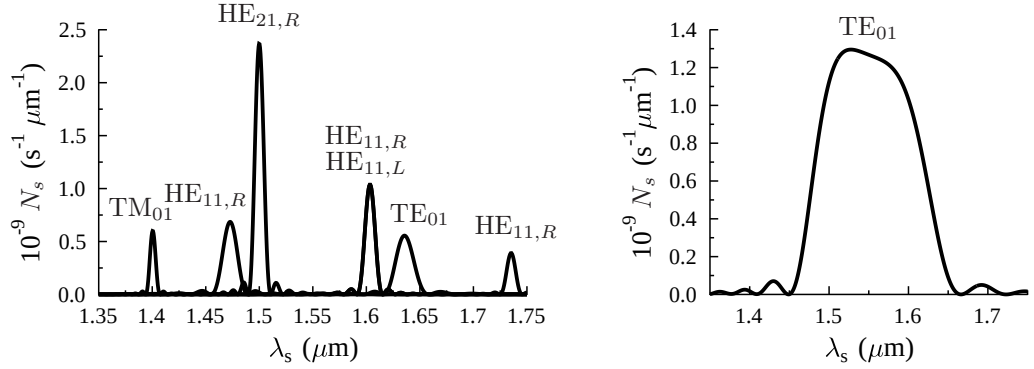

(a) (b)

Figure 3: Signal photon-number spectrum N_s for (a) $\Lambda = 42.9$ μm and $\mathrm{HE}^{p}_{21,R}$ mode (b) $\Lambda = 41.06$ μm and $\mathrm{HE}^{p}_{11,R}$ mode; Λ denotes length of period of QPM grating followed by mode of the pump beam. Each peak in the signal photon-number spectrum N_s corresponds to the emission into a particular mode η. Individual modes η are indicated in the graphs.

Time probability of detection an idler photon $p_{t,i}$ conditioned by the detection of the signal photon at time $t_s = 0$ s is shown in Fig. 4(a). The correlation time τ is determined as FWHM of the $p_{t,i}$ peak in the profile of probability. Correlation time for the narrow-band process [$\mathrm{HE}^{p}_{21,R}$, $\mathrm{HE}^{s}_{21,R}$, $\mathrm{HE}^{i}_{11,R}$ ($\mathrm{HE}^{i}_{11,L}$)] equals $\tau = 63.5 \times 10^{-14}$ s whereas the broad-band process ($\mathrm{HE}^{p}_{11,R}$, TE^{s}_{01}, TE^{i}_{01}) is characterized by $\tau = 4.5 \times 10^{-14}$ s. Sharp temporal correlations are important in metrology as they determine the available temporal resolution.

If the pump beam remains in $\mathrm{HE}_{11,R}$ mode and period of the QPM grating is properly chosen ($\Lambda = 41.06$ μm), the photon pairs are emitted into the modes $\mathrm{HE}_{21,R}$ and $\mathrm{HE}_{21,L}$ with OAM number $+1$ and -1, respectively. The Schmidt number K_θ has been

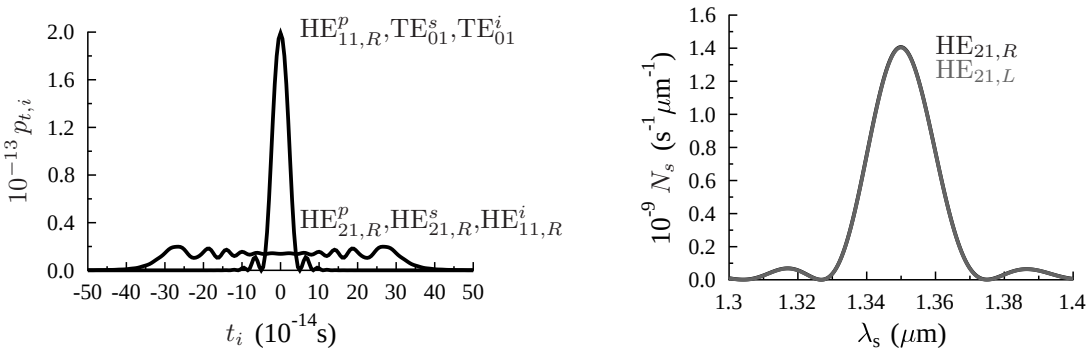

Figure 4: (a) Probability of detection of an idler photon $p_{t,i}$ in dependence on time t_i, conditioned by the detection of a signal photon at time $t_s = 0$ s. (b) Signal photon-number spectrum N_s for the period of QPM grating $\Lambda = 41.06$ μm and pump mode $\mathrm{HE}_{11,R}$.

calculated by both approximative ($K_\theta = 1.998$) and rigorous method ($K_\theta = 1.994$). Thus, the resulting photon-pair state is nearly maximally entangled in the OAM. This is confirmed by nearly perfect overlap of the emission peaks of both modes ($\mathrm{HE}_{21,R}$ and $\mathrm{HE}_{21,L}$) in the signal-photon number spectrum N_s [Fig. 4(b)]. Width (FWHM) of the peaks in the signal photon-number spectrum is 21 nm. There are 30 signal photons per s per μW in each of them. The obtained OAM entangled state $|\psi\rangle$,

$$|\psi\rangle = \int d\omega_s d\omega_i \, \Phi_{1_s,-1_i}(\omega_s,\omega_i)|1,\omega_s\rangle_s|-1,\omega_i\rangle_i + \Phi_{-1_s,1_i}(\omega_s,\omega_i)|-1,\omega_s\rangle_s|1,\omega_i\rangle_i \quad (3)$$

exhibits simultaneous entanglement in the frequency domain. Effective dimension of the entangled space in the frequency domain reaches the maximal value of 100 for 2 nm wide (FWHM) spectrum of the Gaussian pump beam. Due to separability of state (3) in the frequency and spatial domain ($\Phi_{1_s,-1_i} \approx \Phi_{-1_s,+1_i}$), the effective dimension of the entire entangled space can be as high as 200. Maximally entangled photon pairs are highly desired, e.g., for quantum teleportation protocols or quantum computing.

Noise potentially contributing to the generated two-photon state arises from other non-linear processes, photon losses and generation of photons in unwanted modes [5]. All the sources has been evaluated to be negligible. Despite this the fabrication imperfections and handling of the two-photon state in an experimental setup may introduce additional noise. The impact of noise on the two-photon state entangled in OAM is evaluated by the Clauser-Horne-Shimony-Holt form of the Bell inequalities. The state

has to be de-entangled by more than 28% to reach the critical bound $S = 2$ indicating non-classicality. This does not put real limitations for experiments. The value of parameter S has been measured as high as 2.78 for entangled OAM modes with OAM quantum numbers ± 1.

Photon-pair generation in metallo-dielectric 1D photonic structures

The process of SPDC is studied in a metallo-dielectric layered structure consisting of Gallium-Nitride (GaN) and silver (Ag) layers. The first investigated structure is a simple Ag-GaN-Ag resonator. It is designed to provide the highest amount of photon pairs. The designed most efficient structure has the length of metallic layers $l_1 = 9.6376$ nm and length of dielectric layers $l_2 = 95.1195$ nm. The relative signal photon-number density η_s/[4] of the structure is shown in Fig. 5(a). The pump field is assumed to be a TE-polarized monochromatic plane wave with wavelength $\lambda_p^0 = 400$ nm propagating along the axis z. The emission of signal photons is strongly directional and wavelength selective. The maxima in relative signal photon-number density η_s are located around the radial angle $\vartheta_s = 83$ deg and degenerate wavelength $\lambda_s = 800$ nm. If the angle of emission declines from the point of the most intense generation, the number of generated signal photons significantly drops. The directional and wavelength sensitivity of emission of signal photons is caused by the strong resonance of the signal and idler fields inside the structure. The signal photon-number density of the resonator is compared to the same quantity of a GaN monolayer of the same length [see Fig. 5(b)]. The ratio κ_s shows that the resonator emits up to 10^8 more signal photons in the region of resonance.

[4]Relative signal photon number density η_s is defined as $\eta_s(\lambda, \vartheta) = n_s(\lambda, \vartheta)/\max_{\vartheta,\lambda}\{n_s^{\mathrm{ref}}(\lambda, \vartheta)\}$, where n_s [n_s^{ref}] is signal photon-number density of the structure [reference structure] and function $\max_{\vartheta,\lambda}$ gives the maximum value of a function in the argument across the radial emission angle ϑ and wavelength λ.

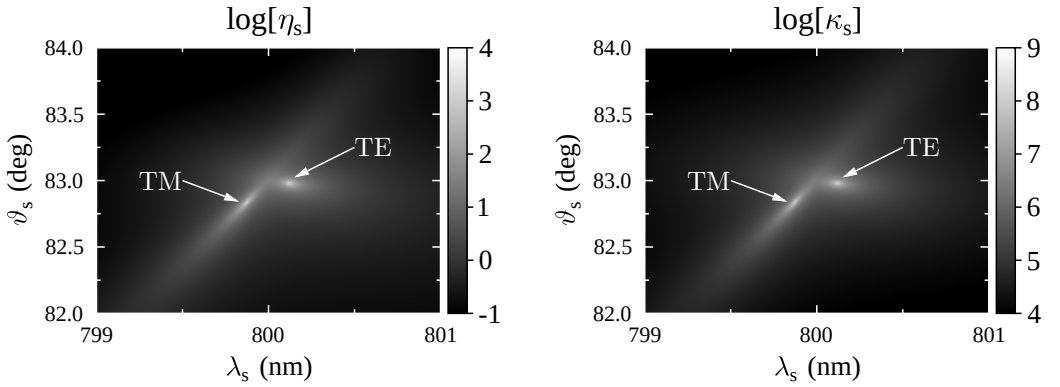

(a) (b)

Figure 5: (a) Relative signal photon-number density η_s of Ag-GaN-Ag resonator (b) κ_s - ratio of signal photon-number density of the Ag-GaN-Ag resonator and single GaN layer of the same length ($l = 114.3947$ nm); ϑ_s is radial emission angle and λ_s is wavelength of the signal photon. The length of Ag layers [GaN layer] in the resonator is equal to $l_1 = 9.6376$ nm [$l_2 = 95.1195$ nm], $\lambda_p^0 = 400$ nm.

The structure consisting of eleven layers exhibits non-degenerate emission of photon pairs [see Figs. 6(a) and 6(b)]. The length of GaN [Ag] layers of the designed structure is $l_1 = 101.752$ nm [$l_2 = 18.083$ nm]. There are two emission peaks in the relative signal photon-number density η_s. The first [second] peak is located at wavelength $\lambda_s = 737.8367$ nm [$\lambda_s = 873.6015$ nm] and radial emission angle $\vartheta_s = 47.686$ deg [$\vartheta_s = 61.095$ deg]. The relative signal photon-number density η_s attains values up to 10^7 near the emission peaks. Thus, the structure is two orders of magnitude more efficient than the Ag-GaN-Ag resonator. In comparison with purely dielectric multilayer systems, the structure can be up to seven orders of magnitude more efficient [6]. The normalized signal photon-number density η_s shows even sharper characteristics than in the case of the resonator [see Fig. 5(a)]. This is caused by stronger interference of the fields inside the structure owing to the presence of the higher number of layers. For the regions of the most intense emission, the transversal components of the interacting electric fields are plotted in Figs. 7(a) - 7(c). The y component of TM-polarized idler electric field [see Fig. 7(c)] is amplified by five orders of magnitude, while the TE-polarized component of the pump [see Fig. 7(a)] and signal [see Fig. 7(b)] fields are amplified only several times. Therefore, strong enhancement of the process arises from the resonant amplification of the TM polarized idler field at wavelength $\lambda_i = 873.6$ nm

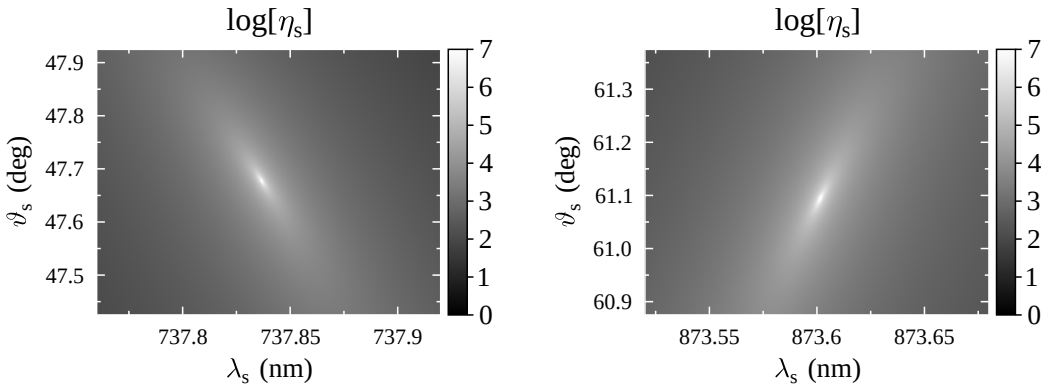

(a) (b)

Figure 6: Relative signal photon-number density η_s in dependence on signal wavelength λ_s and radial emission angle ϑ_s for two regions containing (a) TE-polarized and (b) TM-polarized photons; $\lambda_p^0 = 400$ nm, $l_1 = 101.752$ nm, $l_2 = 18.083$ nm.

emitted at radial angle $\vartheta_i = -61.095$ deg. For the determination of modes, the boundary conditions of the fields were set such that the pump field impinges on the structure at the front interface ($z = 0$) with amplitude 1 V/m. The amplitude of the backward propagating pump field at the rear end of the structure was set to zero. The electric-field amplitudes of signal and idler fields leaving the structure at its rear end were equal to 1 V/m. The amplitudes of the outgoing signal and idler waves at the opposite edge of the structure were assumed to be zero.

Correlated areas of the signal and idler beams differ significantly. The pump beam is assumed to have a Gaussian transversal shape with the radial width equal to 1 mm. It is assumed to propagate along the z axis of the structure. The radial emission angle of the idler photon is assumed to be fixed at $\vartheta_i^0 = -61.095$ deg and azimuthal is $\psi_i^0 = 0$ deg. This direction corresponds to the emission maximum in Fig. 6(b). By these conditions, the correlated area of the TE-polarized signal beam has a Gaussian shape [Fig. 8(a)]. This means that the shape of the area is determined by spatial parameters of the pump beam. When the radial emission angle of the signal photon is fixed at value $\vartheta_s^0 = 47.686$ deg and azimuthal angle equals $\psi_s^0 = 0$ deg, the correlated area of the idler photon is highly elliptic [see Fig. 8(b)]. The width of correlated area in the radial direction ϑ_i is governed by the transmission properties of the idler photon near the region of resonance. In the azimuthal direction psi_i, its width is determined by the width of Gaussian pulse.

The squared modulus of two-photon amplitude n_i computed for the most intense

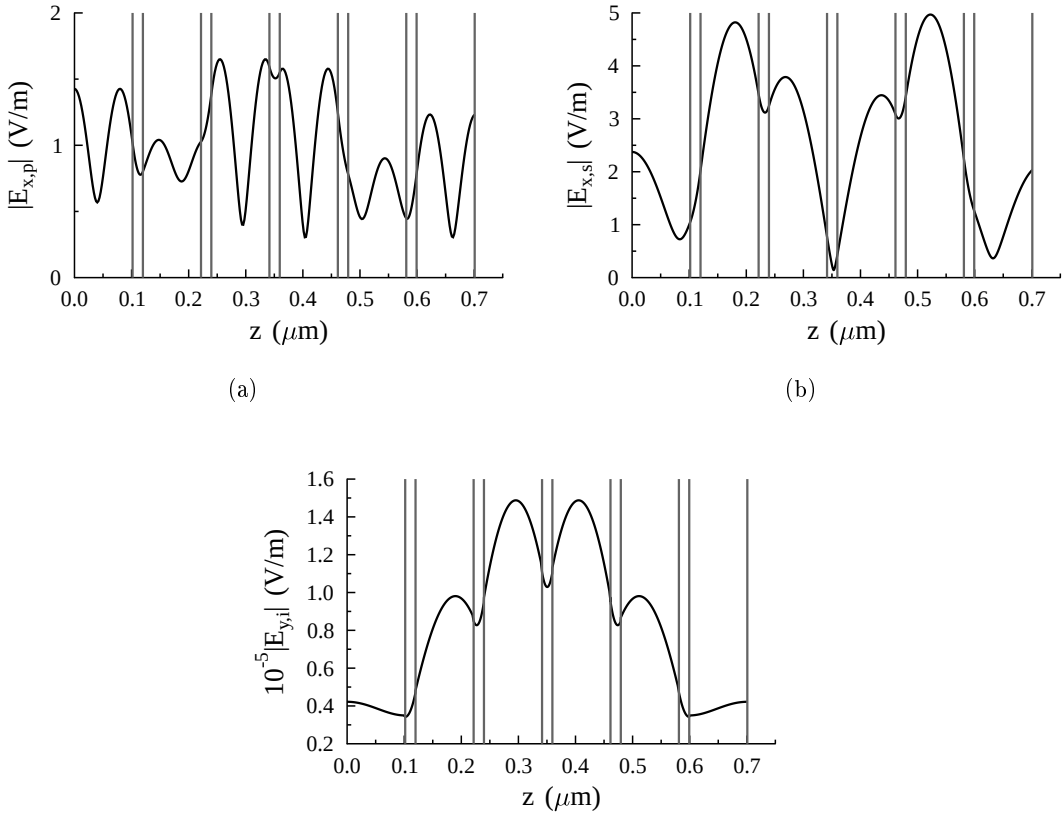

Figure 7: Profile of modulus of the electric-field amplitude for (a) pump, (b) signal and (c) idler fields along the z axis for the pump field with amplitude 1 V/m incident at $z = 0$ m and outgoing signal and idler fields with amplitudes 1 V/m at the end of the structure composed of eleven GaN/Ag layers with lengths $l_1 = 101.752$ nm, $l_2 = 18.083$ nm; $\lambda_p^0 = 400$ nm, $\vartheta_p = 0$ deg, $\lambda_s = 737.8367$ nm, $\vartheta_s = 47.686$ deg, $\lambda_i = 873.6015$ nm, $\vartheta_i = -61.095$ deg.

emission ($\vartheta_s = 47.686$ deg, $\vartheta_i = -61.095$ deg, $\psi_s = \psi_i = 0$ deg) is 4.45×10^{-4} nm wide (FWHM) [see Fig. 9(a)]. This results in temporal correlations at the time scale of nanoseconds. The conditional time probability p_i of detection of an idler photon, provided that the signal photon has been detected at time $\tau_s = 0$ s, is shown in Fig. 9(b). It is asymmetric, expressing that the TM-polarized idler photon leaves the structure after the TE-polarized signal photon. The TM-polarized idler photon undergoes more back reflections in the structure than the TE-polarized signal photon. This is in agreement with the resonant behaviour of the idler photon. As a result, the TM-polarized idler

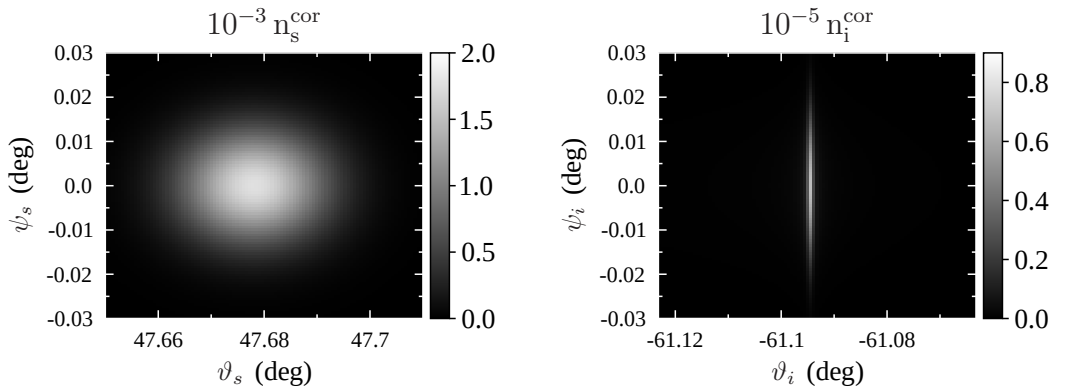

Figure 8: Correlated area $n^{\rm cor}$ of (a) signal [(b) idler] photon observed after detection of an idler [signal] photon at direction $\vartheta_i^0 = -61.095$ deg and $\psi_i^0 = 0$ deg [$\vartheta_s^0 = 47.686$ deg and $\psi_s^0 = 0$ deg] for the structure analyzed in Fig. 6. The correlated areas are normalized such that $\int d\vartheta \int d\psi\, n^{\rm cor}(\vartheta, \psi) = (\pi/180)^2$.

photon stays in the structure for longer time on average. Different time properties of TE-polarized signal photon and TM-polarized idler photon are as well observed in the Hong- Ou-Mandel interferometer (see Fig. 10). The envelope of normalized coincidence-count rate R is positioned in the negative values. This requires the TE-polarized photon to be delayed in order to observe detections in a coincidence. Fast oscillations in the characteristics are caused by unequal wavelengths of the signal and idler photons.

The amount of noise photons emitted from the structure is at the same level as the number of photon pairs. This is documented by ratios R_s and R_i of absorbed single photons and number of generated photon pairs [see Figs. 11(a) and 11(b)]. They are defined as

$$R_{s,ab}^{\alpha\beta}(\mathbf{\Omega}_s) = \frac{d_{s,a}^{\alpha}(\mathbf{\Omega}_s)}{n_{s,ab}^{\alpha\beta}(\mathbf{\Omega}_s)}, \qquad R_{i,ab}^{\alpha\beta}(\mathbf{\Omega}_i) = \frac{d_{i,b}^{\beta}(\mathbf{\Omega}_i)}{n_{i,ab}^{\alpha\beta}(\mathbf{\Omega}_i)}. \tag{4}$$

Index a [b] denotes backward (B) or forward (F) propagating signal [idler] photon at the corresponding output of the structure, index α [β] stands for the polarization of signal [idler] photon. The coefficient $d_{s,a}^{\alpha}(\mathbf{\Omega}_s)$ denotes density of mean number of photon pairs, whose signal photon with polarization α has been transmitted to output a and idler photon has been absorbed. The number of photon pairs $n_{s,ab}^{\alpha\beta}$ denotes mean number of photon pairs whose signal photon with polarization α has been transmitted to output a and idler photon with polarization β to output b. The vectors $\mathbf{\Omega}_m = (\omega_m, \vartheta_m, \psi_m)$; $m = s, i$ correspond to spherical coordinates of the signal (s) or idler (i) wave vector space.

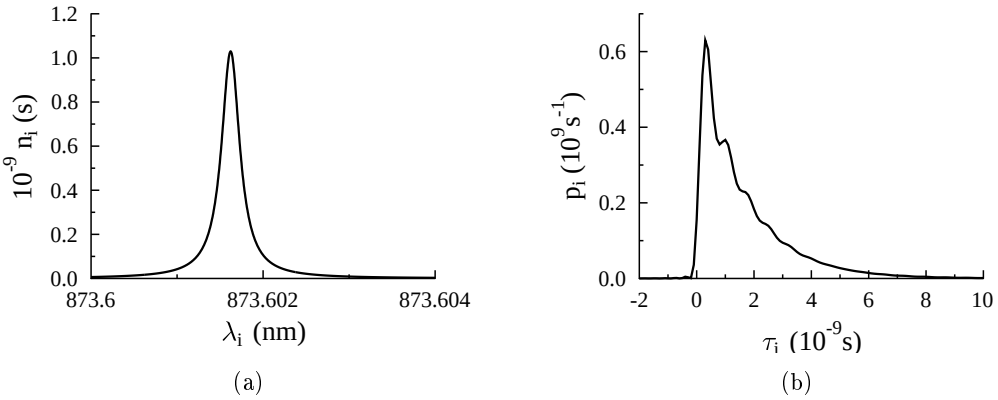

Figure 9: (a) Idler spectral photon-number density n_i as a function of idler wavelength λ_i and (b) probability density p_i of detecting an idler photon at time τ_i provided that its signal twin was detected at time $\tau_s = 0$ s; $p_i(\tau_i) = C|\mathcal{A}(\tau_s = 0, \tau_i)|^2$ using an appropriate normalization constant C. A photon pair is emitted in directions $\vartheta_s = 47.686$ deg and $\psi_s = 0$ deg and $\vartheta_i = -61.095$ deg and $\psi_i = 0$ deg from the GaN/Ag layered structure with length of the layers $l_1 = 101.752$ nm, $l_2 = 18.083$ nm. Normalization is such that $\int d\omega_i \, n_i(\omega_i) = 1$ and $\int d\tau_i \, p_i(\tau_i) = 1$.

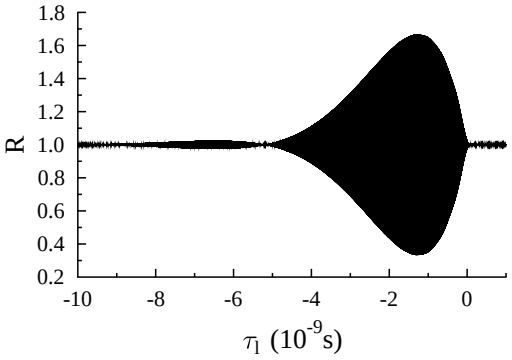

Figure 10: Normalized coincidence-count rate R in the Hong-Ou-Mandel interferometer depending on mutual time delay τ_l between the signal and idler photons. The structure described in the caption of Fig. 9 is analyzed.

Higher amount of noise photons is produced near the photonic stop-bands and near the angle of total reflection due to multiple back-reflections. In the area of the most intense emission of the signal photon ($\lambda_s = 738$ nm $\vartheta_s = 47$ deg), the value of ratio $R_{s,FF}^{\mathrm{TE,TM}}$ is equal to 1.2. Near the neighbourhood of the most intense emission of the idler photon ($\lambda_i = 834$ nm,$\vartheta_i = 61$ deg) the value of ratio $R_{i,FF}^{\mathrm{TE,TM}}$ is equal to 0.97.

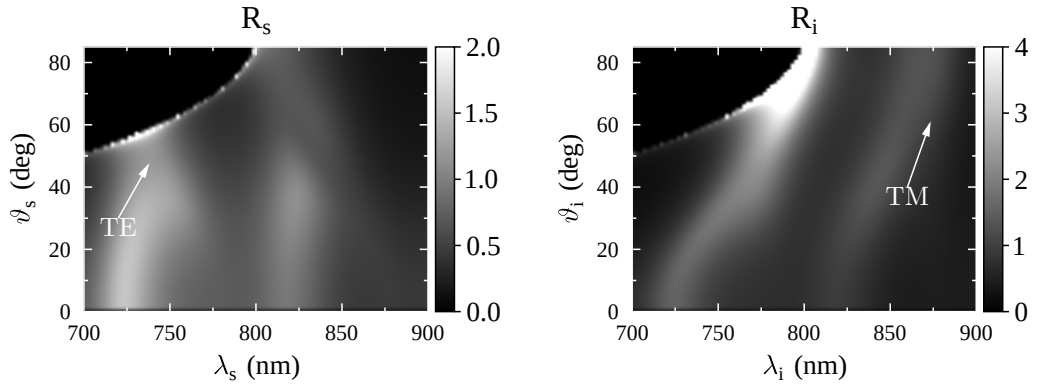

(a) (b)

Figure 11: Ratio (a) $R_{s,FF}^{\mathrm{TE,TM}}$ [(b) $R_{i,FF}^{\mathrm{TE,TM}}$] of signal [idler] noise photon-number density and photon-pair density in dependence on signal [idler] radial emission angle ϑ_s [ϑ_i] and wavelength λ_s [λ_i] determined along Eq. (4). The photon-pair field contains the forward-propagating TE-polarized signal and TM-polarized idler photons; $\lambda_p^0 = 400$ nm, $l_1 = 101.752$ nm, $l_2 = 18.083$ nm.

The characteristics of ratios R_s and R_i are smooth functions without resonances which means that the amount of absorbed signal photons is more-less proportional to the number of generated photon pairs. The noise photons and photon pairs are produced with similar intensity in metallo-dielectric photonic structures. This restricts the use of metallo-dielectric layered structures, as sources of photon pairs to experiments involving coincidence-count detections.

List of author's publications

[A1] D. Javůrek, J. Svozilík, and J. Peřina Jr., "Proposal for the generation of photon pairs with nonzero orbital angular momentum in a ring fiber," Opt. Express **22**, 23743–23748 (2014).

[A2] D. Javůrek, J. Svozilík, and J. Peřina, "Emission of orbital-angular-momentum-entangled photon pairs in a nonlinear ring fiber utilizing spontaneous parametric down-conversion," Phys. Rev. A **90**, 043844 (2014).

[A3] D. Javůrek, J. Svozilík, and J. Peřina Jr., "Entangled photon-pair generation in metallo-dielectric photonic bandgap structures," in "Wave and Quantum Aspects of Contemporary Optics," , vol. 8697 of *SPIE Conference proceedings*, J. Peřina Jr., L. Nožka, M. Hrabovský, D. Senderáková, W. Urbanczyk, and O. Haderka, eds., p. 869727 (2012).

[A4] D. Javůrek, J. Svozilík, and J. Peřina, "Photon-pair generation in nonlinear metal-dielectric one-dimensional photonic structures," Phys. Rev. A **90**, 053813 (2014).

[A5] D. Javůrek, J. Peřina Jr., and J. Svozilík, "Spontaneous parametric down conversion in nonlinear metallo-dielectric layered media," in "Wave and Quantum Aspects of Contemporary Optics," , vol. 8697 of *SPIE Conference proceedings*, W. U. A. Popiolek-Masajada, eds., p. 94410V (2014).

Bibliography

[1] Y. Yue, Y. Yan, N. Ahmed, J.-Y. Yang, L. Zhang, Y. Ren, H. Huang, K. M. Birnbaum, B. I. Erkmen, S. Dolinar *et al.*, "Mode properties and propagation effects of optical orbital angular momentum (OAM) modes in a ring fiber," IEEE Phot. J. **4** (2012).

[2] J. Zhang, "Thermal poling of twin-hole fibers," Master's thesis, Department of Electrical and Computer Engineering, University of Toronto (2008).

[3] N. Bozinovic, Y. Yue, Y. Ren, M. Tur, P. Kristensen, H. Huang, A. E. Willner, and S. Ramachandran, "Terabit-scale orbital angular momentum mode division multiplexing in fibers," Science **340**, 1545–1548 (2013).

[4] B. Guan, R. P. Scott, C. Qin, N. K. Fontaine, T. Su, C. Ferrari, M. Cappuzzo, F. Klemens, B. Keller, M. Earnshaw *et al.*, "Free-space coherent optical communication with orbital angular momentum multiplexing/demultiplexing using a hybrid 3D photonic integrated circuit," Optics Express **22**, 145–156 (2014).

[5] E. Y. Zhu, Z. Tang, L. Qian, L. G. Helt, M. Liscidini, J. E. Sipe, C. Corbari, A. Canagasabey, M. Ibsen, and P. G. Kazansky, "Direct generation of polarization-entangled photon pairs in a poled fiber," Phys. Rev. Lett. **108**, 213902 (2012).

[6] J. Peřina Jr., "Spatial properties of entangled photon pairs generated in nonlinear layered structures," Phys. Rev. A **84**, 053840 (2011).

[7] S. Ramachandran, P. Kristensen, and M. F. Yan, "Generation and propagation of radially polarized beams in optical fibers," Opt. Lett. **34**, 2525–2527 (2009).

[8] J. Peřina Jr., "Spontaneous parametric down-conversion in nonlinear layered media," in "Progress in Optics," vol. 59, E. Wolf, ed., p. 89–158 (Elsevier, 2014).

[9] M. Scalora, M. J. Bloemer, A. S. Manka, J. P. Dowling, C. M. Bowden, R. Viswanathan, and J. W. Haus, "Pulsed second-harmonic generation in nonlinear, one-dimensional, periodic structures," Phys. Rev. A **56**, 3166–3174 (1997).

[10] M. Scalora, M. J. Bloemer, and C. M. Bowden, "Laminated photonic band structures with high conductivity and high transparency: Metals under a new light," Opt. Photon. News **10**, 24–27 (1999).